INTERNATIONAL ATOMIC ENERGY AGENCY
INTERNATIONAL CENTRE FOR THEORETICAL PHYSICS
I.C.T.P., P.O. BOX 586, 34100 TRIESTE, ITALY, CABLE: CENTRATOM TRIESTE

H4.SMR/1013-32

SCHOOL ON THE USE OF SYNCHROTRON RADIATION
IN SCIENCE AND TECHNOLOGY:
*"John Fuggle Memorial"*

**3 November - 5 December 1997**

***Miramare - Trieste, Italy***

---

# *Scattering by Biological Materials*

**Jean Doucet**
**Universite' de Paris XI (Paris-Sud)**
**France**

School on the use of Synchrotron Radiation
in Science and Technology

Trieste, November 1997

# Lecture : Scattering by Biological Materials

Jean Doucet (Lure - France)

## I Introduction

1. Biological Materials
2. Basic knowledge for scattering by biological materials
3. Interest of Synchrotron radiation for biological materials

## II Protein Cryptallography

1- Overview
2. The phase problem
3. The resolution
4. An experimental protein crystallography station
5. Examples
6. Time-resolved protein cryptallography

## III Scattering by chain molecules

1- Overview
2. Principles of scattering by chain molecules
3. examples : DNA, collagen, keratin, muscles
4. Synchrotron radiation and chain molecules

## IV Scattering by lipids and membranes

1- Overview
2- Examples

# I Introduction

## 1 - Biological Materials

Ref: wonderful "Introduction" in

HERCULES by D. BLOW

" Neutron and Synchrotron radiation for condensed matter studies "

vol III - p 111 - 116

Les Editions de Physique - Springer Verlag (1994)

- proteins
- DNA
- lipids
- sugars

# BIOLOGY

## INTRODUCTION

D. M. BLOW

The major scientific achievement of the last 40 years has been the integration of molecular science and biology. Although some of the most spectacular details are common knowledge, presented in high-school textbooks and popular television programmes, it is much more difficult to grasp the huge breadth of knowledge which has been brought together in this process, and the vast range of techniques which have been developed for its achievement. About 40 years ago, at the beginning of the molecular biological revolution, Linus Pauling wrote a wonderful *General Chemistry* which provided a survey of the whole field as it then was, ripe for development. Today, no single undergraduate textbook tries to cover the whole range of achievement, and indeed no undergraduate course could cover it.

There is an integrated range of techniques and discoveries, based in Biochemistry, Microbiology and Genetics, which have come to be known as "Molecular Biology", which are basic knowledge for Life Sciences students, and are well documented in a number of first-class textbooks. There is also a wide range of Physical, Organic and Physical Organic Chemistry, basic for molecular insights into biology, which is recognised as part of the standard equipment of the chemist, and is standard material of Chemistry textbooks.

The part of the subject which is based in Physics, Colloid Science and Statistical Mechanics is less well provided with textbooks, and those which exist tend to be specialised monographs. Thus there are many good texts on Crystallography, Polymer Science, Nuclear Magnetic Resonance, Liquid Crystals ... but few which try to present the impact of all these topics on the broad understanding of biology in molecular terms.

In designing the HERCULES course, the organisers have brought together a wide range of specialised topics in this area, concentrating on those which draw research workers to use large facilities. The authors invited to contribute to this part of HERCULES have provided something approaching a textbook, extending in some cases to a fairly advanced level, and which can be of particular use in the biological exploitation of large facilities.

In my introduction to the biological section of the course, I address the fundamental character of biological systems, and try to provide some essential background within the areas often regarded as Chemistry and "Molecular Biology".

Living cells are self-contained functional units, able to organise themselves, to maintain an energy flow from whatever they can find in the environment, and capable of self-reproduction. To think in detail about the requirements of such a system, we may consider the design of an automatic factory, whose most important function is to build copies of itself.

A bronze statue may be copied by forming a "mould" of it in an appropriate type of cement, into which liquid metal may be poured. Such direct copying occurs also in biology, at the level of DNA replication, where a matching piece is inserted against every specific feature of the nucleic acid, to produce a negative copy or "mould" of it, which can in turn reproduce the original. But for the copying of more complicated structures, such a mechanism breaks down. Try to imagine a machine for copying a mechanical watch by sensing and reproducing its shape, and the types of material which are used. Then imagine doing the same for a quartz crystal watch or a CD player. Long before these complexities are encountered (and these are simple structures compared to you and me!), it is easier to ask for a specification, or blueprint, of the parts to be made, than to copy them by inspection.

In just the same way, the automatic factory's first requirement is for specifications of the total automatic factory which is to be constructed. It is essential to safeguard the originals from the aggressive environment of the construction area, where they will be spattered with oil and swarf or torn up by the machinery.

The automatic factory needs **information**

- stored in a library;
- arrangements to find and copy required information;
- only copies allowed out;
- the library itself needs to be copied for the new factory under construction;
- this copy library needs to be carefully checked, since errors will propagate;
- to eliminate errors use digital rather than analogue storage media.

The factory also needs **functional machines** including

- machine tools - with automatic control
  - including machine-tool-making machines;
- transporters - both passive flow channels
  - and active carriers;
- two types of copiers
  - to copy the whole library of the original factory
  - to copy selected information to control machine tools;
- cleaning machines - to clean up and re-use rubbish and spoilt work
  - including products rejected by quality control;
- energy supplies - using fuel brought in from outside, or rubbish
  - providing energy for tools and transporters.

The factory requires a **structural organisation**, placing boundaries

- between the organised factory and the mass of rubbish outside;
- between the library and the shop floor;
- between parts of the shop floor where incompatible activities take place.



It also requires **temporal organisation** with sequencers and time signals

- to organise tasks in their proper order;
- to make sure no task is begun until a preliminary stage is finished;
- to control the commissioning of the new factory when it is completed, and its separation from the old one.

All of these components are found in living cells. The information stores are *nucleic acids*, long copolymers made of four alternative monomers whose sequence carries the information. The machines are *proteins*, amino-acid polymers with the unique property that they fold up spontaneously into three-dimensional shapes. The structural organisation is mediated by *membranes* which are usually composed of phospholipid glycerides. We do not know the mechanism which specifies the topology and the specific properties of different membranes. The temporal organisation of DNA replication and cell division is mediated by mechanisms for chemical modification of proteins controlled by *cell-cycle proteins*.

| | |
|---|---|
| **INFORMATION** | |
| original library information | DNA |
| copying original information | DNA polymerase |
| checking and correction | repair enzymes |
| copying for issue | DNA-dependent RNA polymerase |
| issued information | RNA |
| **MACHINES** | |
| machine tools | enzymes |
| machine-tool-making machines | ribosomes (enzyme-RNA complex) |
| cleaning machines | proteinases, nucleases |
| energy supplies | sugar, ATP |
| energy transduction | metabolic enzymes |
| **ORGANISATION** | |
| spatial boundaries | phospholipid membranes |
| passive transporters | specific pores in membranes<br>specific binding proteins |
| active transporters | ATP-driven pumps in membranes<br>motile fibrous proteins |
| time signals, sequence control | cell cycle proteins |

The two fundamental types of nucleic acid, in which the sugar is either deoxyribose (DNA) or ribose (RNA) have significantly different conformational properties. DNA has a strong tendency to form stiff double helices with very regular external structure, ideal for information storage. DNA double helices are stored in chromosomes in supercoiled form, where the coils are stabilised by protein molecules (histones). RNA is more versatile structurally, though a degree of specific base-paring is important in maintaining a particular structure. RNA occurs in a variety of different biochemical contexts, for example

- messenger RNA (mRNA) – an edited DNA transcript;
- ribosomal RNA (rRNA) – part of the machinery of the ribosome;
- transfer RNA (tRNA) – a specific "label" attached to an amino acid to render it recognisable during protein synthesis.

The code which specifies the conversion of a RNA message to an amino-acid sequence has several important consequences. In freshly synthesised DNA there are only four possible bases, which pair specifically:

adenine <-> uracil

guanine <-> cytosine.

There are twenty different types of amino-acid in freshly synthesised protein.

There are thus four possible "letters" in the DNA code, which have to specify one of the 20 possible amino-acids in the target protein. This is achieved by a triplet code, in which each of the 64 possible 3-letter "words" in DNA specifies one of 20 amino-acids (or "stop"). For most amino acids, there are several different DNA codes. Crick's "fundamental dogma" concerns the flow of information from nucleic acid to protein, but not in the reverse direction. It may be written


and is a natural consequence of this type of code, since although a DNA or RNA sequence uniquely specifies the amino-acid sequence of a protein (once the "reading frame" which separates the triplets is defined), the protein sequence cannot specify a unique nucleic acid sequence.

The machine tools for making machine tools are very special. They are huge complexes of protein and RNA known as *ribosomes*. They provide a system through which the mRNA is fed, and on which an amino-acid polymer is synthesised according to the information encoded in the mRNA. This process has been studied biochemically in great detail, and the steps by which it proceeds are known in detail. But the molecular structure of the ribosome, and the detailed mechanism of its action, are still unknown.

Proteins, as amino-acid polymers, have a fundamental property which has no counterpart in man-made machines. The polymer is specified and assembled as a linear polymer, but the specific sequence of the polymer defines a three-dimensional conformation which can be reached efficiently by a well-defined route, and which is more stable than the extended polymer. The *linear* polymer thus specifies a definite *three-dimensional shape*. Despite all we know about protein structure today, this folding process sets a baffling problem which is



beyond the power or accuracy of present conformational modelling techniques. Although the amino-acid sequence specifies a three-dimensional shape, the only way we can recognise it is if the amino-acid sequence has a clear and close resemblance to that of a protein whose structure is already known.

The variety of amino-acid side chains, bulky or small, polar or non-polar, acidic or basic which occur in proteins, confers a versatility on their properties, and their structure is often complex. A nomenclature to classify the various levels of structural organisation is generally used :

**Primary structure** – the sequence of individual side-chains along the peptide chain which specifies the chemical formula of the protein.

**Secondary structure** – local regularity in the relationship of amino-acids, creating a structure which is in general helical.

**Tertiary structure** – The overall organisation of the complete polypeptide chain, including the interactions of different secondary structural elements.

**Quaternary structure** – The interaction of complete polypeptide chains to form a molecule composed of several chains.

Quaternary structures often show exact or approximate symmetries relating different peptide chains in a molecule. Tertiary structures also often include two or more similar structures within the same polypeptide chain, leading to the suggestion that more complicated protein structures have often evolved by gene duplication from simpler structures.

While the structures of hundreds of soluble proteins are now known, much less is known about proteins which reside in membranes. In a very few cases well-ordered three-dimensional crystals have been prepared, and the structures determined by conventional x-ray diffraction techniques. In a few other cases, ordered two-dimensional arrays of proteins can be isolated in membrane-bound form, and these specimens of monomolecular thickness are feasible for study by electron microscopy and electron diffraction.

The fundamental limitation on the study of very small biological specimens is the problem of radiation damage. The energy transferred to the specimen in observing it is so great, for both x-rays and electrons, that a high resolution view of a single molecule would vaporise it, breaking many covalent bonds in the process. Electron microscopy of single structures is never likely to yield an interpretation at atomic resolution, but where the structure is highly repetitive, processing of the images of molecular arrays improves the quantity of data available. This gives insight into the reasons why crystallography can produce detailed results, where microscopy fails : it is fundamentally a matter of spreading the radiation, and the consequent damage, over a larger number of individual units. Many radiation damage problems can be overcome by the use of neutrons, which give much more scattered energy than the energy absorbed in the sample, but which scatter much more weakly, requiring larger specimens and more expensive detectors.

At large facilities in the future, we should expect to see

- successful structural study of larger and more complex structures;
- the exploitation of absorption effects (MAD and XAS) to give more structural information;

- study of very short-lived structures, such as intermediates in muscle contraction or in enzyme activity;
- a better understanding of the dynamic properties and vibrational modes of biological specimens;
- deeper insight into the properties of specimens in solution, and of the effects of the solvent on stability and kinetic properties;
- the overcoming of radiation damage problems, by completing the data collection before the molecule has had time to fall apart;
- the study of much smaller specimens than has been possible hitherto, widening the range of structures which can be studied.



# CHAPTER VIII

## MACROMOLECULES IN DILUTE SOLUTIONS

H.B. STUHRMANN

## VIII.1. Contrast

"Suppose a region [= volume] v of constant shape to be occupied by the molecule which for the present purposes is defined as the region into which the salt does not penetrate when a salt solution is substituted for water. It is assumed that the density of the liquid outside v is uniform. The effect on the value of F [= structure factor] of increasing density everywhere outside v is equivalent to that of decreasing density by an equal amount everywhere inside v, since a uniform distribution of density throughout the cell has no effect on F. It follows that the values F(water) - F(salt) are the F values for a region v of uniform density equal to the difference between the electron concentration of the salt solution and water."

This argument was introduced by Bragg and Perutz (1952) to explain reversible changes in the intensities of low order x-ray reflections from a haemoglobin crystal and to deduce from these the shape and orientation of the haemoglobin molecule occupying the volume v within the unit cell. It is also a description of what became known later as contrast variation in small-angle scattering (Stuhrmann and Kirste, 1964).

Following this idea, the scattering density $\rho(r)$ of the dissolved macromolecule which effectively contributes to the observed scattered intensity (short: the effective scattering density) is

$$\rho(r) = \rho(r)_{solute} - \rho(r)_{solvent} \qquad \text{(VIII.1)}$$

$$= \rho(r)_{solute} - \rho_{solvent}.$$

The quantity F(water) - F(salt) used by Bragg and Perutz is the Fourier transform of $\rho(r)_{solute} - \rho_{solvent}$. In (VIII.1) we have assumed, as did Bragg and Perutz, that the density of the solvent is uniform outside the volume of the dissolved particle. Or

$$\rho(r) = \sum b_i \, \delta(r - r_i) - \rho_{solvent} \; v(r)_{particle} \qquad \text{(VIII.2)}$$

where $v(r)_{particle}$ (the index is suppressed in the following) defines the shape of the volume of the dissolved particle with $v(r) = 1$ inside the volume occupied by the particle and zero elsewhere (a more precise definition is given below). $b_i$ is the scattering length of the i-th atom at the position $r_i$. The index i runs over all atoms of the particle, e.g. in proteins, from 1 to some thousands.

$\rho$ is the average value of $\rho(r)$. Both $\rho$ and $\rho(r)$ represent contrasts. The latter is the excess scattering density in a volume element of the solute particle at r whereas the former refers to the whole particle. With this definition of the

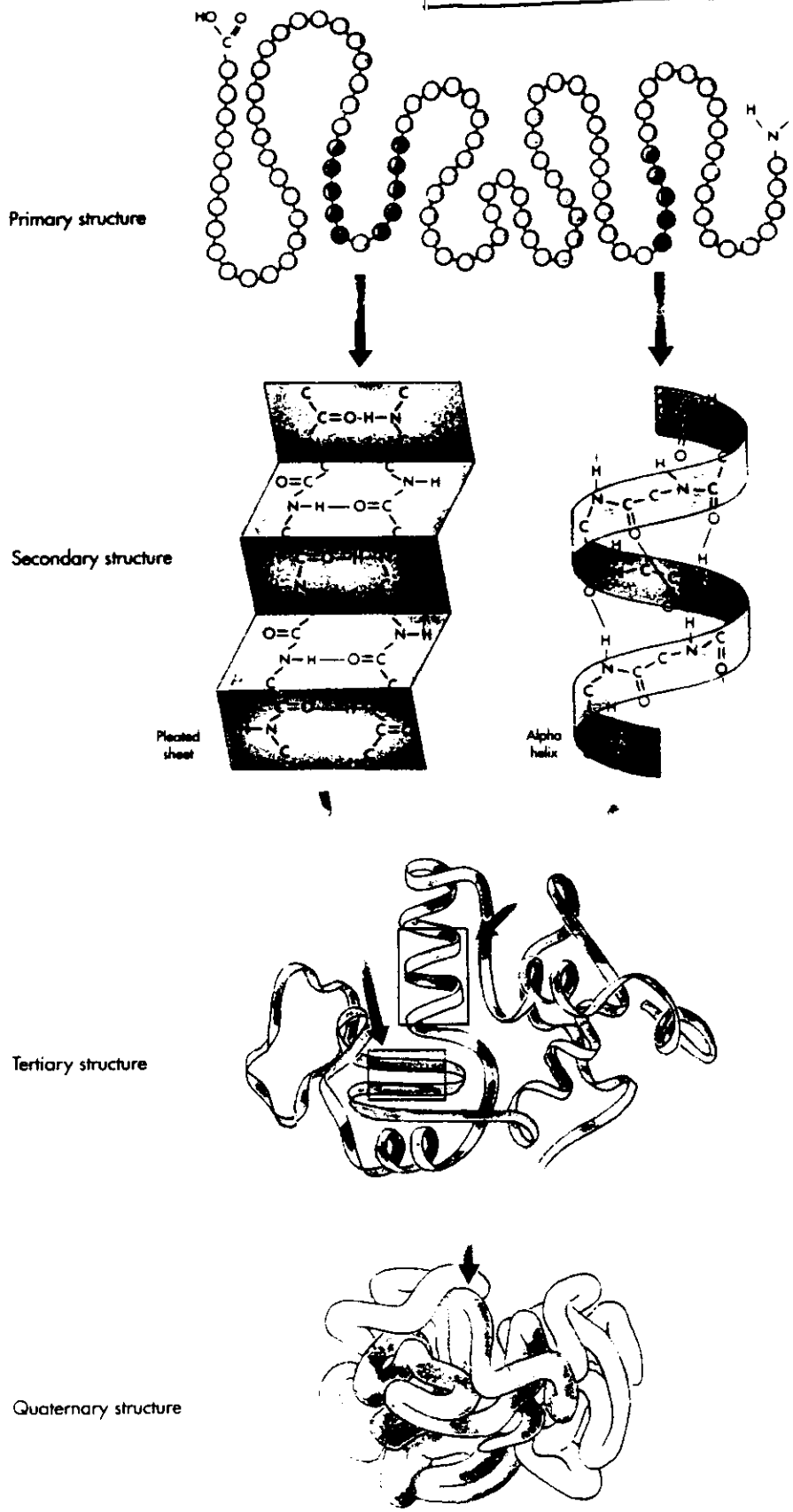


**FIGURE 2-23 How primary structure determines a protein's shape.**
The amino acid sequence of the enzyme protein lysozyme, called its *primary structure,* encourages the formation of hydrogen bonds between nearby amino acids, producing coils and foldbacks called the *secondary structure.* The lysozyme protein assumes a three-dimensional shape like a cupped hand; this is called its *tertiary structure.* Many proteins (not lysozyme) aggregate in clusters called the *quaternary structure* of the protein.

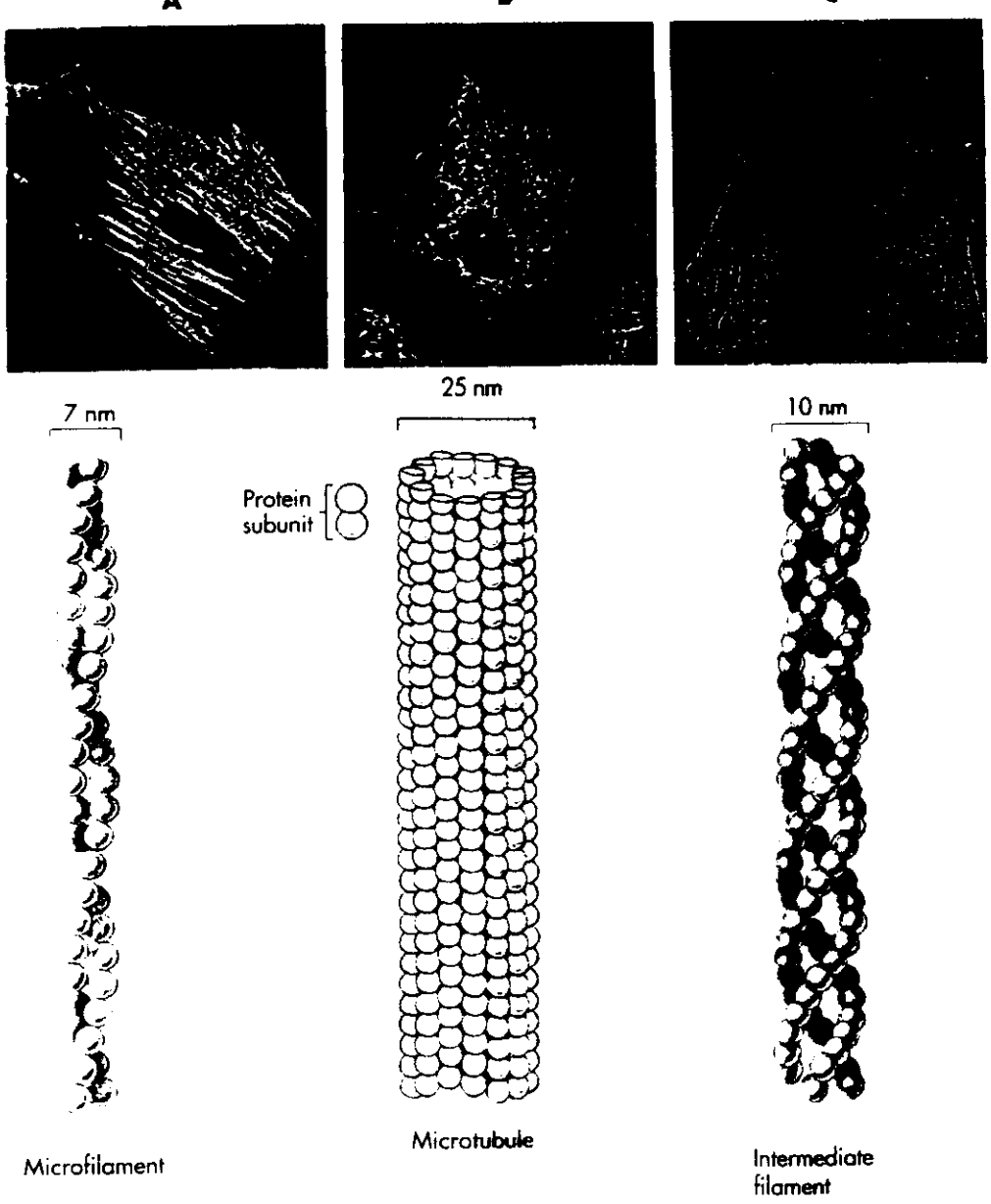


**FIGURE 3-8 Molecules that make up the cytoskeleton.**
**A** Microfilaments run parallel to the cell membrane in bundles.
**B** Microtubules are composed of a spiral array of protein subunits. The microtubules in the micrograph radiate from an area near the nucleus (the dark region in the center). Microtubules provide intracellular support in the nondividing cell.
**C** Intermediate filaments are probably made up of three subunits that are wound together in a coil, interrupted by uncoiled regions. In a skin cell, such as the one shown, intermediate filaments form thick, wavy bundles that probably provide structural support.

are also part of this "skeleton" of the cytoplasm. Together these three types of protein fibers provide the cell with mechanical support and help anchor the organelles. They also help move substances from one part of the cell to another. The filaments forming the highway in the chapter opener photo are microtubules found within nerve cells.

The cytoskeiton is a network of filaments and fibers within the cytoplasm that helps maintain the shape of the cell, move substances within cells, and anchor various structures in place.

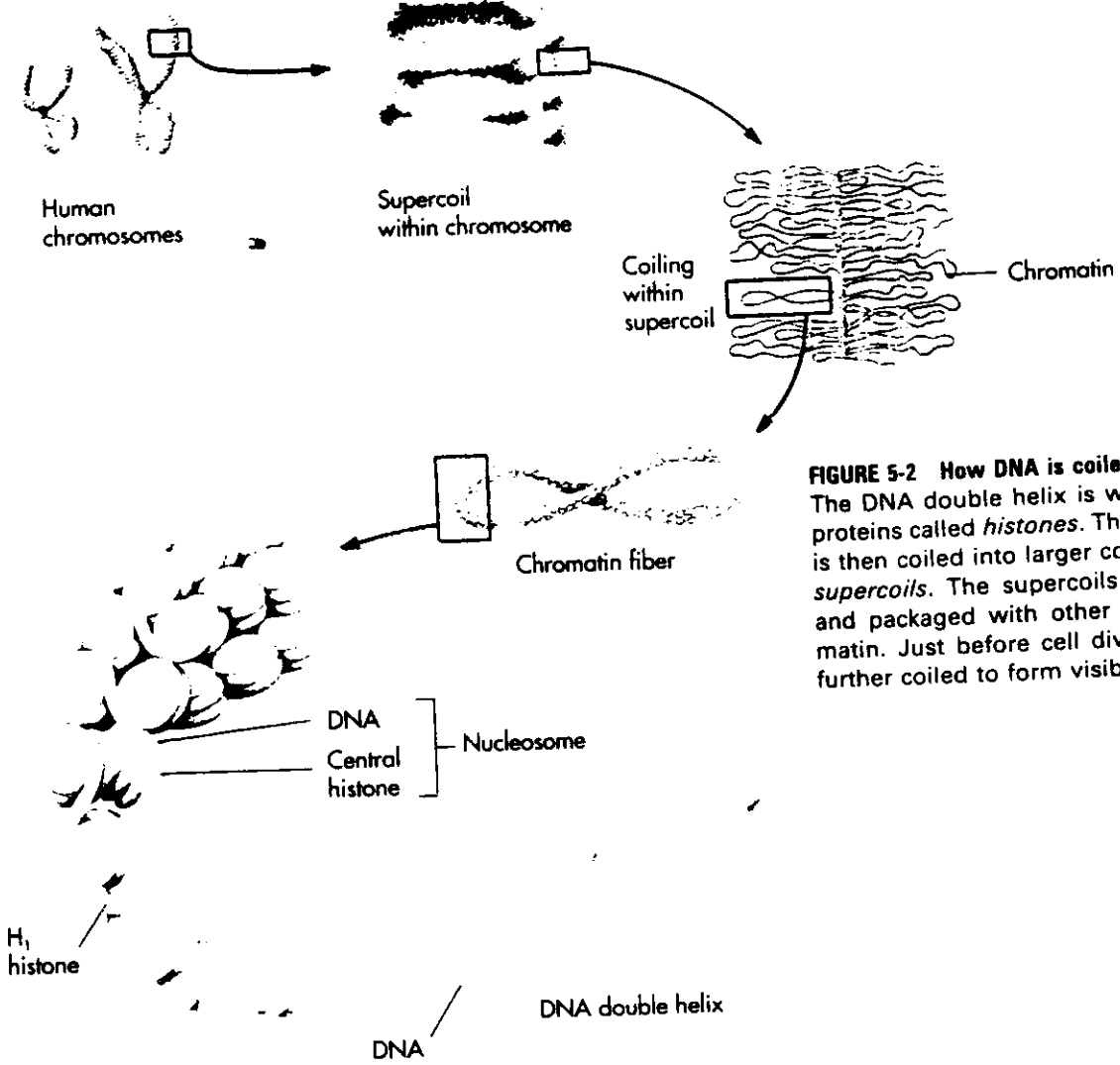


**FIGURE 5-2 How DNA is coiled within chromosomes.**
The DNA double helix is wrapped around special proteins called *histones*. The DNA-histone package is then coiled into larger coils appropriately called *supercoils*. The supercoils are themselves coiled and packaged with other proteins to form chromatin. Just before cell division, the chromatin is further coiled to form visible chromosomes.

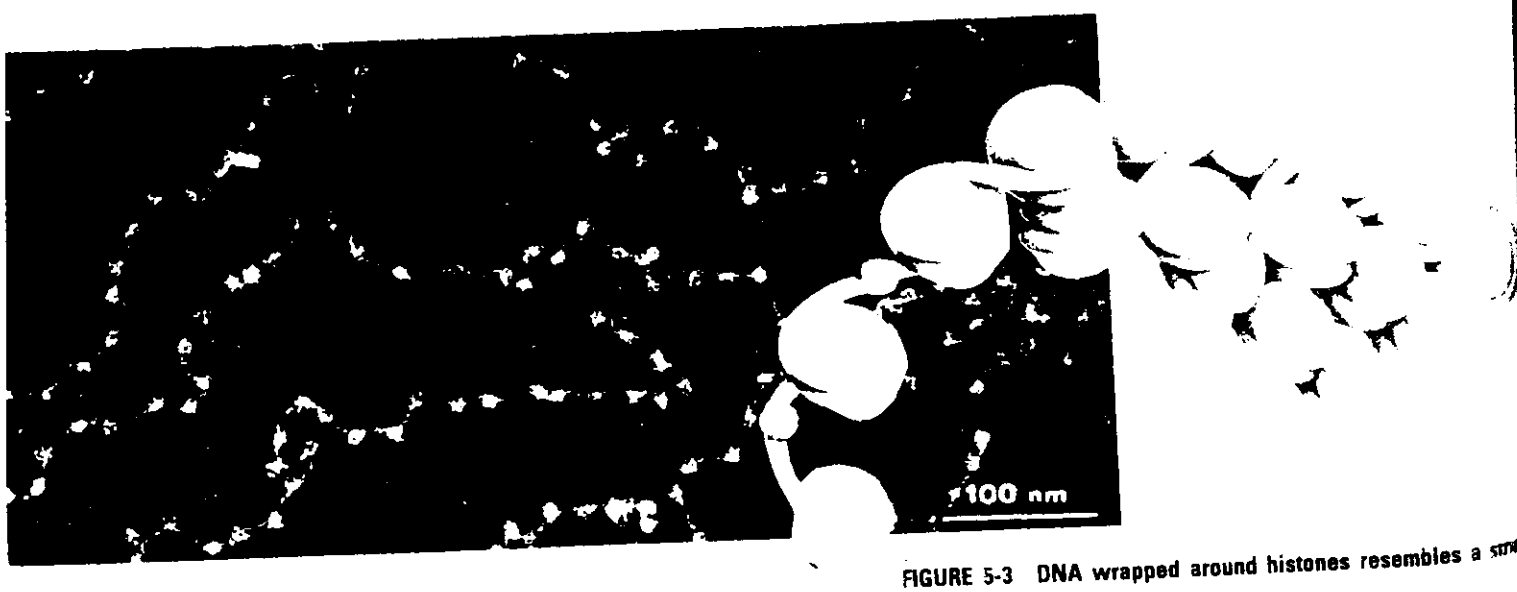


**FIGURE 5-3 DNA wrapped around histones resembles a string of pearls.**
The electron micrograph is of rat liver DNA

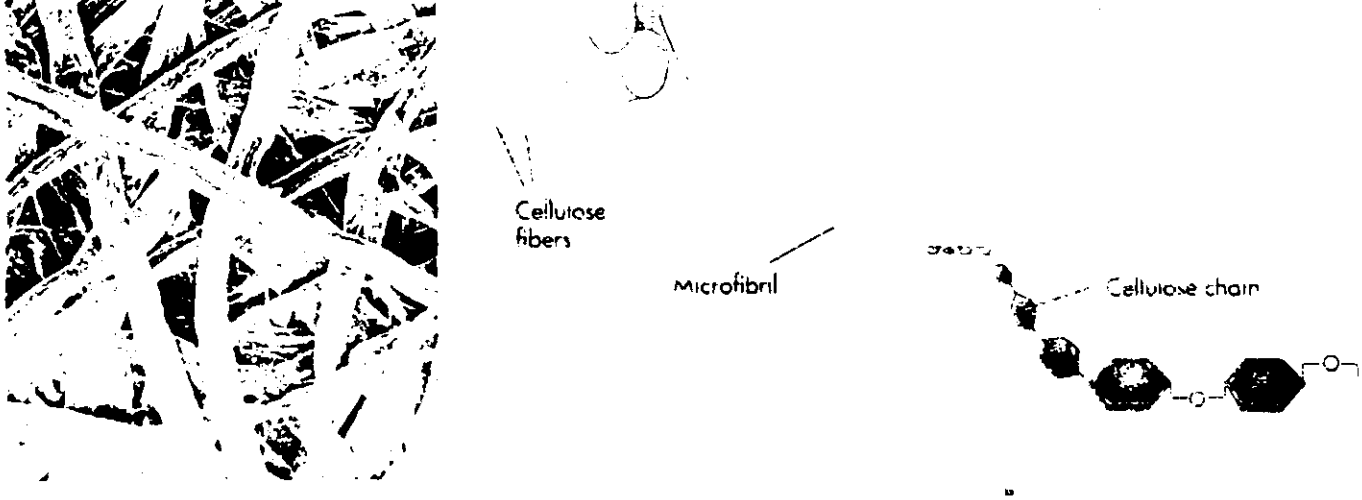


**FIGURE 2-17 A journey into wood.**
The jumble of cellulose fibers *(left)* is from a ponderosa pine. Each fiber is composed of microfibrils, which are bundles of cellulose chains. Cellulose fibers can be very strong, which is one reason wood is such a good building material.

The chief component of plant cell walls is a polysaccharide called **cellulose.** Cellulose is chemically similar to amylose but is bonded together in a way that most organisms cannot digest (Figure 2-17). For this reason, cellulose works well as a biological structural material and occurs widely in this role in plants. The structural material in insects, many fungi, and certain other organisms is a modified form of cellulose called **chitin** (Figure 2-18) Chitin is a tough, resistant surface material that is also relatively indigestible.

## Fats and lipids

When organisms store glucose molecules for long peri they usually store them as **fats** rather than as carbohydr Fats are large molecules made up of carbon, hydrogen. oxygen as are the carbohydrates, but their hydrogen to gen ratio is higher than 2 : 1. For this reason, fats cor more energy-storing carbon-hydrogen bonds than ca hydrates. In addition, fats are nonpolar, insoluble molec so they work well as storage molecules

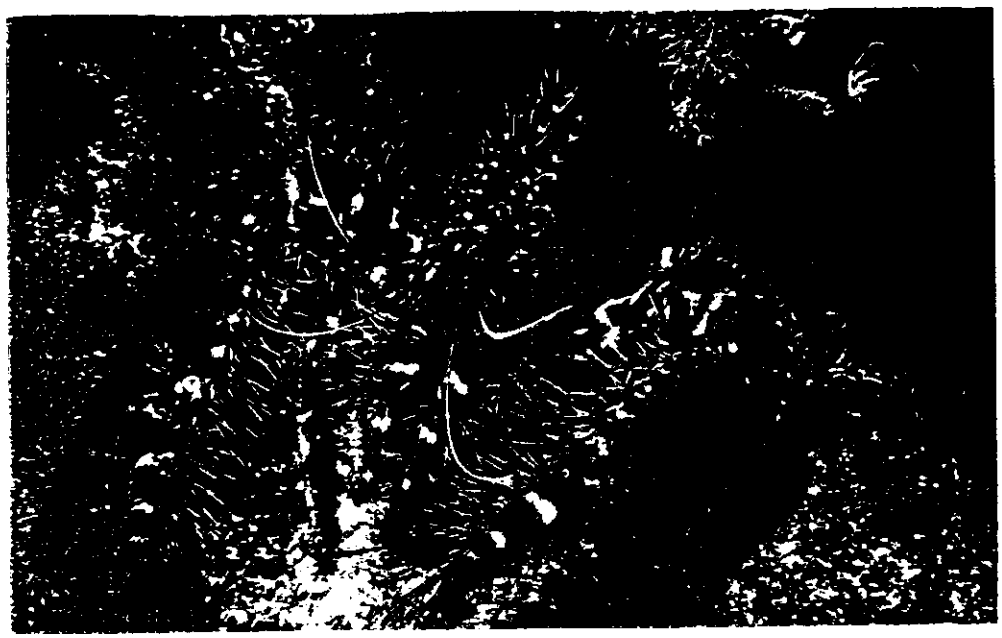

**FIGURE 2-18 Chitin.**
Chitin is the principal struc element in the external s tons of many invertebr such as this lobster.

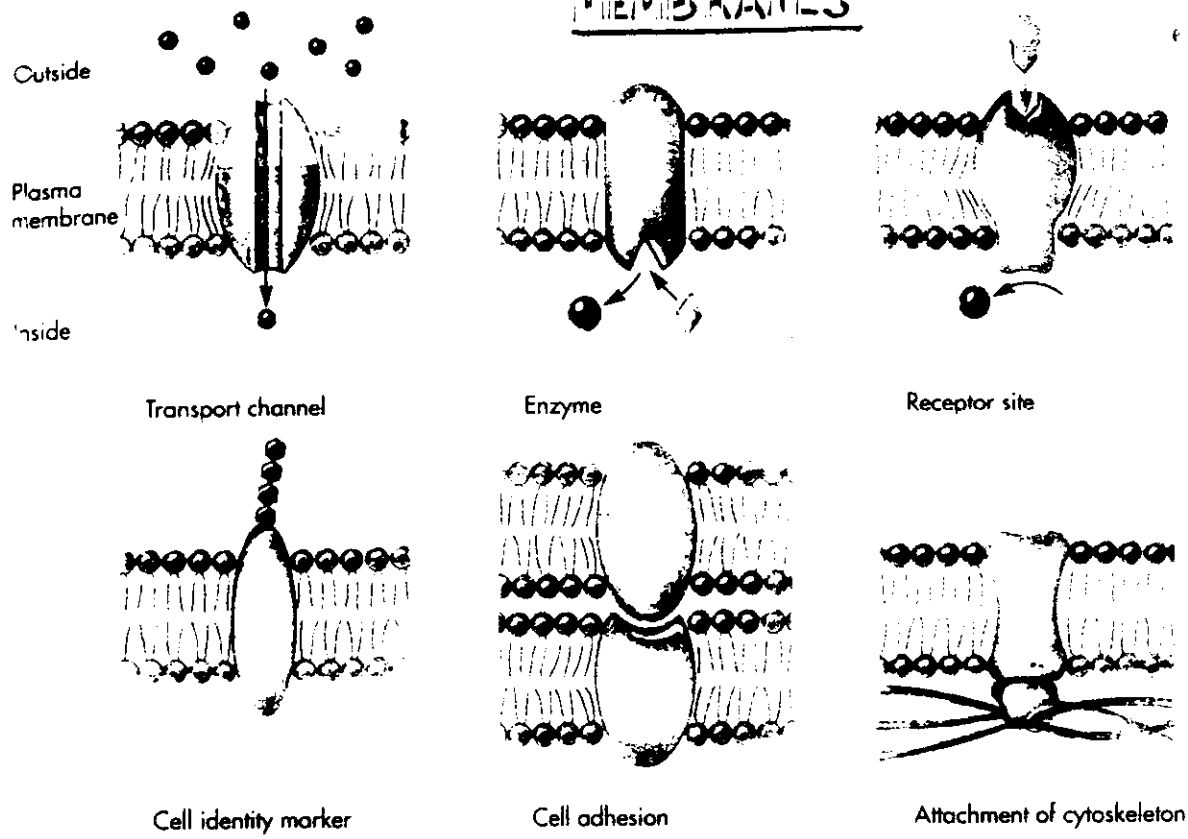


**FIGURE 4-3 Functions of plasma membrane proteins.**
The different proteins shown *(purple shapes)* perform many important functions. Some proteins act as *channels* through which certain substances enter and leave cells. Enzymes help speed up chemical reactions (see Chapter 6). Some proteins act as *receptor sites,* which bind specific chemicals. This binding prompts the cell to begin a specific function, such as the synthesis of a hormone. *Cell identity markers* are proteins that let other cells in the body know that they are not foreign invaders. Still other proteins perform structural roles: some proteins serve as *attachment sites* for other cells so that cells stick together, and other proteins anchor a cell's cytoskeleton in place.

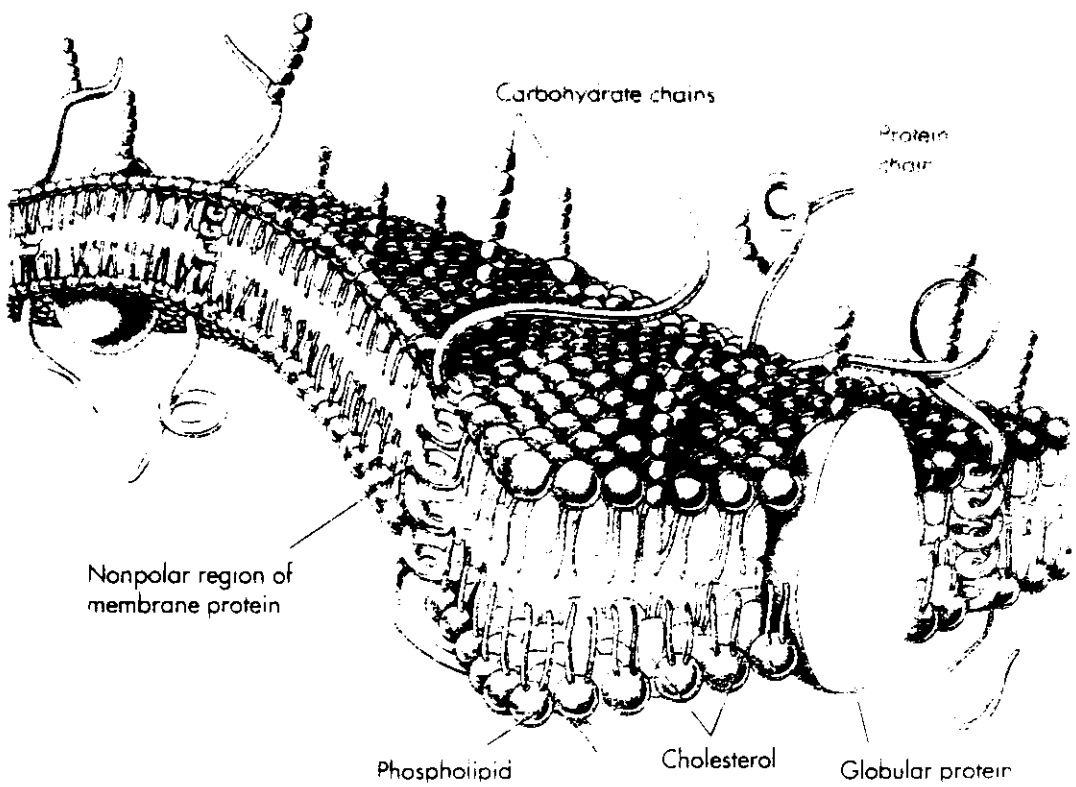


**FIGURE 4-4 Cell identity markers are found on the surface of the membrane.**
The purple tail-like structures shown in the diagram are proteins that enable the cell to interact with its environment

# 2. Basic knowledge for scattering by biological materials

| | | |
|---|---|---|
| Scattered amplitude | : | $A(\vec{S}) = \mathcal{FT}(\rho(\vec{r}))$ |
| Scattered intensity | : | $I(\vec{S}) = \lvert A(\vec{S}) \rvert^2$ |

- Case of the distribution of identical objects in the same orientation

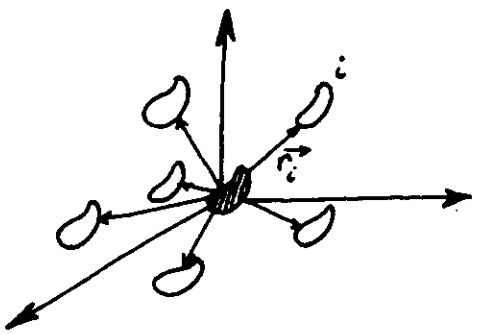


$$\rho(\vec{r}) = \left( \sum \delta(\vec{r} - \vec{r}_i) \right) * \rho_{obj}(\vec{r})$$

↑ position function $\mu(\vec{r})$

$$A(\vec{S}) = \mathcal{FT}(\mu(\vec{r})) \cdot \mathcal{FT}(\rho_{obj})$$

$$\boxed{A(\vec{S}) = \mathcal{FT}(\mu(\vec{r})) \cdot F_{obj}(\vec{S})}$$

↑ { structure factor / form factor

$$I(\vec{S}) = \lvert \mathcal{FT}(\mu(\vec{r})) \rvert^2 \cdot \lvert F_{obj}(\vec{S}) \rvert^2$$

$$\boxed{I(\vec{S}) = Z(\vec{S}) \cdot \lvert F_{obj}(\vec{S}) \rvert^2}$$

↑ interference function $= \mathcal{FT}(z(\vec{r}))$

↑ distribution function
= probability to find an object at $\vec{r}$ when one is located at the origin

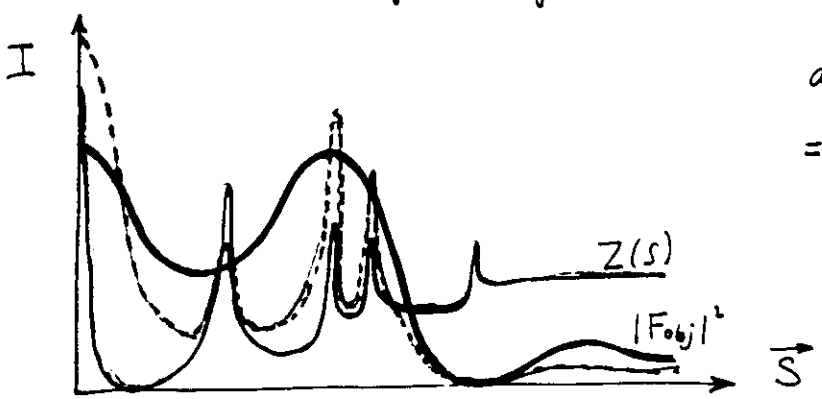

- crystal

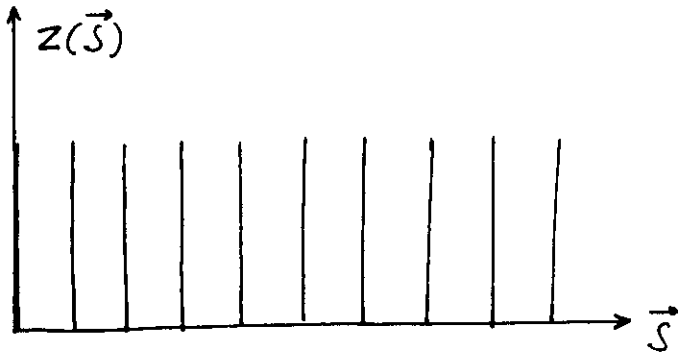


- liquid


- disordered system

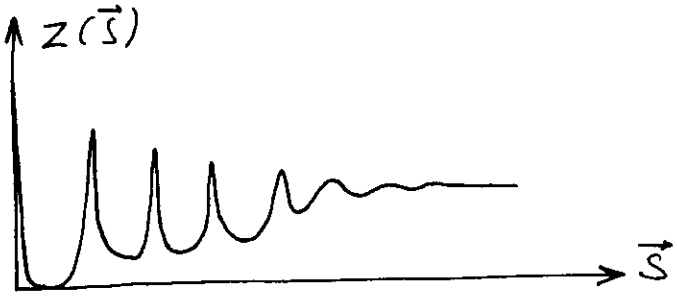

# 3. Interest of synchrotron radiation for biological materials

① flux
- Signal / noise ↑
- Sample damaging ↓

② angular resolution ↑ ⇒ large lattices

③ micro-beams ⇒ data Collection on small samples

④ low divergence ⇒ SAXS

⑤ tunability ⇒ MAD

⑥ temporal structure ⇒ time-resolved

⑦ coherence ⇒ imaging

# II Protein Crystallography

## 1- Overview

- major activity in S.R. centres
- routine technique
- industrial interest
- "lobby"

The various steps of a structure determination :

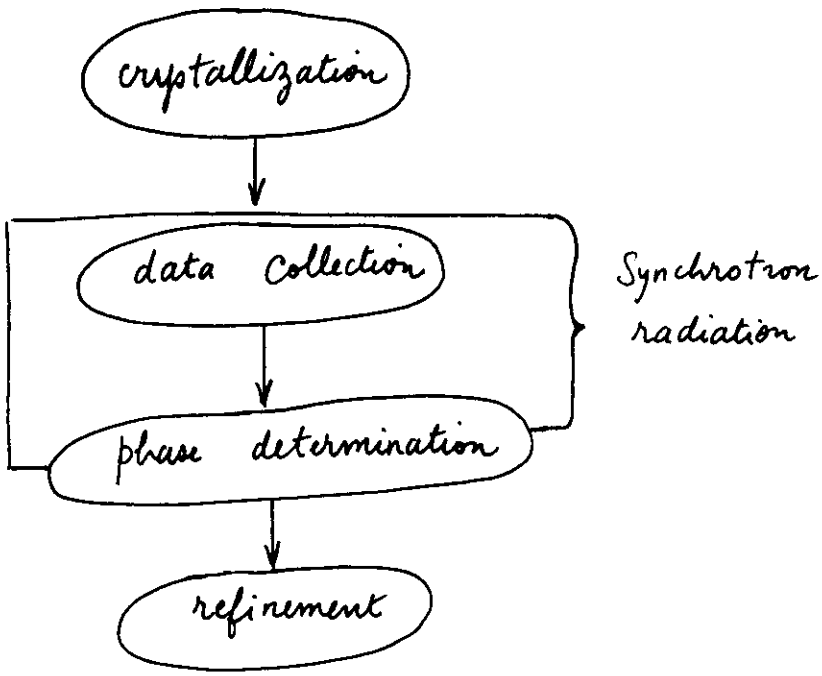

PROTEIN CRYSTALS

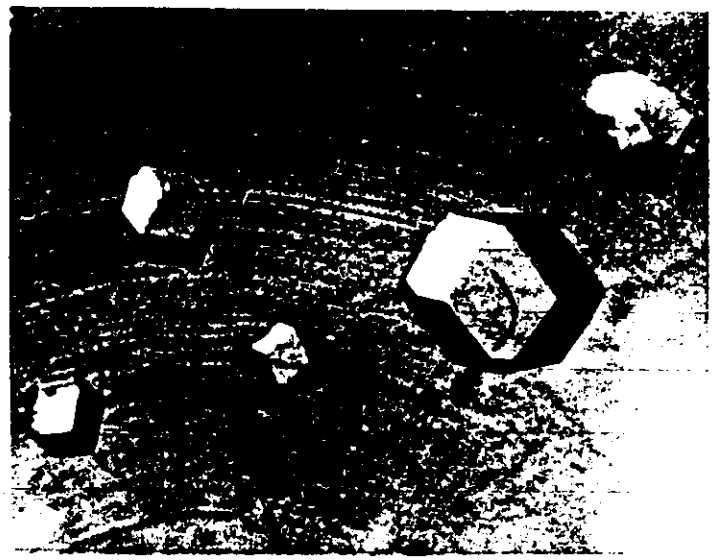

Figure 2: I23 cubic crystals of CPMV. The long axis of the rhombic dodecahedron for the largest crystal shown measures approximately 1mm.

EFFECT OF HEAVY ATOMS

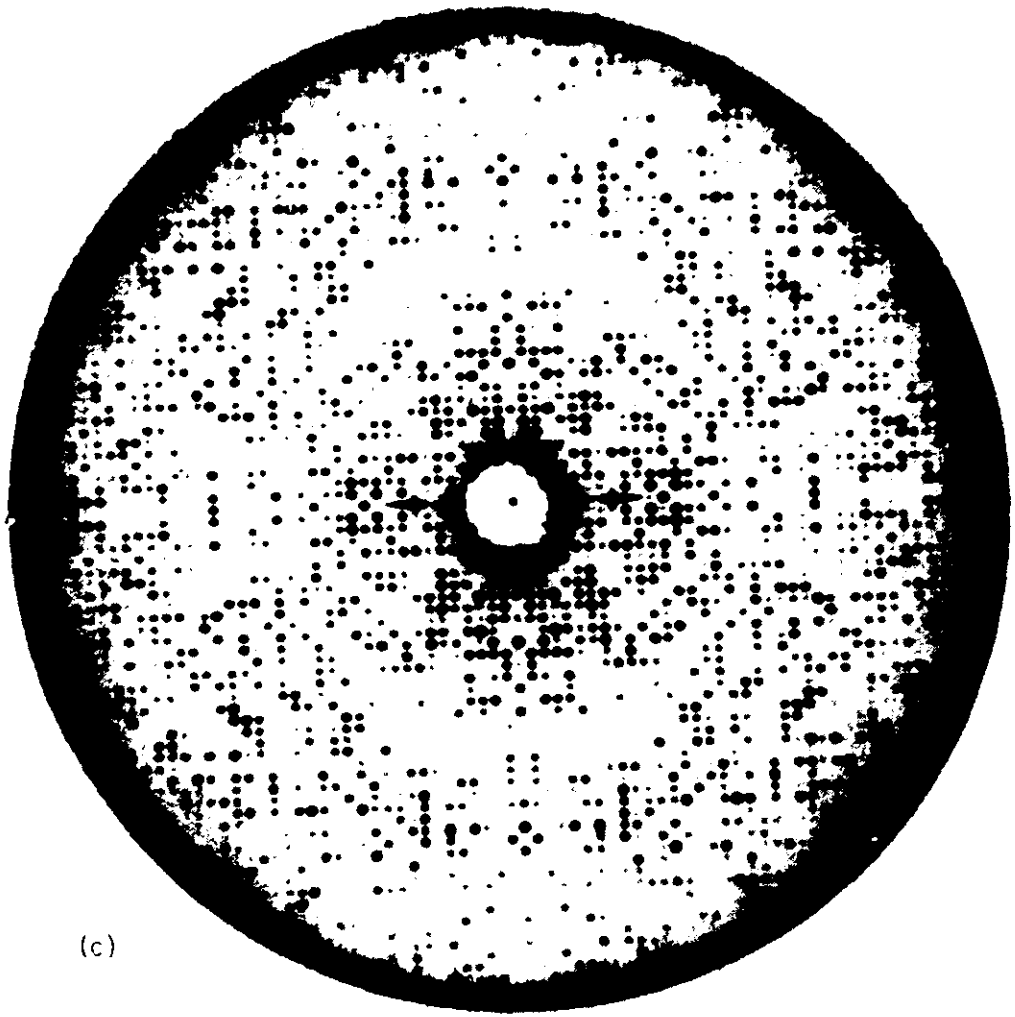

(c)

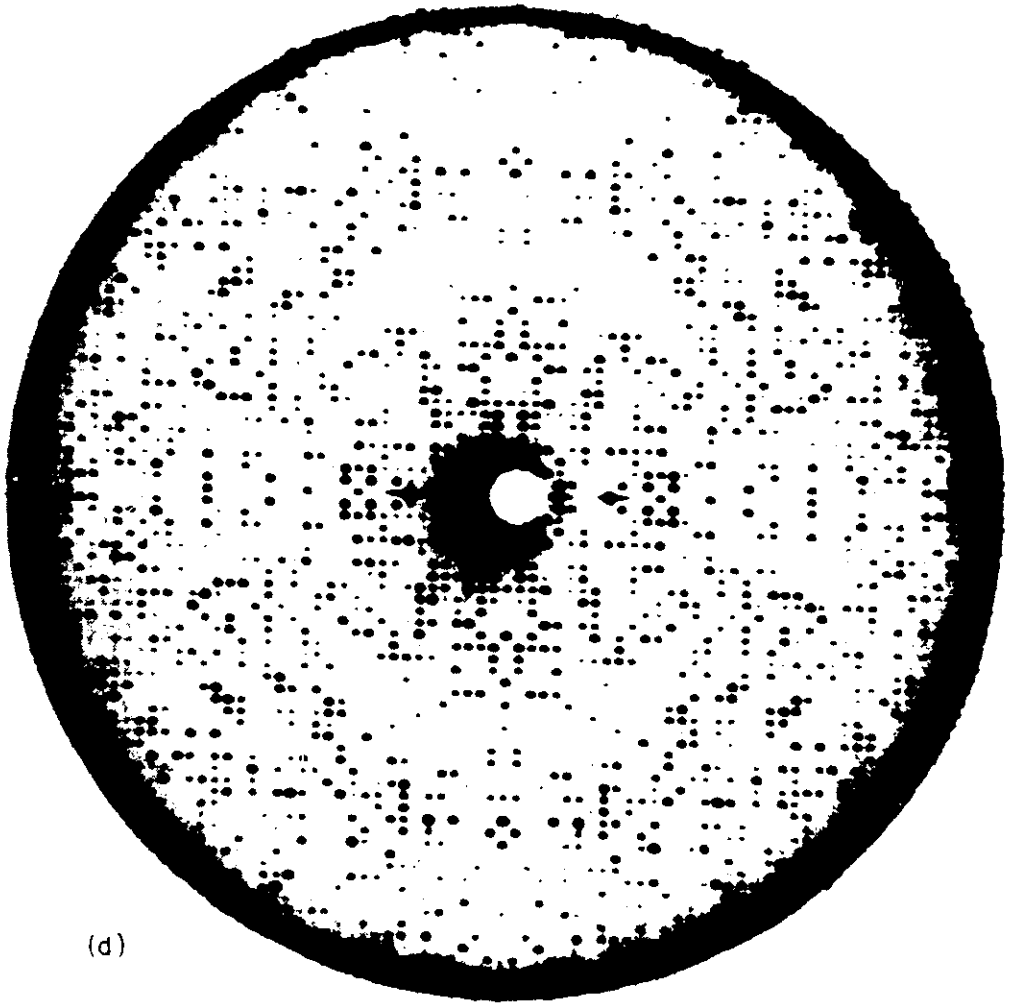

(d)

FIG. 6.2 X-ray precession photographs ($\mu = 15^{\circ}$) of native protein and heavy atom derivative crystals. (a) Native lysozyme (hh0 zone) (b) lysozyme p-chloromercuribenzene sulphonate (PCMBS); (c) native phosphorylase (h01 zone); (d) phosphorylase ethyl mercuri thio salicylate (EMTS).

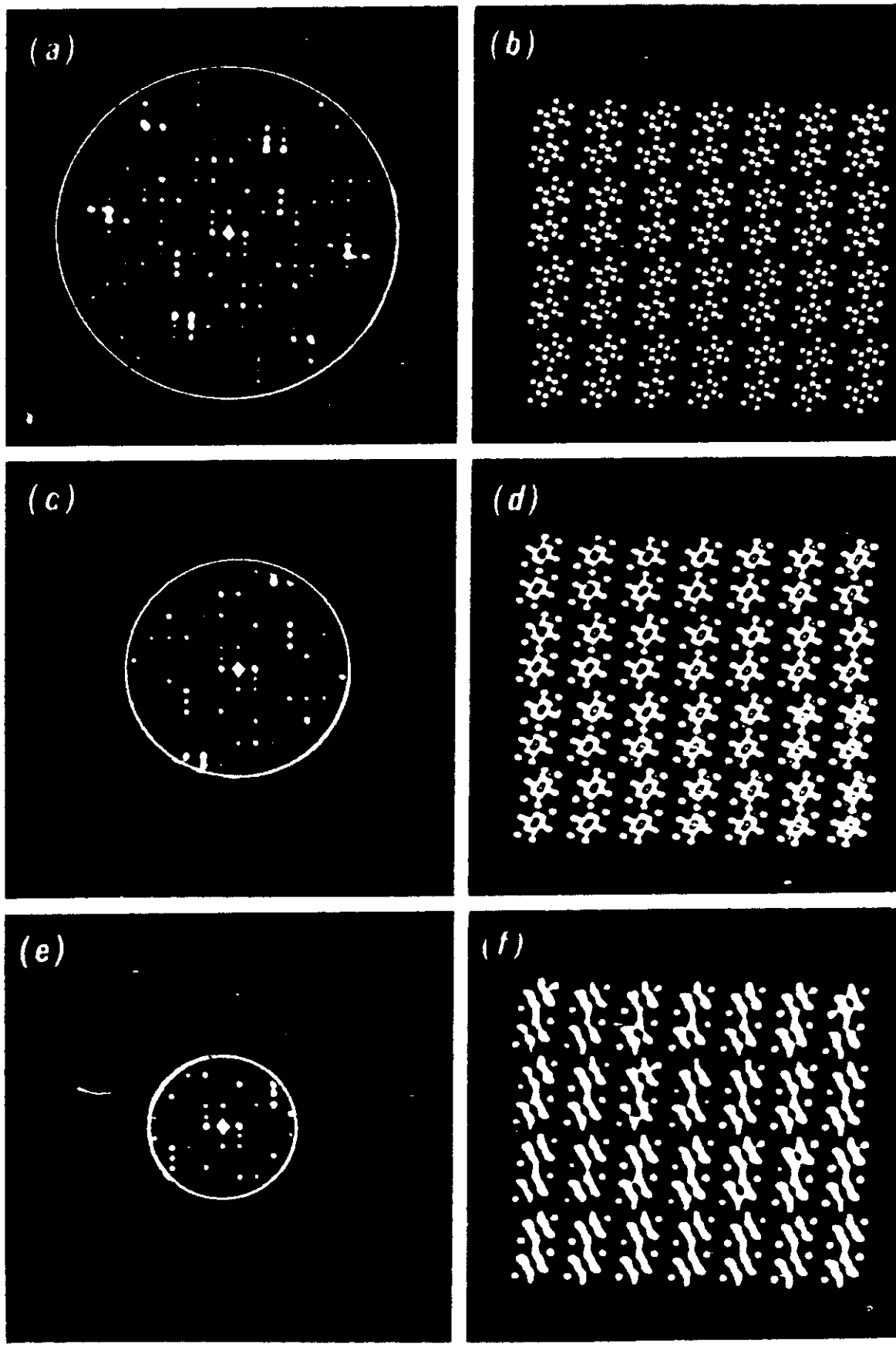


FIG. 5.8 Optical illustration of the effects of series termination in Fourier synthesis. The transforms of the portions of the diffraction patterns (a), (c), and (e) are shown in (b), (d), and (f) respectively. (Taylor and Lipson, 1964)

# CHAPTER XI

## MACROMOLECULAR CRYSTALLOGRAPHY WITH SYNCHROTRON RADIATION

R. FOURME

## XI.1. Introduction

Synchrotron radiation is used in X-ray crystallographic studies of biological macromolecules for several applications (monograph by Helliwell, 1992).

The first and basic class of applications is measurement of diffraction data with the highest possible quality, using existing crystals. Monochromatized radiation is used as it provides the highest signal to noise ratio and allows a complete survey of the reciprocal lattice.

A sub-class is concerned by the use of anomalous dispersion. Here, the emphasis is on accurate measurements of small differences between the intensities of Bragg reflections in anomalous pairs.

The second class of applications is kinetic crystallography and fast data collection methods, using either monochromatic or polychromatic radiation.

## XI.2. Accurate and high resolution data collection

The conclusion of the first steps of the analysis of every macromolecular structure by x-ray diffraction is the production of an ordered list of structure factor amplitudes $|F(h)|$ for the native crystal plus, generally, other lists for derivative crystals (Blundell & Johnson, 1976). The quality of final structural results, and often the possibility of solving the structure, are directly related to resolution, accuracy and completeness of these data.

Here, two pieces of equipment play a key role: the x-ray source and the area detector.

Acquisition of diffraction data with monochromatic radiation proceeds in general by recording a succession of diffraction images (frames) through adjacent rotations of amplitude $\Delta\phi$ of the crystal. Frames are partitioned into elements (pixels) and the pixel content is stored in digital form. Extraction of structure amplitudes is obtained by off-line analysis of the record of digitized frames, using for each reflection a three dimensional box (voxel) centred on the reflection at x, y and $\phi$ with dimensions defined by three integers m x n x p, where m and n are numbers of pixels defining the integration area on the detector (boxel) and p is the number of increments $\Delta\phi$. The total count in each voxel is obtained by summing contributions from contributing frames. The background is estimated from the count in an adjacent voxel free of diffraction signal and substracted from the total count to get the integral diffraction signal. This scheme has several variants, and is generally followed by post-refinement based on profile analysis of strong reflections. The best signal to noise ratio is obtained when the background

is integrated over an angular interval no larger than the reflection width, which is usually a fraction of a degree; in this respect, an increment $\Delta\phi$ of 0.05 - 0.1° is often most appropriate.

Table XI.1 contains basic considerations on data collection with monochromatic radiation (Fourme et al., 1991).

The first and second columns show respectively facts of biocrystallographer's life and main problems to be solved. In short, we are faced to (a) a large number of diffracted beams (b) spatially very close (c) with intensities spanning a dynamical range of 5 decades and peaking over a substantial background; we would like to measure these intensities with one to a few per cent accuracy. Crystals are subject to radiation damage which is dependent on wavelength, total dose and dose rate; for a given dose, a higher dose rate is in general beneficial; shorter wavelengths are favorable in all respects, improving accuracy - less absorption, better signal to noise due to longer crystal to detector distance - and the amount of information acquired per sample.

The third column shows the technical goals which we would like to achieve:

(i) an intense, quasi-parallel and highly monochromatic x-ray beam, which requires a source with a high spectral brilliance. In this respect, synchrotron sources outcome by far any other source. The total energy in a diffracted beam h for a crystal rotating at a constant angular velocity $\omega$ is given by:

$$E(h) = C\,\omega^{-1} I_0 \lambda^3 LP\, A\, (V_x/V_0^2)\, |F(h)|^2$$

where C is a constant, $I_0$ the intensity of the incident x-ray beam of wavelength $\lambda$, LP the Lorentz-polarization correction, A a correction for absorption, $V_x$ the volume of the sample, $V_0$ the volume of the unit cell and $|F(h)|$ the structure factor amplitude. When the expression of L is taken in account, E(h) is proportional to $\sim \lambda^2$. So, the need for high brilliance is comparatively more important for work at short wavelengths, below 1Å.

(ii) the reduction of various sources of parasitic scattering (crystal mounting, evacuated paths, beam catcher design....). A longer crystal-to-detector distance d is also useful in this respect. Due to the low divergence of the x-ray beam and the narrow width of Bragg reflections from most macromolecular crystals, the boxel size on the detector may be kept constant; in contrast, the solid angle subtended by the boxel decreases as $1/d^2$. Note that this argumentation is simplified, and results will depend on each instrumental configuration; during tests with an image plate detector, we found an effective gain in signal to noise with increasing values of d, but less than predicted by the inverse square law.

(iii) a good detector. This is a challenging problem for the physicist, because requirements are of a very high level and often conflicting. There are as yet no detector which can meet all requirements, so that the potential of even current synchrotron radiation sources is only partially exploited; but there are several lines of development to make improved detectors within the next few years. The data collection procedure just described is typical of electronic detectors such as multiwire proportional chambers (Kahn et al., 1986) or detectors based on a charge-coupled device (CCD) (such as developed by Westbrook et al., 1989 or by J. P. Moy and coll. in the ESRF Detector Group), in which the dead time between two frames may be a small fraction of the exposure time per frame. With current imaging plate detectors (Miyahara et al.,1986), the dead time due to readout and



| features | goals | solutions |
|---|---|---|
| global structural method | | intense X-ray beam, hence higher dose rate |
| several data sets (MIR) | collect vast amounts of data in short times | 2D detector with high efficiency even at short $\lambda$<br>high count rate<br>fast readout<br>low noise<br>large number of pixels<br>small point spread function |
| large number of reflections excited simultaneously | avoid spatial overlap | monochromatic and parallel beam<br>small oscillations per frame<br>large crystal-to-detector distance |
| static and dynamical disorder in crystal | | |
| diffuse scattering by crystal<br>various parisitic scattering | improve S/N = increase number of reflections per crystal | improve crystal mounting<br>evacuated paths |
| radiation damage in crystal | | short $\lambda$ (0.3 Å)<br>cryocrystallography |

Table XI.1. Data collection using a monochromatic X-ray beam, or how to improve the signal to noise ratio (S/N), i.e. the ratio of diffraction signal to non-diffraction signal (after Fourme et al., 1991, modified)

erasing is relatively long, and $\Delta\phi$ increments of typically 1° are used in order to get a reasonable duty cycle. Large increments tend to increase background and produce overlapping spots. These drawbacks are minimized using a Weissenberg camera with an imaging plate (Sakabe, 1991). This instrument combines sharp collimation of the beam, translation of the detector in one or two directions coupled with the crystal rotation, long crystal-to-film distance, made possible by the use of a large single plate or an array of plates and helium paths.

As a conclusion of table XI.1, it is important to note that it describes essentially *how to improve the ratio (diffraction signal/non-diffraction signal)*

Figure XI.1 shows a practical example of the comparison between several data sets obtained with various X-ray sources and various detectors with crystals from the same batch.

In conclusion, the future of accurate and high resolution data collection with synchrotron radiation is especially bright. For fundamental as well as applied research, the demand in structural results - now and extrapolated to at least the end of this century - is increasing quickly (Smith and Watenpaugh, 1991). Work that can be done with rotating anode sources may be improved by using synchrotron radiation. Synchrotron radiation has contributed to set new

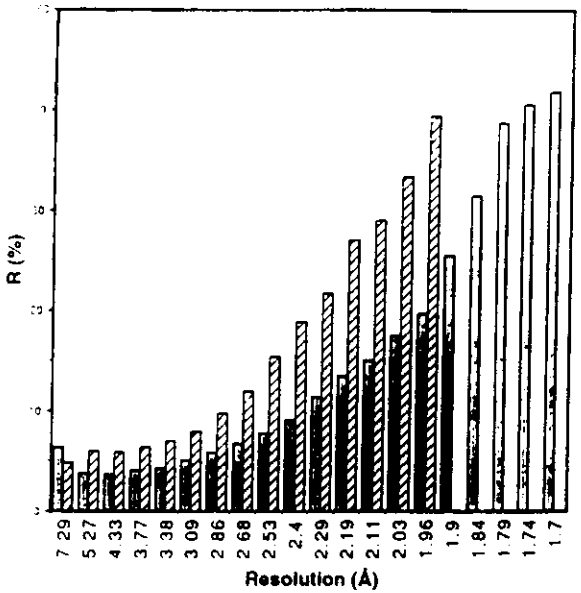


Fig. XI.1. — Crystals of the antigen-binding fragment of an immunoglobulin (Fab Hil); space group $P2_12_12_1$, a = 110.6 Å, b = 127.4 Å, c = 66.50 Å.
High resolution data collection using:
- a commercial multiwire proportional chamber and a rotating anode tube (hatched)
- a spherical drift proportional chamber (Kahn et al. 1986) and synchrotron radiation at LURE (grey).

$$R = \sum_h \sum_i |I_i(h) - \langle I(h) \rangle| / \sum_h \sum_i I_i(h) \times 100$$

where $I_i(h)$ is the ith measurement of the intensity of reflexion h and $\langle I(h) \rangle$ is the weighted mean of all measurements of I(h) (courtesy of F. Saul, Immunologie Structurale, Institut Pasteur, Paris).

standards in the quality of structural work. In this respect, one could consider synchrotron radiation as a basic supply as necessary and as trivial as laboratory fluids like water or liquid nitrogen. For more challenging projects (small crystals, ultra high resolution, complex macromolecular systems, very large unit cell...), undulators on 6-8 GeV third generation storage rings, with the fundamental emission in the X-ray range, are the real breakthrough. This has been demonstrated by protein cristallography experiments performed at the ESRF in early 1993, using the unfocused third or fifth harmonics from the ID10 undulator (ESRF report "Proteins on Troika", reporter M. Lehmann, february-march 1993).

## XI.3. Applications of anomalous dispersion

The spectral brilliance over a wide range of wavelengths, of synchrotron radiation sources has stimulated appplications of anomalous dispersion in many fields. Concerning macromolecular crystallography, familiar applications of anomalous dispersion to the phase problem (single isomorphous replacement



with anomalous scattering or SIRAS, multiple isomorphous replacement with anomalous scattering or MIRAS) can now be made optimal by appropriate wavelength selection (see Dumas et al., 1992 for an example of optimised SIRAS). A new method (multiwavelength anomalous diffraction or MAD) exploits anomalous diffraction from an ordered constellation of atoms to help solving the phase problem. Last, multiwavelength anomalous solvent contrast (MASC) exploits the wavelength-dependent scattering from anomalous scatterers dispersed in the solvent for determination of the macromolecular envelope and phasing of low resolution reflexions. MASC measurements can be analysed by a MAD-like formalism (Fourme et al., 1993) and experiments are in preparation at LURE.

### XI.3.1. Basic physics of anomalous dispersion

The x-ray scattering factor of an isolated atom is the amplitude of the wave scattered by this atom, taking as reference the amplitude of the wave scattered by a free electron located at the same point. Assuming that electrons in the atom are free, one gets the "normal" scattering factor $f^0$ which is the Fourier transform of the electron density distribution of the atom. $f^0$ is a real number which, at $s = 2\sin\theta/\lambda = 0$, is equal to the atomic number Z; it drops off rapidly with increasing values of s because the diffuse part of the electronic charge distribution becomes more and more ineffective in scattering.

In fact, the electrons are bound to the atom and, when submitted to the electromagnetic field, are not free oscillators. Using a simple classical mechanical model (see for example James, 1965), the atom scatters as a collection of damped oscillators whose natural frequencies are those of the absorption edges of the electronic shells. As a result, the atomic scattering factor f is a complex number. This effect is termed anomalous (or resonance) scattering. It is customary to write

$$^\lambda f = f^0 + {}^\lambda f' + i\,{}^\lambda f'' \qquad \text{(XI.1)}$$

where f' and f'' (the superscript $\lambda$ is implicit) are the real and imaginary anomalous dispersion corrections, respectively, of the normal scattering factor.

Let us recall a few important properties of f' and f'':

- f' is the (in-phase) dispersive term. f'', (the out-of-phase) absorptive term, is proportional to the product of the photon energy by the atomic absorption coefficient, so that a measurement of this coefficient will give, after proper scaling, the corresponding value of f''.

- f' and f'' are related through the Kramers-Kronig dispersion relation. This relation may be used to calculate f' from f'' values.

- f' and f'' are only weakly s-dependent, in contrast to $f^0$. In effect, anomalous dispersion is due to innermost electronic shells which, for atoms used as anomalous scatterers, have a radius much smaller than the x-ray wavelength. f' and f'' are usually assumed as independent of s. Subsequently, the relative importance of anomalous dispersion is increasing with the scattering angle.

- f' and f'' are wavelength-dependent. They vary most rapidly and reach their maximum magnitudes in the immediate vicinity of absorption edges. In fact, the domain of wavelengths close to absorption edges (say from 100 eV on the low energy side to 800eV on the high energy side) is of particular interest. The atomic

absorption spectra (and hence f' and f") displays features which are dependent on the molecular bonding environment and on the local structure around the atom.

- f' and f" are polarization-dependent

With polarized x-rays emitted by synchrotron sources, absorption spectra in the near-edge region depend on the orientation of the local chemical environment of the anomalous scatterer with respect to the polarization direction of the x-ray beam (see e.g. Templeton and Templeton,1985). This effect, which is averaged out in the case of a disordered sample, can be observed with a single crystal and may affect substantially both the edge position and the magnitude of the absorption. There is a related anisotropy in the anomalous scattering (pleiochroism). As an example, the anomalous scattering of selenium covalently bound to two carbon atoms is highly anisotropic in the vicinity of the K-edge of Se; at 12,654.9 eV, the effective f" lies between 0.8 and 7.7 electrons depending on the orientation of the crystal with respect to the polarization direction of the incident and diffracted x-ray beams (Templeton and Templeton,1988). A tensorial formalism to deal with the anisotropy of anomalous scattering has been developed by Templeton and Templeton (1982).

The f' and f" curves for isolated atoms of a few elements are shown in figure XI.2A. These examples illustrate several points:

- edge position for a given orbital occur at shorter wavelengths as the atomic number increases.

- apart from the energy of transition, all K edges are essentially alike and all L edges are alike.

- $L_{III}$ edges, which are associated with the six 2p electrons have anomalous scattering factor magnitudes about three times greater than those for K edges, which are associated with the two 1s electrons. As shown in fig XI.2B & XI.2C, the profiles observed for molecules are typically more strongly featured than the calculated ones for isolated atoms. These resonant features ("white lines"), which correspond to unoccupied molecular orbitals, can be about threefold greater than those expected for isolated atoms; of real practical interest are the 2p-5d resonances in elements from Cs to Pt, including the lanthanides.

Nearly all biocrystallographic experiments using anomalous dispersion have been performed using wavelengths between 0.6Å and 1.8Å (see table XI.2 for MAD experiments). Most elements used commonly as heavy atoms in MIR have a K or L edge in this window, plus many which are too light for use as MIR derivatives but are suitable as anomalous scatterers; such elements either occur naturally in macromolecules or can be introduced in a variety of ways. Experiments at long wavelengths are compromised by absorption; shorter wavelengths should become more readily usable with developments in sources, optics and detectors.

The anomalous scattering factors must be known for the analysis of MAD data to proceed. Initials values of f' and f" at the various wavelengths may be obtained from a combination of theory and experiment. Away from absorption edges, calculations from quantum mechanics provide reliable results (Cromer and Liberman, 1970). At wavelengths close to absorption edges, atomic absorption coefficients can be obtained from x-ray absorption spectra measured by fluorescence from the very crystal and the very x-ray beam used in the experiment



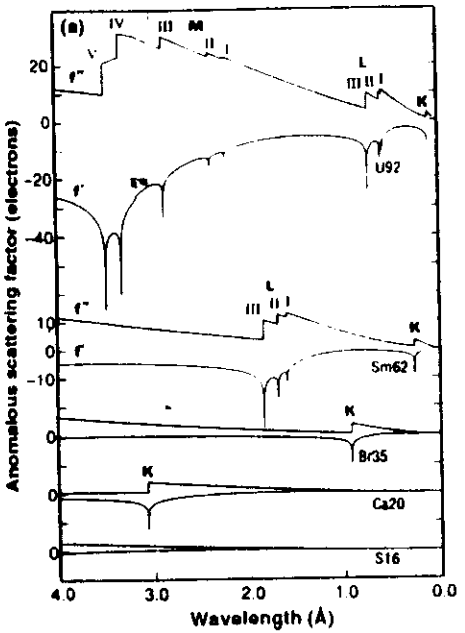


Fig. XI.2. — Anomalous scattering factor spectra for selected elements (after Hendrickson, 1991, modified).

(A) Calculated spectra for some isolated atoms. For each element, the imaginary component f" is drawn in the upper curve and the real component (f') in the lower curve. Origins for the five elements are displaced vertically as indicated.

(B) Experimental values derived from an x-ray absorption spectrum of Eu-(PhAcAc)3 (Ph, phenyl, and Ac, acetyl). The resonances from left to right are associated with the $L_{III}$, $L_{II}$ and $L_I$ absorption edges.

(C) Experimental values derived from an x-ray absorption spectrum of selenomethionyl thioredoxin from *E. coli*.

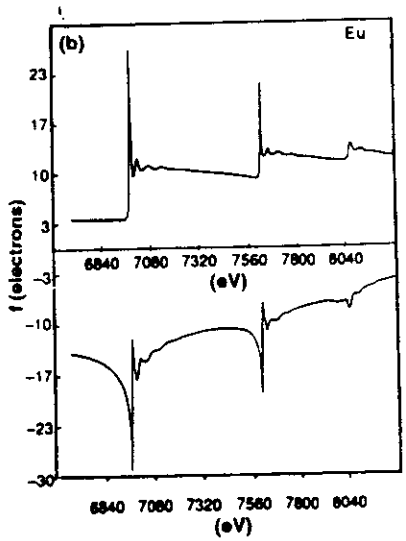


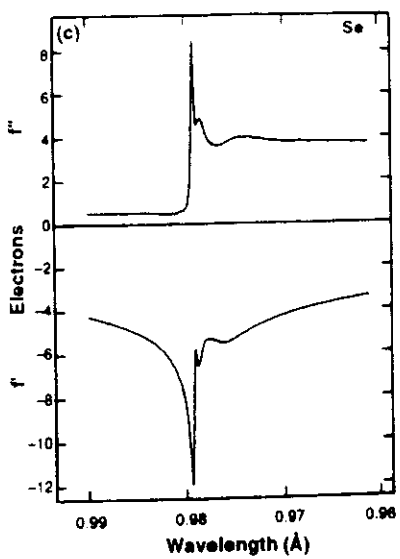

| Category | Typical element |
|---|---|
| Metalloproteins | |
| Transition metals | Fe, Cu, Zn, Mn |
| Other | Ca, Mo |
| Metal replacements | |
| Lanthanides for $Ca^{2+}$, $Mg^{2+}$ | Tb, Ho, Yb |
| Mercury for zinc | Hg |
| Ligands analogs | |
| Arnsenates, selenoethers, organohalides | As, Se, Br |
| Heavy-atom complexes | |
| Common protein derivatives | Pt, Au, Hg, U |
| Cluster compounds | Ta, W |
| Building-unit analogs | |
| Selenomethionyl residues | Se |
| Brominated nucleotides | Br |

Table XI.2. — Categories of MAD applications. An accessible x-ray range from 0.3 to 3.0 Å wavelengths covers the resonant transition from atomic numbers 20 (Ca) to 58 (Ce) for K edges and from 51 (Sb) to 92 (U) for $L_{III}$ edges. Apart from Ca, all of the likely candidates listed in the table fall within a range of wavelengths from 0.6 to 1.8 Å for which experiments are especially convenient. (after Hendrickson, 1991, modified).

(in the case of significant anisotropy effects, several spectra can be recorded for various orientations of the crystal and subsequently averaged to get an isotropic coefficient as a starting point). The reduction of these data to f" values involves background and scaling adjustments that can be tied to theoretical values calculated at points remote from the absorption edge. f' is calculated from f" by the Kramers-Kronig transformation. These starting f' and f" values may be refined against the experimental data; this is the case in MAD experiments, in which f' and f" values are often refined together with other global parameters (partial structure of anomalous scatterers) and local variables. This refinement procedure may give correct f' and f" values in case, for instance, of systematic errors due to monochromator missetting (e.g. Weis et al., 1991).

### XI.3.2. Effects of anomalous dispersion on Bragg Diffraction

We assume that the structure contains many ordered atoms (P) for which only normal scattering is detectable and a few ordered atoms (A) which have detectable anomalous scattering .

Reflections h and -h are known as Friedel mates, and in the absence of anomalous scattering they have identical intensities. With significant anomalous scattering, this is no longer the case, as shown in figure XI.3.

The actual difference

$$\Delta F_{\pm h} = |{}^{\lambda}F(h)| - |{}^{\lambda}F(-h)|$$



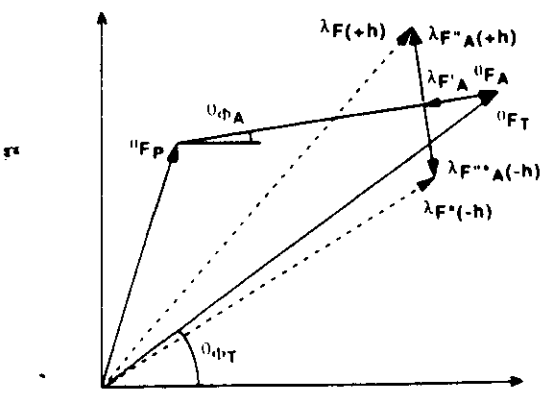


Fig. X.3. — Vector diagram in the complex plane of structure factors for one Bragg reflection h at one wavelength λ (see text). The structure factor for the total normal scattering, $|{}^{0}F_T| \exp {}^{0}\phi_T$, is the vector sum of normal scattering from atoms of type P and those from atoms of type A. The real and imaginary components of anomalous scattering are $^{\lambda}F'_A$ and $^{\lambda}F''_A$ respectively; when added to $^{0}F_T$, the resultant is the observed structure factor $^{\lambda}F$.

The complex conjugates of the structure factors from the -h reflection are also shown to illustrate the origin of the anomalous signal ($2\,^{\lambda}f''$). Note that the diagram pertains to the case for a single type of anomalous scatterer. (after Smith, 1991, modified).

between the structure amplitudes of Friedel mates or respective rotational symmetry equivalent of them, is designated as the Bijvoet or anomalous difference.

The second effect of anomalous scattering on the diffraction pattern is that the magnitudes of a given reflection differ with wavelength, because f' and f" are wavelength-dependent. We define a dispersive difference at wavelengths $\lambda_i$ and $\lambda_j$ as:

$$\Delta F_{\Delta\lambda} = |{}^{\lambda_i}F| - |{}^{\lambda_j}F|$$

where

$$|{}^{\lambda}F| = [\,|{}^{\lambda}F(h)| + |{}^{\lambda}F(-h)|\,]/2$$

Provided that the anomalous scattering is relatively weak compared with protein scattering, in the case of a single anomalous scattering type, the expected values of anomalous and dispersive ratio are (Hendrickson et al., 1985):

$$\text{rms}\,(\Delta F_{\pm h})/\text{rms}\,|F| = 2q\,{}^{\lambda}f'' \qquad \text{(XI.2)}$$

and

$$\text{rms}\,(\Delta F_{\Delta\lambda})/\text{rms}\,|F| = q\,|\,{}^{\lambda_i}f'' - {}^{\lambda_j}f''\,| \qquad \text{(XI.3)}$$

respectively, where rms means root mean square and $q = [(2N_T/N_A)^{1/2}Z_{eff}]^{-1}$. Here, $N_A$ is the number of anomalous scatterers per molecule, $N_T$ is the total number of nonhydrogen atoms in the molecule; $Z_{eff}$ is the effective normal

atomic scattering for a given value of s. For increasing values of s, $Z_{eff}$ decreases thus the expected diffraction ratios are enhanced. Note also that the scattering strength of a cluster of n anomalous scatterers is enhanced by a factor of $n^{1/2}$ if data are limited to spacings insufficient to resolve the individual atoms.

The anomalous and dispersive ratios are usually small. As an example, in the case of core streptavidin, a protein with 925 "normal" atoms and 1 Se atom as anomalous scatterer, and using three wavelengths around the Se K absorption edge, the calculated per cent ratios at s = 0 range from 0.7 to 2.5 (Hendrickson et al., 1989).

### XI.3.3. The Multiple Wavelength Anomalous Diffraction method (MAD).

#### XI.3.3.1. The phase problem

The phase problem is a severe rate-limiting step in macromolecular structure determination. Simply stated, the diffraction pattern of a crystal gives only the amplitudes of the Fourier transforms of the crystal contents, the phase angle is lost. In principle, provided enough unique diffraction amplitudes are known, the many constraints imposed by a knowledge of general molecular structure make the inversion of the known structure amplitudes, in the absence of any phase information, into real space electron density an overdetermined problem. However, direct methods that exploit this overdeterminacy are presently only available for relatively small molecules, although there is hope to extend eventually their application to the field of macromolecular structures ( for a panel of recent research in this domain, see Glusker, 1993). To date, the success of macromolecular crystallography for structures not related to ones already known is founded almost entirely on multiple isomorphous replacement (MIR). Differences in diffracted intensities from the derivative and native crystals are used to locate the heavy atoms. The calculated contributions from these centers serve as reference waves for evaluation of phases for the crystal structure. In general, the phase information from single isomorphous replacement (SIR) is ambiguous. Thus, MIR or other methods such single isomorphous replacement with anomalous scattering (SIRAS), solvent flattening or molecular averaging are used to resolve the ambiguity. But MIR phasing has its drawbacks. The preparation and interpretation of several heavy atom derivatives is a main factor limiting the speed and accuracy with which biological structures can be determined by x-ray crystallography. In this method, changes in diffraction patterns arise from chemical and structural differences, and strict isomorphism between the original structure and the derivative structure is exceptional. The ideal situation would be to rely on changes in the x-ray diffraction patterns arising from physical differences in a single sample. Anomalous scattering can indeed induce such differences. The corresponding method is called MAD (for reviews, see Fourme & Hendrickson, 1990; Hendrickson, 1991; Smith, 1991).

The principle of MAD phasing has been recognized more than 30 years ago (Okaya and Pepinsky, 1956). A landmark experiment was performed with x-ray tubes and a single-counter diffractometer (Hoppe and Jakubowsky, 1975); this work pointed out the need for a continuously tunable synchrotron radiation source and for an area detector. X-ray synchrotron sources became available in the early 1970. The development of EXAFS produced instrumentation and procedures which were directly applicable to MAD experiments. From EXAFS



and least squares refinement of crystallographic measurements, large resonance effects were demonstrated at L-edges of cesium (Phillips et al., 1978) and lanthanides (Templeton et al., 1980). Computational tests using these results showed the large potential of MAD methods (Phillips and Hodgson,1980). The realization of this potential has been fairly long to materialize, and this was due essentially to technical reasons. A MAD data collection is a complex experiment which requires extreme care; the main sources of trouble are: area detectors, crucial ingredients for which progress has been slow and uncoordinated, and which are still a main limiting factor; instabilities of synchrotron radiation sources, which became apparent when aiming at high accuracy data; the hectic pace of work and beam-time limitations at first generation synchrotron radiation facilities, which has not been optimal to perform long and careful experiments; and finally, the variety of problems associated with biological crystals such as radiation damage. The bulk of calculations performed during MAD data reduction is primarily concerned with the correction of these deficiencies. An algebraically exact theory of phase evaluation from MAD data, developed by Karle (1980) and implemented by Hendrickson (1985), has been central for the determination of most structures resolved up to now by the MAD method.

The first crystal structure solved by the MAD technique was parvalbumin from *Opsanus tau* (Kahn et al., 1985); the structures of a blue copper protein from cucumber (Guss et al.,1988) and of core streptavidin (Hendrickson et al., 1989) were more stringent tests of the MAD technique as the structures of the proteins involved were completely unknown. The incorporation of selenomethionine in place of methionine, suggested by Hendrickson (1985), can be a general vehicle for protein structure determination (Horton and Hendrickson, 1989); similarly, brominated bases can generally be used to provide suitable labels for nucleic acid structures and the structure of a DNA-drug complex has been determined by this method (Ogata et al., 1989). To date, a number of structure determinations have been reported in abstract or in extended form (table XI.3). MAD experiments are now available or in active developments at several synchrotron radiation facilities.

#### XI.3.3.2. Theoretical Foundation of MAD method

##### *XI.3.3.2.1. Introduction*

MAD is one of *de novo* phasing methods such as SIRAS or MIR. In these methods, the phasing procedure can be divided for clarity in two basic steps. The first step is the determination of the structural parameters of a subset of atoms which have, with respect to the rest of atoms, particular properties such as a large atomic number and/or significant anomalous scattering at the X-ray wavelength(s) used in data collection. The second step is the use of these parameters in the estimation of Fourier coefficients suitable for the calculation of an electron density map of the total structure. The MAD method relies on a subset of atoms with measurable anomalous scattering. This subset of atoms, A, is called hereafter the partial structure. The pertinent parameters of the partial structure are atomic coordinates, occupancies, temperature factors and anomalous components of atomic scattering factors at each wavelength. The first step of a MAD phasing is the determination of these parameters. The second step, for each reflexion h, makes a pivotal use of a reference structure factor *calculated*

| Molecule | #AS / kD | source | detector | dmin (MAD) | reference |
|---|---|---|---|---|---|
| **1/ Tests** | | | | | |
| Erythrocruorin | 1Fe / 16 | tube lines | scintil | 3.0 | 1975 |
| Rubredoxin | 1Fe / 6 | SSRL | films | 2.1 | 1977 |
| **2/ Published MAD phased electron density** | | | | | |
| Parvalbumin | 1.3 Tb / 10 | LURE | MWPC | 2.3 | 1985 |
| Cytochrome c' | 2Fe / (2x14) | PF | scintil. | 6.0 | 1986 |
| Azurin | 1Cu / 14 | CHESS | films | 3.0 | 1987 |
| Lamprey hemoglobin | 1Fe / 18 | SSRL | MWPC | 3.0 | 1988 |
| Ferrodoxin | 8Fe / 5.9 | SSRL | MWPC | 5.0 | 1988 |
| Cucumber basic protein* | 1Cu /11 | SSRL | MWPC | 3.0 | 1988 |
| Streptavidin * | 2Se / (2x14) | PF | scintil. | 3.3 | 1989 |
| DNA:chromomycin* | 4Br / (4x3.5) | PF | IP | 2.9 | 1989 |
| Ribonuclease H* | 3Se / 18 | PF | IP | 2.2 | 1990 |
| Cytochrome c-553* | 1Fe / 8.7 | PF | IP | 2.2 | 1990 |
| *Urechis* hemoglobin* | 2Fe / 31 | SSRL | MWPC | 3.0 | 1991 |
| Rat lecün CRD domain* | 4Ho sites / 27 | LURE | MWPC | 2.5 | 1991 |
| Tenascin FnIII domain* | 2Se | CHESS | IP | 2.5 | 1993 |
| **3/ Published MIR+MAD phased electron density** | | | | | |
| CD4 fragment (MIR+MAD) | 2Pt sites / 18 | Au lines | MWPC | 3.5 | 1990 |
| Interleukin 1α (MIR + MAD) | 3Se / 18 | PF | scintil. | 3.3 | 1990 |
| **4/ Data sets for MAD phasing under evaluation** | | | | | |
| Cutinase | Hg | LURE | MWPC | 1.7 | |
| Hemocyanin Og unit | Cu | PF/LURE | IP/MWPC | 3.0 | |
| Thioredoxin | Se,Cu | SSRL | MWPC | 3.0 | |

* structure solved by direct eveluation from MAD data, without any other information to develop the structure

Table X.3. — Results in MAD method

from these parameters in order to estimate the phase (and possibly modulus) of the Fourier coefficient to be used in the calculation of the initial electron density map. In all recent applications of MAD, the reference structure factor is the wavelength-dependent part of the structure factor of the partial structure, and the result is an estimation of the 'normal' part, ${}^0F_T$, of the structure factor of the total structure (the subscript T refers to the total structure, and the superscript 0 to a wavelength-independent quantity)( fig. XI.3). MAD has two advantages over SIRAS or MIR. First, it is a method in which the theory of phasing a wave from interference with several reference waves is strictly realised in practice, due to the fact that all measurements are made on a single sample. Second, the algebraic analysis described below gives the coefficients for the calculation of a Patterson map of the partial structure, instead of approximations of these coefficients.

*XI.3.3.2.2. Determination of the partial structure of anomalous scatterers*

We assume that the collection, analysis and scaling of multiple wavelength diffraction data have been performed, providing for each reflection h, n intensity measurements $|{}^\lambda F_T(\pm h)|^2$ (the superscript $\lambda$ is the wavelength of the measurement; $\pm h$ refers to the anomalous pair h, -h).The determination of the structural parameters of the partial structure may be performed using single wavelength data, although not in optimal conditions. In effect, the Fourier map calculated with coefficients $[|{}^\lambda F_T(h)| - |{}^\lambda F_T(-h)|]^2$ (Rossmann, 1961) is a sharpened Patterson that represents the distribution of interatomic vectors for the anomalous scatterers, but with a degraded signal to noise ratio (Karle, 1980). An intrinsically more powerful method relies on the analysis of multiple wavelength data by an algebraic procedure first proposed by Karle (1980). Karle expressed all quantities in terms of two structure factors ${}^0F_A$ and ${}^0F_P$ that have contributions from normal scattering only from respectively anomalous scatterers and the rest of the atoms. Hendrickson (1985) used the formulation in terms of ${}^0F_A$ and ${}^0F_T$ in his implementation of the algebraic method. With notations as in figure XI.3, equations are the following for a single type of anomalous scatterers:

$$|{}^\lambda F(\pm h)|^2 = |{}^0F_T|^2 + a(\lambda)|{}^0F_A|^2 + b(\lambda)|{}^0F_T||{}^0F_A|\cos({}^0\varphi_T - {}^0\varphi_A) \pm c(\lambda)|{}^0F_T||{}^0F_A|\sin({}^0\varphi_T - {}^0\varphi_A) \qquad \text{(XI.4)}$$

with:

$$a(\lambda) = ({}^\lambda f'^2 + {}^\lambda f''^2)/f^{02} \qquad b(\lambda) = 2({}^\lambda f'/f^0) \qquad c(\lambda) = 2({}^\lambda f''/f^0)$$

Least-squares procedures implemented to solve the system of equations (XI.4) (Hendrickson, 1985; Chapuis et al., 1985) take advantage of their essentially linear character. Given the coefficients a, b, and c determined by the scattering factors, each equation for the case of a single kind of anomalous scatterer has the form

$$y = p_1 + a\,p_2 + b\,p_3 + c\,p_4$$

and the system can readily be solved for the parameters $\{p_i\}$. These parameters are not independent, however, as they are related by a trigonometric identity such that

$$p_1p_2 = p_3^2 + p_4^2 \qquad \text{(XI.5)}$$

This constraint on the system can be imposed by introducing an undetermined Lagrange multiplier and continuing the non-linear constrained refinement to convergence. In this way, the three parameters, $|{}^0F_T|$, $|{}^0F_A|$ and $\Delta\varphi = {}^0\varphi_T - {}^0\varphi_A$, that characterize the MAD information are determined. Such an analysis is performed by the MADLSQ program (Hendrickson, 1985) for each reflection.

Although implementation of the linear least-squares phase of the procedure requires prior specification of scale factors and anomalous scattering factors, these values can subsequently be refined in the non-linear phase as global variables affecting the entire data set (Hendrickson, 1985). A program of this kind has proved effective in refining scattering factors from crude estimates (Hendrickson

et al., 1989). It is also possible to impose the constraint of equation (XI.5) implicitly through explicit refinement of the primary variables $|^0F_T|$, $|^0F_A|$ and $\Delta\varphi$.

From the set of $|^0F_A|^2$, the structure of anomalous scatterers can be solved by standard methods such as Patterson or direct methods, and then refined by least squares techniques. The entire set of $|^0F_A|$ values, excluding outliers (i.e. abnormal values), are valid data for this refinement in contrast to the limited subset of Bijvoet differences that can be used in the single-wavelength case (Hendrickson & Teeter, 1981). An alternative to refinement of the anomalous scatterer model against these $|^0F_A|$ estimates would be to refine directly against the set of $|^\lambda F|$ observations (Hendrickson, 1985). This scheme is like the phase refinement procedure used in isomorphous replacement (Dickerson et al., 1961), but here $|^0F_T|$ and $^0\varphi_T$ are refined as local parameters for each reflection and $^0F_A$ is expressed through the global parameters of the atomic model for anomalous scattering centers. In this context, it is possible to return to the general expression of algebraic equations for several anomalous scattering species and allow an arbitrarily complex structure of anomalous scatterers. A program called MADDST has been written to implement this procedure and to account for anisotropy in anomalous scattering (Fanchon and Hendrickson, 1989).

*XI.3.3.2.3. Estimation of phases*

The second step makes use of the reference waves from the partial structure to get estimates of $^0F_T$.

In the context of the algebraic analysis (Hendrickson, 1985), the phase $^0\varphi_A$ calculated from the refined model of the partial structure is used to derive $^0\varphi_T$ from the phase difference $\Delta\varphi$. The phase and amplitude of the Fourier coefficient $^0F_T$ are thus determined. Two electron densities based on weighted $^0F_T$ coefficients are traced with $^0\varphi_A$ calculated for the two enantiomorphs of the partial structure. The correct map is distinguished by chemical reasonableness or by symmetry considerations. Weights are based on residuals in the least squares fit of the phase equations to the observations.

Another approach is based on probability methods. Once the partial structure parameters have been obtained, there remains the problem that the resulting phase indications given by MAD (and other de novo methods) are most often ambiguous because of varying degrees of bimodality in most of the acentric phase probability distributions. The standard solution is to use centroid structure factors ( Blow & Crick, 1959) which minimize the root mean square error in the final map and may thus be viewed as a damage limitation measure. Following the description of Hendrickson and Lattman (1970), a Gaussian distribution is ascribed to errors of closure in $|F|^2$ values instead of $|F|$. A probability distribution function for the phase information is derived from the intensity measurements. Fourier coefficients used for the calculation of the electron density map have figure of merit-weighted moduli and centroid phases. The correct enantiomorph of the partial structure is selected as in the algebraic method. This approach has been used either with simulated MAD data (Phillips and Hodgson, 1980) or real data (Kahn et al., 1985; Harada et al., 1986; Korszun, 1987; Guss et al., 1988). Pahler et al. (1990) used it as an alternative way to derive weights for the $^0F_T$ Fourier synthesis in the algebraic analysis and showed that the probability distribution $P(\varphi)$ can be cast in the A, B, C, D representation of Hendrickson and Lattman (1970):

$$P(\varphi) = N\,(A\cos\varphi + B\sin\varphi + C\cos 2\varphi + D\sin 2\varphi) \qquad \text{(XI.6)}$$

The A, B, C, D formulation facilitates the combination of MAD information with information from other sources, such as isomorphous replacement, solvent flattening, non-crystallographic symmetry and partial models.

Instead of the calculation of the centroid phase, the latest version of this standard solution is the calculation of the real and imaginary components of the Fourier coefficients which will provide the best electron density map (Chiadmi et al., 1993).

Direct phase determination for macromolecular structure determination by entropy maximization and likelihood ranking is being gradually implemented. A status report and perspectives of this 'Bayesian programme' can be found in Bricogne (1993). As discussed in this article, this statistical theory, which encompasses all phasing procedures, may be important for MIR and MAD. Recourse to maximum-likelihood provides an optimal and definitive answer to the heavy atom parameter refinement in MIR (Bricogne, 1991). This approach can also be applied as well to the refinement of parameters in the MAD method where it provides a sounder statistical treatment than is currently available. In order to imlement it, a program has been written which can accomodate both MIR and MAD data, or any mixture of them (de La Fortelle et al., 1993). Maximum entropy and maximum likelihood methods can also be used for the systematic resolution of phase ambiguities, assuming that the phase information available at each stage from the MIR or MAD methods have been encoded by means of A, B, C, D coefficients. Further, because MAD exploits only one configuration of anomalous scatterers, it is unable to phase reflexions for which the transform of that constellation of scatterers is weak. A corollary to this observation is that, even in the most favourable circumstances, MAD would have to rely on some other procedure for propagating phase information, from those reflexions where it is strongly indicated, to those where it is essentially absent. Again, maximum entropy and maximum likelihood method will perform this task in an optimal fashion.

### XI.3.3.3. Instrumentation

In macromolecular crystallography, even when the anomalous effects are maximized, the changes in intensities are small: the scattering from the anomalous scatterers is typically a rather small perturbation of the total scattering, but, as seen previously, it is in differences between intensity values at different wavelengths and between the Bijvoet mates that the phasing power resides. Accurate measurements of small intensity differences is thus essential; achieving this goal depends on the interplay between a careful experimental design, a strategy for efficient acquisition of data with appropriate counting statistics, and care to minimize or correct systematic errors at various steps, from sample preparation and data acquisition to reduction of raw data.

*XI.3.3.3.1. X-ray source.* X-ray tubes have been used for MAD measurements. But the spectral brightness of synchrotron radiation is better suited for MAD work. The bending magnet radiation from several existing sources (at CHESS, NSLS, SSRL, Photon Factory, LURE, VEPP 3, DESY, SRS and ESRF) provide adequate flux for many experiments. Wigglers give enhanced flux and shift the spectrum to higher energy; accordingly, they extend the range of accessible absorption edges and they also can make third-generation, low energy sources, suitable for MAD (at ALS, MAX-II, SRRC, LNLS). Undulators on third generation, high energy sources (available currently at ESRF and later at SPRING 8 and APS) have a ultrahigh brightness in a restricted wavelength range which may be purposely adjusted for a given anomalous scattering species. In all cases, the stability of the beam is a critical point, especially for low emittance storage rings, in order to get a stable focal point, a constant polarization of the x-ray beam at the sample location and no wavelength shifts.

*XI.3.3.3.2. X-ray optics.* The optical system has specifications comparable to those of many EXAFS spectrometers: i) monochromatic beam with an energy band-pass of 1-2 eV; ii) free of higher order harmonics; iii) accurately and repeatedly tunable; (iv) fixed focal point. Designs of variable costs and complexities have been proposed to meet these requirements. The emphasis is on stability (thermal stability, mechanical stability, elimination of backlash, filtering of vibrations, beam-position monitoring etc...).

*XI.3.3.3.3. Goniometer.* A multi-circle goniometer is required to provide maximum flexibility. A vertical equatorial plane is optimal as the synchrotron beam is polarised in the horizontal plane. Axis movements must have angular steps of $10^{-3}$ deg, as usual in synchrotron radiation diffractometry. Slewing speeds should be as large as possible, as MAD measurements require frequent changes in crystal orientation, for instance to measure Friedel-related data. The intensity of the beam after the collimation system of the goniometer must be monitored. This monitor is used to rescale diffraction data collected with an x-ray beam of varying intensity; it may also be used to give the reference $I_0$ signal in fluorescence EXAFS experiments from which the variation of f" and f' in the near-edge region will be derived.

*XI.3.3.3.4. Detector.* The x-ray detector is the most important piece of equipment in a MAD setup. Both a single counter detector and area detectors have been used for successful MAD studies.

Single counter diffractometers have the advantage of flexibility, which is useful for complex data collection schemes, and provide a good signal-to-noise ratio because peak and background measurements can be optimised. The low efficiency is acceptable if the sample is stable and beam time available (e.g. structure of core streptavidin by Hendrickson et al., 1989)

Area detectors measure many reflections simultaneously, so that these devices are an integral feature of MAD experiments. Electronic area detectors (EAD) acquire diffraction images directly in digital form, like a single channel diffractometer; as the dead time between two frames is very short, the data collection can be subdivided into many frames, thus optimising the signal-to-noise ratio. Multiwire proportional chambers at SSRL( Phizackerley et al., 1986) or LURE (Kahn et al., 1986) have been used for high accuracy MAD measurements but they are presently count rate limited and not suitable for very short wavelengths. These defaults could be cured by microstrip technology, fast readout systems and pressurized detectors (for a review see e.g. Walenta, 1991). A commercial television detector is used at NSLS. Charge coupled device detectors have a high dynamic range, a high quantum efficiency and a small point spread function; a prototype system is available at NSLS (Westbrook et al., 1989) and another one, using an X-ray image intensifier, is being developed at ESRF ( Moy and Gibney, 1992). Imaging plates have several outstanding characteristics: unlimited count rate, large dynamic range, very uniform response, high efficiency over the whole useful wavelength range, small point spread function (Miyahara et al., 1986). The main default, which is perhaps more serious for MAD than for normal data collection, is the long processing time of each image. Various technical solutions have been proposed to overcome this problem: a carrousel of several detectors each with its built-in laser scanner, a fast plate exchanger or even a belt-type imaging plate (Sakabe, 1991).

*XI.3.3.3.5. Additional experimental apparatus* The degradation of crystals is a source of systematic errors in MAD measurements. The crystal lifetime is frequently increased by keeping the the crystal at a constant temperature close to 0°C. This can be obtained by commercial devices which provide a directed jet of cool gas which is coaxial with the glass capillary tube in which the sample is mounted. Another interesting possibility is shock-cooling of crystals at cryogenic temperatures, by which crystal degradation is in many cases virtually eliminated (Hope, 1988).

As discussed previously, it is important, prior to intensity measurements, to record XANES and EXAFS spectra from the sample crystal itself. A scintillation detector, mounted on one side of the diffractometer, measures fluorescence from the sample crystal as the x-ray energy is scanned across the absorption edge. The detector, positioned very close to the crystal, is mounted in the horizontal plane containing the beam and at 90° to the beam in order to decrease the intensity of the elastically scattered x-rays but not the fluorescence.

### XI.3.3.4. Diffraction Data Collection and Processing

The first step of the procedure is the determination of the variation of anomalous scattering factors as described previously. Fluorescence x-ray spectra in the near-edge region are reduced to f" values and the Kramers-Kronig transformation produces f' values. Both of these calculations are made subject to constraints to values obtained from quantum calculations at points relatively remote from the edge. In case of significant pleiochroism in the near-edge region, the fluorescence spectra are recorded for several orientations of the crystal with respect to the polarized incident beam and averaged values of f" and f' are calculated.

Then the choice of wavelengths is performed. Large values of f" and large values of differences $^{\lambda_i}f' - {}^{\lambda_j}f'$ are both required to get the best phasing power; hence, from eq. (XI.2) and (XI.3), both Bijvoet and dispersive ratios must be large.

In fact, Bijvoet and dispersive differences provide orthogonal phase information and are thus complementary; moreover, the strength of these diffferences depends in a predictable way on the magnitudes of anomalous scattering factors. The selection of wavelengths includes at least a pair of wavelengths very close to an absorption edge. One of these wavelengths corresponds in general to the largest value of f", and the other one to the inflection point in the rise of absorption at the edge which corresponds to the largest magnitude of f'. A third wavelength at a point remote from the edge (preferably on the high energy side, where f" is larger and the absorption lower) is added, in order to contrast the extreme value of f' that occurs at the inflection point with the smaller magnitude observed away from the edge.

Data collection can then proceed. From expected Bijvoet and dispersive ratios, counting times are set so that counting statistics will not be limiting. As usual, diffraction intensities must be processed to account for a number of factors including the Lorentz factor, polarization effects (Kahn et al., 1982), detector count loss, source intensity variation, absorption and radiation damage.

Through an appropriate experimental strategy, it is often possible to arrange that remaining common systematic errors will tend to be eliminated by differencing. Thus, one obtains greater precision in phase determination than the independent accuracy of measurement would warrant. Experimental control of systematic errors has several components:

i) All data, or at least all data pertaining to a given phase, should be taken from the same crystal, eliminating the intercrystal absorption and scaling errors that limit the accuracy of the isomorphous replacement method.

ii) The data for Bijvoet mates and for all wavelengths should be collected close together in time; this procedure minimizes both the impact of radiation damage and of slow drifts in the state of polarization of the beam at the sample location, in the x-ray optics and in the detector and beam monitor response.

iii) Crystals are mounted so as to exploit their symmetry and morphology to reduce absorption errors arising from different path lengths for the mates of a Bijvoet pair

iv) Absorption differences at different wavelengths can be taken into account in experimental transmission factors.

Many of the residual experimental errors in Bijvoet and dispersive differences can be further reduced numerically by parameterized local scaling of adjacent reflections as originally developed for highly precise, single-wavelength measurements (Hendrickson and Teeter, 1981). Afterwards, data from separate wavelengths are brought to a common scale; this is first done by bringing the various data sets into least-square agreement by the local scaling algorithm, then additional scale factors that account for variation in total scattering strength must also be applied. At each step, an appropriate rejection of outliers is imposed. Finally, all data are placed on a quasi-absolute scale by Wilson's statistics, sorted, and equivalent and redundant data are merged. It is emphasized that this merging occurs at a late stage, and may be further deferred until after phase determination for separate sets.

### XI.3.3.5. Applications

Although the possibility for phase determination from MAD data has been appreciated for decades, the realization of this promise has been quite slow in coming. Recently, however, the pace has quickened markedly. This reflects both the maturation of synchrotron instrumentation and also significant advances in methods of analysis as described in previous sections. The pioneering study by Hoppe and Jakubowski (1975), while determining phases for only a few hundred reflections, clearly demonstrated practical feasibility even with conventional x-ray sources. Another study with conventional x-rays, that on the small molecule selenolanthionine (Hendrickson, 1985), showed that accurate phases could be determined even using the continuum Bremsstrahlung from an x-ray tube. Another test study worth singling out was the analysis of lamprey hemoglobin, first reported at 5.5Å resolution (Hendrickson, 1984), in which many of the experimental and analytical procedures now in the use were first developed (Hendrickson et al., 1988).

Despite the usefulness of test demonstrations, it was only through complete analyses on macromolecules of unknown structure that the method could be proven. This has now been accomplished, as shown in table XI.3.

### XI.3.3.6. Prospects

After a long period of gestation, the MAD method can fairly be said to have emerged with vitality. To date applications exploiting K-shell edges have predominated. Many candidate problems including nearly all metalloproteins fall into this category. The MAD approach with K edges has also been successful with elements such as selenium and bromine that are not normally heavy enough for the MIR method. Biologically engineered selenomethionine proteins might serve as a general vehicle for protein structure determination (Hendrickson, 1985; Horton & Hendrickson, 1989). Similarly, brominations of nucleic-acid bases (U or C) offer a rather general approach for this class of problems. L-shell transitions lead to much stronger anomalous scattering, particularly at the white lines such as occur with lanthanides; thus MAD studies would be appealing on nearly any heavy-atom derivative that might be used for MIR phasing – but without a requirement for isomorphism. As instrumentation develops, experiments at very long wavelengths might be attractive (especially at S and P absorption edges, despite complexities due to the very high absorption coefficients). Using high energy storage rings and appropriate optics and detectors, very short wavelengths might also become more practical.

The MAD method is not without its complexities. The multiple data sets and the need for high precision in measurements in many MAD experiments are complications. Fortunately, there are advances in instrumentation, especially detectors, as previously discussed, and the availability and stability of synchrotron radiation for MAD experiments is also improving. Another potential pitfall concerns the effect of anisotropy, but studies indicate that, even when present, this need not be debilitating and can be accounted for (Fanchon and Hendrickson, 1989). In the case of selenomethionine proteins and certain other situations, the number of anomalous scatterer sites in a large macromolecule might present a daunting structural problem in its own right. However, with accurate $|^0F_A|$ values and the power of direct methods, one can

also hope to address this problem. In the end, the prospect that, for macromolecules as for small molecules, one might enjoy assurance of a straightforward structural determination once a crystal is grown is a powerful incentive for continued development of MAD phasing technology. It is not easy to predict the future of MAD with respect to other competing phasing methods, such as MIR, molecular replacement and, perhaps, direct methods. NMR may also provide (currently for proteins of less than about 20 kD) a model for molecular replacement. In fact scientists in structural biology are pragmatic and use all that is available and efficient to elucidate three dimensional structures. Several new synchrotron beam lines and instruments dedicated to MAD experiments are being built, and some of them are completed. These instruments will certainly be crucial for the development of the method.

## XI.4. Kinetic crystallography and fast data collection methods

The introduction of synchrotron radiation for structural studies by Rosenbaum & al. in 1971 brought the time resolution of X-ray techniques into the domain where biological action takes place. An intense beam is required with - especially polychromatic techniques - a very low divergence. In this respect, synchrotron sources are the best sources, even with respect to laser plasmas which produce a more intense but also more divergent burst of radiation.

A number of reports or reviews on the subject of time-resolved crystallography have appeared in recent years (e. g. Hajdu et al., 1988; Moffat, 1989; Moffat & Helliwell, 1989; Hajdu and Johnson, 1990; Pai, 1992). The proceedings of a meeting adressing these topics give a snapshot of the present status in the field (Cruickshank et al., 1992).

### XI.4.1. Monochromatic techniques

With monochromatic X-rays, only a small fraction of lattice planes diffract at any particular orientation of the crystal and the crystal has to be rotated in the beam in order to record progressively all integrated intensities. Using conventional sources, data rates of 50 to 1000 reflections/s have been achieved, and undulators from third generation high energy storage rings are brighter by several orders of magnitude. Considering only the x-ray sources, there is a potential to bring monochromatic techniques into the subsecond range. Let us discuss the various technical problems. The centrifugal acceleration produced by fast rotation is not a serious problem: at 1000 rev./s (then, 90° are swept in 15 ms), an average size protein crystal (0.5 mm in diameter) experiences a maximal acceleration of only 0.27g (Hajdu & Andersson, 1992). The real difficulty is the detector and the data collection method. A method which looks promising is based on the Weissenberg technique (Sakabe, 1991; Andersson et al., 1991). In this technique, as described previously, it is posssible to record on each image Bragg reflections excited through an angular range of several degrees with few overlaps and while keeping a reasonable signal to noise ratio on the detector. With an undulator and an even larger imaging plate, it might be possible, especially in the case of a crystal of high symmetry, to record a large fraction of the data on a single image with an exposure time limited essentially by the source brilliance.

Monochromatic techniques tolerate crystals with high mosaicity; images are relatively easy to process and may provide quality data with a good completeness both at low and high resolution .

### XI.4.2. White radiation technique. The Laue method.

Laue diffraction is discussed extensively in chapter XII by C. Wilkinson. Briefly summarized, Laue diffraction is produced when polychromatic x-rays illuminate a stationnary crystal. Reflections are integrated through a small wavelength range instead of a small angular range. A large number of lattice planes diffract simultaneously under these circumstances as the Bragg condition is satisfied for each of these planes by at least one wavelength of the spectrum. A short exposure time is the principal asset of the technique. In a quantitative analysis of Laue diffraction patterns recorded from the radiation emitted from a single bunch of electrons traversing an undulator Szebenyi et al. (1992) showed that data obtained in a 100 ps exposure are of useful quality. A few diffraction pictures taken at different orientations of the crystal can result in useful data sets. The exact number depends on the symmetry of the crystal; in the case of a cubic crystal, one single exposure can be sufficient. The advantage of Laue over monochromatic techniques is largely lost as soon as more than one exposure is needed to complete the data set.

The extraction of structure factor amplitudes from Laue images is in general more complicated than the processing of manochromatic data sets. There are are two main ways to extract this information. The first is based on a wavelength normalization curve to compensate for wavelength factors in the intensity measurements; this curve is derived from experimental data only, using intensities of equivalent reflections excited at various wavelengths (Helliwell et al., 1989). The second is based on a difference method, and can be used for the analysis of structural changes relative to a known starting structure.

The Laue technique suffers from two specific limitations, inherent to the physics of the method, which restrict its use in routine data collection ( Hajdu et al, 1991) and have implications to the use of this method in time-resolved measurements.

- Sensitivity to disorder in the crystal

The size and shape of a reflection on a Laue photograph depends on the dimensions of reciprocal points (crystal mosaicity) and on the divergence of the x-ray beam. Even moderate mosaicity (0.1-0.2°), makes reflections radially elongated, which can cause extensive overlapping between neighbouring relections. Mosaicity of most crystals increases during a structural transition or reaction, and therefore useful structural data may not always be attainable from reactive crystals with the Laue method.

- Lack of low resolution data

The two limiting spheres of radius $1/d_{max}$ and $1/d_{min}$ are in contact at the origin of the reciprocal lattice, so the efficiency of the Laue method at low resolution is hardly better than the efficiency of monochromatic still photographs. In addition, most of the reflections in this region are harmonic overlaps and those which are singlets are at the short wavelength limit of the spectrum where the scattering power is the lowest, and the change in spectral intensity is the steepest. Finally,

there is little or no reliable data in the range of about 4 - 5Å resolution to infinity. The consequence of the low resolution "hole" is that structural elements with a high B factor are difficult to identify from Laue data. The increase in motion in a structure causes a weakening of reflections at higher resolutions, so that the errors increase in parallel. Little information can be expected for structural motifs with high B factors from weak reflections at high resolution.

### XI.4.3. Starting a reaction in the crystal and the synchronization problem

Although there are still problems associated with the crystallographic part of time-resolved experiments, the major obstacles now seem to be chemical in nature, and connected to the fact that the image obtained from a diffraction experiment is the average over $10^{14}$ -$10^{15}$ molecules during the exposure time.

First, a simultaneous initiation of the reaction in the crystal is required. For most reactions in the crystalline state, temperature-jumps, pressure-jumps or Ph-jumps might be used to start the reaction (Pai, 1992). Very often, however, only photochemical activation is fast enough for efficient initial synchronization. Cage compounds are used for protecting the substrate against the enzyme, or the catalysis itself may be blocked through the covalent attachment of a reversible component to crucial active-site groups. Intense light pulses are needed to achieve fast conversion of caged compounds into substrates.

The kinetics of the catalyzed reaction in solution and in crystal must be investigated before starting time-resolved diffraction, and knowledge of the different rates of transformation of substrates into intermediates and finally into products should guide the design of the experiment. The course of the reaction during the diffraction experiment has also to be monitored, using for instance microspectrophotometer systems with time resolution in the millisecond range.

In conclusion, a combination of various experimental techniques - notably NMR and other spectroscopic techniques - with x-ray diffraction methods and computational procedures offers the obvious route for 4 dimensional (time being the 4th dimension, Andersson et al., 1992) structural studies in the future. Using cryotechniques, it should be possible to lengthen the time-intervals available for probing specific intermediates. Concerning diffraction methods, both monochromatic and polychromatic methods need consideration and further developments.

Acknowledgements: this chapter makes use of materials from various reviews and articles, in particular Fourme & Hendrickson (1990), Fourme et al. (1991), Hajdu & Andersson (1992) and other quoted references.

## General Readings

BLUNDELL,T.L. & JOHNSON L. N., 1976 - Protein crystallography - Academic Press (London)

HELLIWELL, J.R., 1992 - Macromolecular Crystallography with synchrotron radiation - Cambridge University Press (Cambridge)



STRYER, L., 1988, third edition - Biochemistry - Freeman (New York)

## References

ANDERSSON, I., CLIFTON, I.J., FULOP, V. & HADJU, J.,1991 - in Crystallographic Computing 5: From Chemistry to Biology; eds. MORAS, D. PODJARNY, A.D. & THIERRY, J.C. - Oxford University Press (Oxford)

ANDERSSON, I., CLIFTON, I.J., EDWARDS, S.L., FULOP, V., HADFIELD, A.T., NORDLUND, P., PHIZACKERLEY, R.P., SOLTIS, S.M., WAKATSUKI, S. & HADJU, J., 1992 -in Time Resolved Macromolecular Crystallography; eds.CRUICKSHANK et al. - Oxford University Press for the Royal Society

BLOW, D. M. & CRICK, F. H. C., 1959 - Acta Cryst. 12, 794

BRICOGNE, G., 1991 - in Isomorphous Replacement and Anomalous Scattering, Proceedings of the CCP4 Study Week End jan. 25-26 1991, p. 60 - Daresbury Laboratory

BRICOGNE, G., 1993 - Acta Cryst. D49, 37

CHAPUIS, G., TEMPLETON, D. H. & TEMPLETON, L. K., 1985 - Acta Cryst. A41, 274

CHIADMI, M., KAHN, R., FOURME, R. & DE LA FORTELLE, E., 1993 - J. Appl. Cryst. (in the press)

CROMER, D.T., & LIBERMAN, D., 1970 - J. Chem. Phys. 53, 1891

CRUICKSHANK, D.W.J., HELLIWELL, J.R. & JOHNSON, L.N., 1992 - Phil. Trans. R. Soc. London (A) 340

DE LA FORTELLE, E., BRICOGNE, G., KAHN, R. & FOURME, R., 1993 - abstract to the 16th International Congress of Crystallography, Beijing

DICKERSON, R. E., KENDREW, J. C. & STRANDBERG, B. E., 1961 - Acta Cryst. 14, 1188

DUMAS, C., 1988 - Doctoral Thesis, Université Paris-Sud, Orsay, France.

DUMAS, C., LASCU, I., MORERA, S., GLASER, P., FOURME, R., WALLET, V., LACOMBE, M.L., VERON, M. & JANIN, J., 1992 - The EMBO J. 11(9), 3203

FANCHON, E. & HENDRICKSON, W.A., 1989 Abstracts of the American Crystallographic Association Meeting, series 2, vol. 17, p.122.

FOURME, R., BAHRI, A., KAHN, R. & BOSSHARD, R., 1991 - Proc. of the European Workshop on X-ray detectors for synchrotron radiation sources (Aussois), ed. WALENTA, A.H. - EEC (Siegen )

FOURME, R. & HENDRICKSON, W.A. - 1990 - in Synchrotron Radiation and Biophysics, eds. S.S. HASNAIN, p. 156 - Hellis Horwood Limited (Chichester)

FOURME, R., DE LA FORTELLE, E., SHEPARD, W. & KAHN, R. ,1993, (submitted for publication)

GLUSKER, J.P. ed., 1993 - Acta Cryst. D 49 (1)

GUSS, J.M., MERRITT, E.A., PHIZACKERLEY, R.P., HEDMAN, B., MURATA, M., HODGSON, K.O. & FREEMAN, H.C., 1988 - Science 241, 806

HAJDU, J., ACHARYA, K.R., STUART, D.I. & JOHNSON, L.N.,1988 - Trends Biochem. Sci. 13, 104

HAJDU, J., ALMO, S.C., FARBER, G.K., PRATER, J.K., PETSKO, G.A., WAKATSUKI, S., CLIFTON, I.J. & FULOP, V., 1991 - in Crystallographic Computing 5: From Chemistry to Biology; eds. MORAS, D., PODJARNY, A.D. & THIERRY, J.C. - Oxford University Press (Oxford)

HAJDU J. & ANDERSSON I., 1992 - in Approches Expérimentales de la Dynamique des Macromolécules Biologiques, FOURME, R. & VACHETTE, P. ed., p 89, Cahiers IMABIO - CNRS (Paris).

HAJDU, J. & JOHNSON, L.N., 1990 - Biochemistry 29, 1668

HARADA, S., YASUI, M., MURAKAWA, K., KASAI, N. & SATOW, Y., 1986 - J. Appl. Cryst. 19, 448

HELLIWELL, J.R., HABASH, J., CRUICHSHANK, D.W.J., HARDING, M.M., GREENHOUGH, T.J., CAMPBELL, J.W., CLIFTON, I.J., ELDER, M., MACHIN, P.A., PAPIZ, M.Z. & ZUREK, S., 1989 - J. Appl. Cryst. 22, 483

HENDRICKSON, W. A., 1984 - Acta Cryst. A40, C3.

HENDRICKSON, W.A., 1985 - Trans. Am. Crystallogr. Assoc. 21,11

HENDRICKSON, W.A.,1991 - Science 254, 51

HENDRICKSON, W. A., & LATTMAN, E. E., 1970 - Acta Cryst. B26, 136

HENDRICKSON, W.A., PAHLER, A., SMITH, J.L., SATOW, Y., MERRITT, E.A. & PHIZACKERLEY, R.P., 1989 - Proc. Natl. Acad. Sci. USA 86, 2190

HENDRICKSON, W. A., SMITH, J. L., PHIZACKERLEY, R. P. & MERRITT, E. A.,1988 - Proteins 4, 77

HENDRICKSON, W.A. & TEETER, M.M., 1981 - Nature 290, 107

HOPE, H., 1988 - Acta Cryst. B44, 22

HOPPE, W., JAKUBOWSKI, V., 1975 - in Anomalous Scattering, ed. RAMASESHAN, S. & ABRAHAMS, S. C., p. 437 - Munksgaard (Copenhagen)

HORTON, J.R. & HENDRICKSON, W.A., 1989 - Abstracts of the American Crystallographic Association Meeting, series 2, vol. 17, p.122

JAMES, R.J.,1965 - The Optical Principles of the Diffraction of X-rays - Cornell University Press (Ithaca)

KAHN, R., FOURME, R., BOSSHARD, R., CHIADMI, M., RISLER, J. L., DIDEBERG, O. & WERY, J. P., 1985 - FEBS Lett. 179, 133

KAHN, R., FOURME, R., BOSSHARD, R. & SAINTAGNE, V., 1986) - Nucl. Instrum. and Meth. A246, 596

KAHN, R., FOURME, R., GADET, A., JANIN, J., DUMAS, C. & ANDRÉ, D., 1982 - J. Appl. Crystallogr. 15, 330

KARLE, J., 1980 - Int. J. Quant. Chem. 7, 357

KORSZUN, Z. R., 1987 - J. Mol. Biol. 196, 413

MIYAHARA, J., TAKAHASHI K., AMEMIYA,Y., KAMIYA, N. & SATOW, Y.,1986 - Nucl. Instrum. and Meth. A246, 572

MOFFAT, K., 1989 - Annu. Rev. Biophys. Biophys. Chem. 18,309

MOFFAT, K. & HELLIWELL, J.R., 1989 - Top Curr Chem, 151, 61



MOY, J.P. & GIBNEY, S., 1992 - Low Energy X-ray Image Intensifier Development, Phase 1 report - ESRF (Grenoble)

OGATA, C.M., HENDRICKSON, W.A., GAO, X. & PATEL, D.J., 1989 - Abstracts of the American Crystallographic Association Meeting, series 2, vol. 17, p. 53

OKAYA, Y. & PEPINSKY, R., 1956 - Phys. Review 103, 1645

PAI, E.F., 1992 - Current Opinion in Structural Biology 2, 621

PÄHLER, A., SMITH, J. L. & HENDRICKSON, W. A.,1990 - Acta Cryst. A46, 537

PHILLIPS, J. C., & HODGSON, K.O.1980 - Acta Cryst. A36, 856

PHILLIPS, J.C., TEMPLETON, D.H., TEMPLETON, L.K. & HODGSON, K.O.,1978 -Science 201, 257

PHIZACKERLEY, R. P., CORK, C. W., MERRITT, E. A.,1986 - Nucl. Instrum. Meth. A246, 579

ROSENBAUM, G., HOLMES, K.C. & WITZ, J., 1971 - Nature 230, 434

ROSSMANN, M. G.,1961 - Acta Cryst. 14, 383

SAKABE, N., 1991 - Nucl. Instrum. and Meth. A303, 448

SMITH, J.L., 1991 - Current Opinion in Structural Biology 1,1002

SMITH, J.L. & WATENPAUGH, K. ed., 1991 - Structural biology and synchrotron radiation: assessment of resources and needs - Purdue Univ., USA.

SZEBENYI, D.M.E., BILDERBACK, D.H., LEGRAND, A., MOFFAT, K., SCHIELDKAMP, W., SMITH-TEMPLE, B. & TENG, T.-Y., 1992; J. Appl. Cryst. 25, 414

TEMPLETON, D.H. & TEMPLETON, L.K., 1982 - Acta Cryst. A38, 62

TEMPLETON, D.H. & TEMPLETON, L.K.,1985 - Acta Cryst. A41, 365

TEMPLETON, L. K. & TEMPLETON, D. H., 1988 - Acta Cryst. A 44, 1045

WALENTA, A.H. ed., 1991 - Proc. of the European Workshop on X-ray detectors for synchrotron radiation sources (Aussois) - EEC (Siegen, Germany)

WEIS, W.I., KAHN, R., FOURME, R., DRICKAMER, K. & HENDRICKSON, W.A. 1991 - Science 254, 1608

WESTBROOK, E.M., DEACON, M.L., STRAUSS, M.G., NADAY, I. & SWEET, R.M. (1989). Abstracts of the American Crystallographic Association Meeting, series 2, vol. 17.

# CHAPTER XII

## X-RAY AND NEUTRON LAUE DIFFRACTION

J.R. HELLIWELL AND C. WILKINSON

## XII.1. Introduction

As indicated by McIntyre in Volume I VII.2., the original X-ray Laue diffraction experiment was based on an idea of von Laue and conducted by Friedrich and Knipping (Friedrich et al. 1912) and earned von Laue the Nobel Prize for physics in 1914. The original diffraction photograph was from a crystal of copper sulphate.

The essential feature of the Laue method, as it became called, is that the incident X-ray beam is polychromatic (a 'white beam') and the crystal sample is held stationary. X-rays of all wavelengths from the emission tube are allowed to impinge onto the sample; no special filtering or monochromatisation is employed. The Bremsstrahlung continuum and the characteristic emission lines constitute this incident beam of X-rays. This beam hits the stationary crystal and each Bragg reflection making up the diffraction pattern is excited simultaneously, but by a different wavelength. A given set of 'reflecting planes' in the crystal selects from the beam the particular wavelength which allows constructive interference to occur. This is in contrast to the monochromatic rotating crystal method, in which each reflection is stimulated in turn by varying the angle of incidence on the specimen crystal of an X-ray beam of a single (normally characteristic) wavelength. The Laue method is described in the book by Amorós, Buerger and Amorós (1975).

The first analyses of simple crystal structures were made using Laue photographs by W.L. Bragg, who deduced the structure of sodium chloride and other alkali halide crystals (for a historical review see Bragg (1975)). Subsequently, Bragg primarily used the monochromatic X-ray beam to examine crystals in the spectrometer designed and built by his father W.H. Bragg. Enthusiastic proponents of the use of the Laue method were Wyckoff (1924) and Pauling. However, the Laue method at that time was subject to various real and imagined limitations (discussed below) and its use lapsed as a method for determining molecular structure as it became superseded by the monochromatic rotating crystal method. This was in large part due to the relative weakness of the Bremsstrahlung radiation with respect to the characteristic lines from an X-ray tube.

The spectral curve of synchrotron radiation, however, ideally lends itself to Laue geometry since a broad band of wavelengths of high intensity is emitted by the synchrotron electron beam (Helliwell (1992)). As a result, a very large number of reflections can be recorded in a remarkably short exposure time in a Laue experiment; this has led to a revival of the Laue method as a means for quantitative structure analysis, especially for kinetic studies and the analysis of structural perturbations. Time resolved investigations include the study of enzyme or zeolite electric fields, pressure and temperature on various materials. An example of a

# III Scattering by Chain Molecules

Basic reference : B.K. Vainshtein, Elsevier (1966)
"Diffraction of X-rays by Chain Molecules"

## 1- Overview

- found for proteins, nucleic acids and sugars
- natural but imperfect crystallization
  ⇒ atomic resolution is difficult to obtain
- assemblies of parallel fibers
  - generally longitudinal periodicity
  - lateral order more or less well defined
- either isolated form or in biological tissues
- in biological tissues :
  - Composite materials
  - may be heterogeneous
  - mechanical role (except for DNA)
- order from the atomic level up to the macroscopic one.

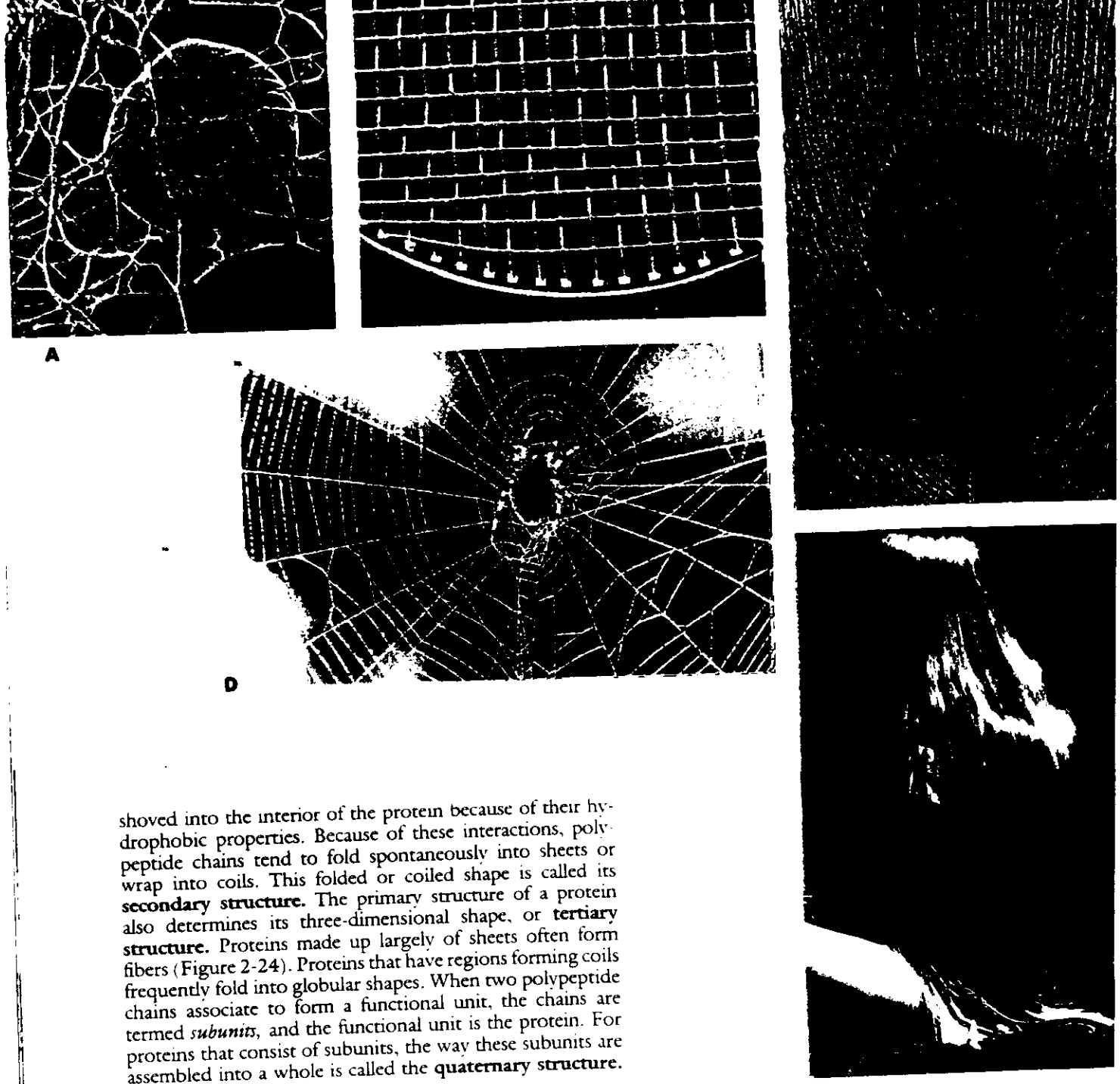


shoved into the interior of the protein because of their hydrophobic properties. Because of these interactions, polypeptide chains tend to fold spontaneously into sheets or wrap into coils. This folded or coiled shape is called its **secondary structure.** The primary structure of a protein also determines its three-dimensional shape, or **tertiary structure.** Proteins made up largely of sheets often form fibers (Figure 2-24). Proteins that have regions forming coils frequently fold into globular shapes. When two polypeptide chains associate to form a functional unit, the chains are termed *subunits*, and the functional unit is the protein. For proteins that consist of subunits, the way these subunits are assembled into a whole is called the **quaternary structure.**

**Approximately 20 different amino acids are used in various sequences and combinations to make up a wide variety of proteins. These amino acids have different properties from one another. These differences and the sequence in which the amino acids are arranged determine the shape of a protein, which is crucial to its proper functioning.**

**FIGURE 2-24 Many proteins play stru roles.**
**A** Fibrin—electron micrograph of a t clot.
**B** Collagen—strings of a tennis rac
**C** Keratin—a peacock feather
**D** Silk—a spider's web.
**E** Hair—a woman's hair.

# Principles of Scattering by Chain Molecules

## Isolated Chain $|F|^2_{obj}$ ?

- Continuous Chain

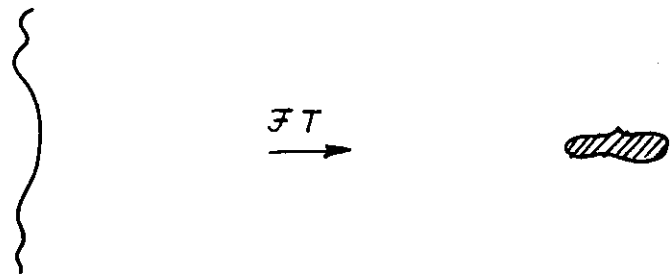


- Discontinuous Chain

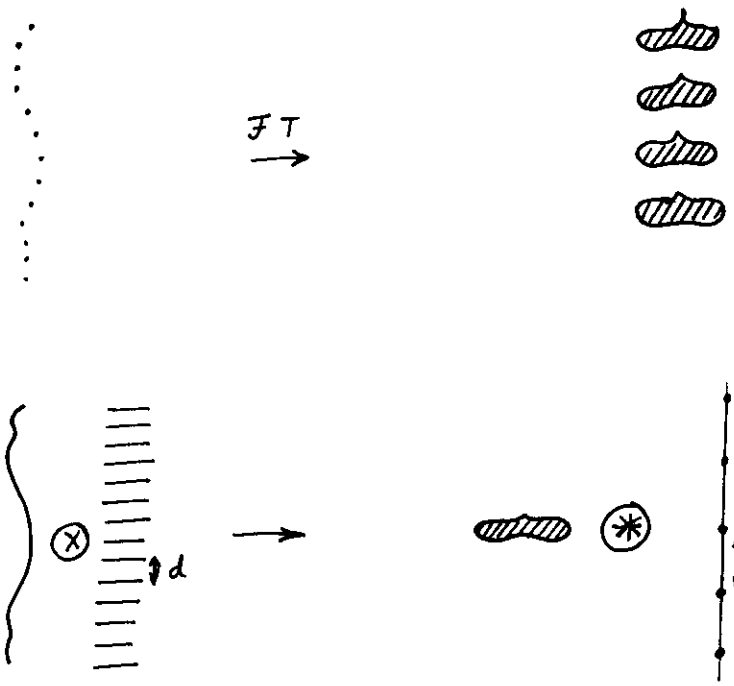

- Periodic Chain

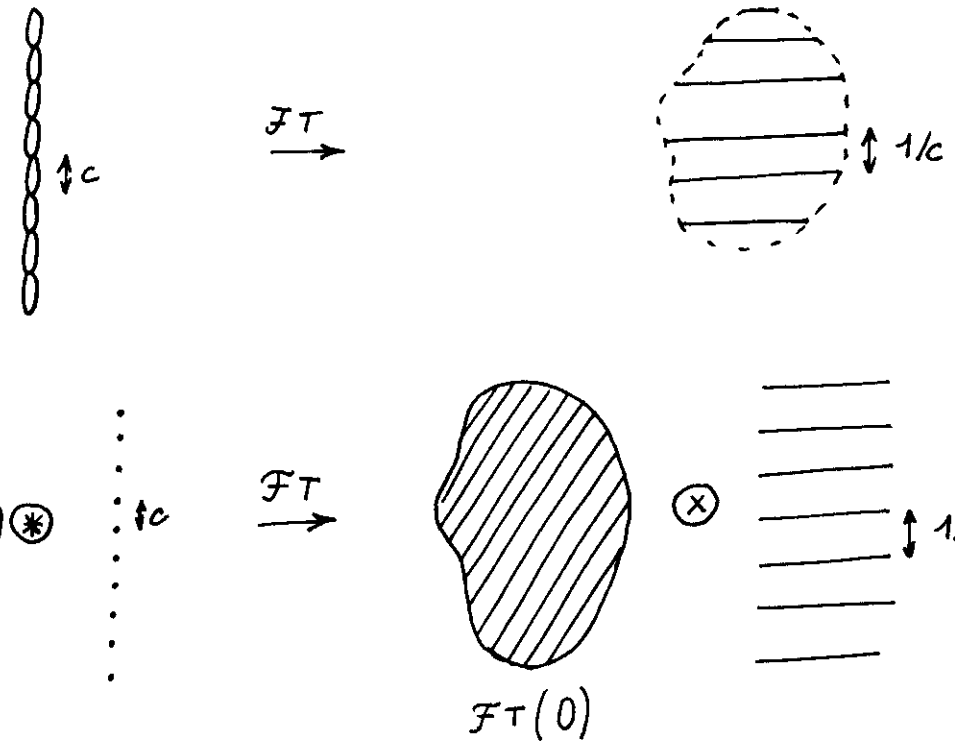


- Periodic discontinuous Chain

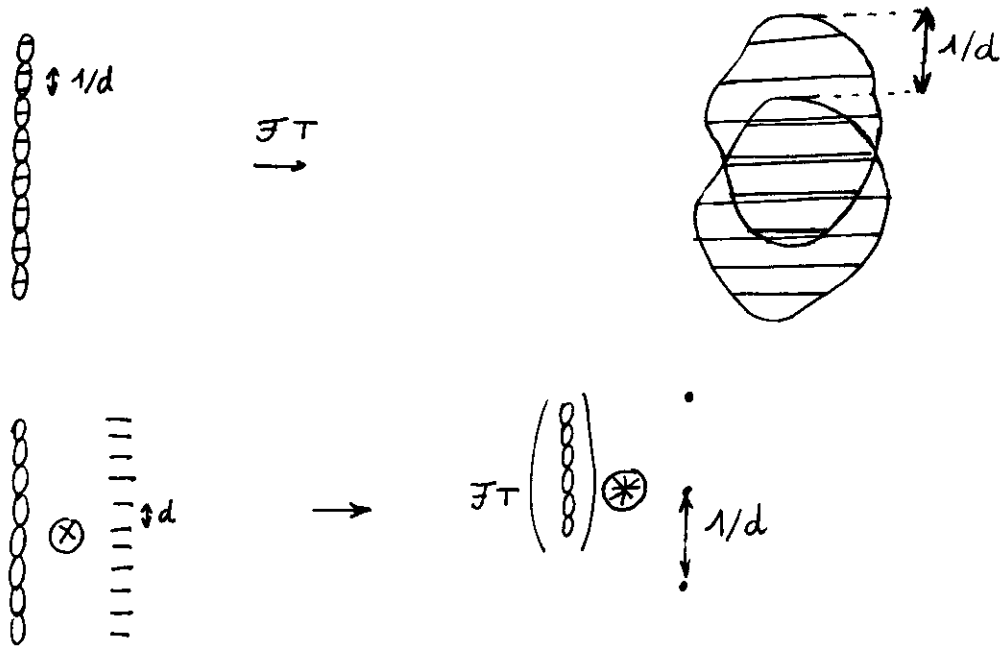

- Cylinders

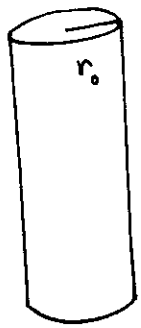


full cylinder
$(r_0, \rho_0)$

$$|F_{obj}|^2 = \left(2\pi \rho_0 r_0^2 \frac{J_1(u_0)}{u_0}\right)^2$$

With $u_0 = 2\pi r_0 S$

limited to the equatorial plane

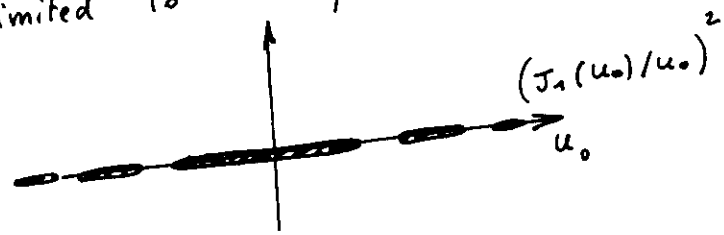


- Helix


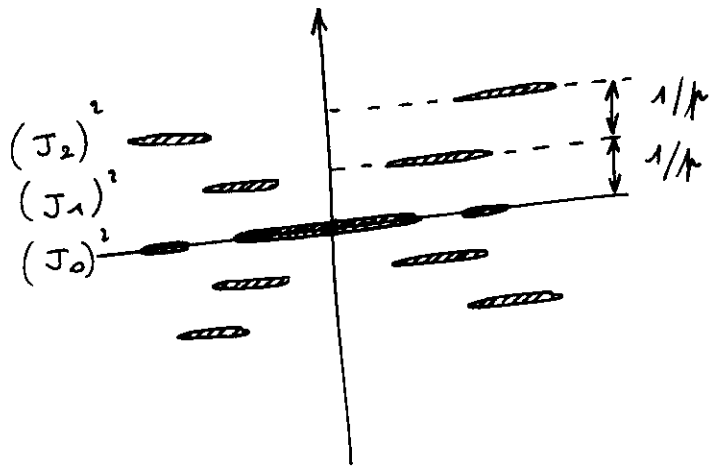


cross pattern

# 2-d array of chains

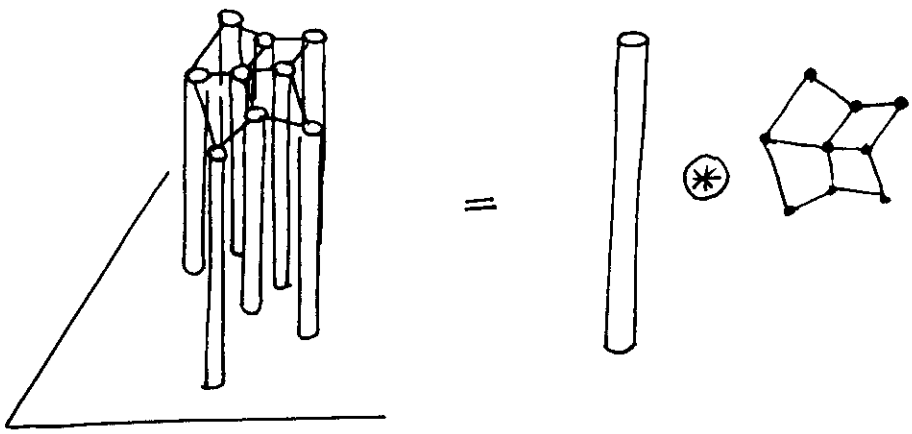

$$|FT(Obj)|^2 \otimes FT(z(\vec{r}))$$

$$|F_{obj}|^2 \otimes Z(S)$$

↑ limited to the equatorial plane.

① cryptalline order

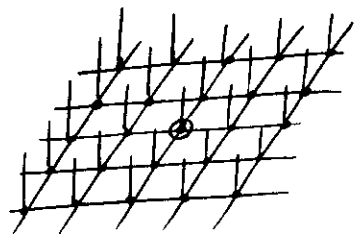

② liquid order

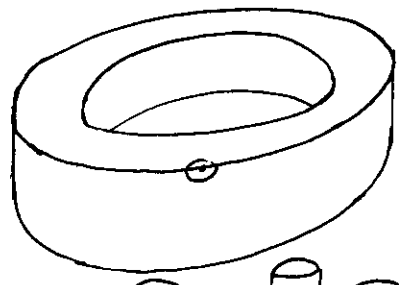

③ disordered system

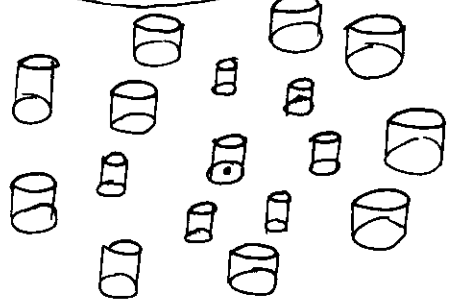

# 3-d array of chains

longitudinal ordering between neighbouring chains

$\Rightarrow$ periodicity along the chains

$\Rightarrow$ $Z(S)$ becomes structured along $\vec{c}^*$

# CHAPTER XI

## FIBRE DIFFRACTION

V.T. FORSYTH

The fibrous state is a natural one for polymer molecules which tend to assume regular helical conformations rather than the globular structures characteristic of many proteins. Fibre diffraction therefore has broad application to the study of a wide range of biological and synthetic polymers. It is the purpose of this chapter to illustrate the general scope of the method and in particular to demonstrate the impact of modern synchrotron X-ray and neutron beam sources on the range of applications available to the method.

An aligned fibre is characterised as containing many regions in which the polymer molecules are arranged with their long axes parallel to the fibre axis. These are typically separated by less ordered amorphous regions. The molecular alignment within such a fibre is associated with varying degrees of order in the side-by-side packing of the chains (for a detailed description of the types of disorder in fibrous samples, see references 1 and 2). To a large extent this ordering will determine the general appearance of the observed diffraction pattern which may vary from continuous molecular transform to the other extreme where the pattern is dominated by sharp Bragg reflections. Because there is no preferred orientation of microcrystallites about the fibre axis, an X-ray fibre diffraction pattern from a crystalline fibre has some of the character of that which would be obtained from a single crystal if it was rotated by 360° about one of its principal axes during data collection. The resolution attained in fibre diffraction experiments varies widely but can in favourable circumstances extend to d spacings of ~2Å. Whilst there is some loss of information imposed by cylindrical averaging in fibre diffraction this has to be offset against the fact that in most situations comparable measurements are not possible from single crystal systems. In many biological structures such as muscle and connective tissue and also in synthetic industrial polymers, the fibrous state is functionally important and fibre diffraction provides the most powerful technique to establish both molecular structure and the higher order interactions of these molecules. It is also true to say that fibre diffraction offers one of the few quantitative methods which are well suited to the study of conformational pathways in polymer molecules. Such investigations are of central importance in the study of DNA polymorphism (where highly cooperative structural transitions are observed) and also of synthetic polymers where particular drawing and annealing methods are of direct relevance to industrial processes.

Because of the importance of helical systems in fibre diffraction, the first part of this chapter is used to summarise some important results from helical diffraction theory, starting with the Fourier transforms of smooth and discontinuous helices and ending with the structure factors expected from a fully crystalline array of helical molecules. This is followed by two sections which are designed to illustrate the scope of fibre diffraction as applied to a few specific examples. These include a number of DNA systems and also the industrial

thermoplastic and has many industrial applications. In discussing the use of synchrotron X-ray sources in fibre diffraction the description has been limited to time-resolved studies and does not consider the application of other important techniques such as anomalous scattering. The same is true for the examples which illustrate the application of neutron fibre diffraction. These are focussed exclusively on isotopic substitution experiments aimed at locating for example water around DNA or hydrogen atoms in PEEK. It is hoped that by presenting some selected results from fibre diffraction it will be possible to illustrate not only the applicability of these methods to a wide variety of polymer systems but also to emphasise the importance of the complementarity which exists between X-ray and neutron fibre diffraction methods.

## XI.1. Helical Diffraction Theory

### XI.1.1. The Fourier Transform of an Infinite Smooth Helix

An infinite smooth helix (H) (see figure XI.1) of radius r, pitch P and of uniform scattering density can be thought of as the convolution of a single turn of the helix (T) with a point lattice (L) of spacing P along the direction of the helix axis. By the convolution theorem it is therefore possible to evaluate the Fourier transform of H as the product of the Fourier transforms of T and L so that $F_H=F_TF_L$.

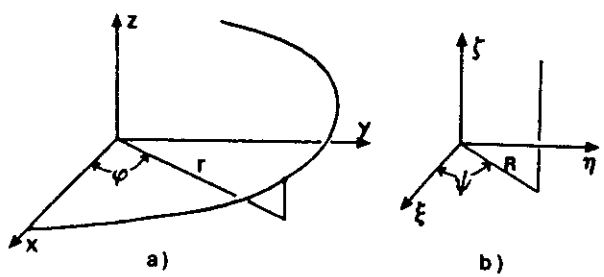


Figure XI.1. — (a) Cartesian and cylindrical polar coordinates for a point on a helix.
(b) Corresponding coordinates for a point in reciprocal space[3].

It can be shown that $F_T$ is given by:

$$F_T(R,\psi,\zeta)=\int_0^P \exp\left[2\pi iRr\cos\left(\frac{2\pi z}{P}-\psi\right)\right]\exp(2\pi i\,\zeta z)\,dz.$$

However since the Fourier transform $F_L$ is a function which is zero everywhere except on a series of planes having a spacing 1/P, we only need to evaluate $F_T$ for $\zeta=n/P$ where n is any integer. The integral given above may be evaluated using the identity :



$$\int_0^{2\pi}\exp(iX\cos\theta)\exp(in\theta)d\theta=2\pi i^nJ_n(X)$$

where $J_n(X)$ is an $n^{th}$ order Bessel function of argument X. It then follows that

$$F_H\left(R,\psi,\frac{n}{P}\right)=J_n(2\pi Rr)\exp\left[in\left(\psi+\frac{\pi}{2}\right)\right]$$

neglecting constant terms. The magnitude of this transform is independent of ψ and the intensity transform will vary as the function $J_n(2\pi Rr)$ as shown in figure XI.2. The distribution of Bessel functions across these layer lines gives a characteristic cross-like appearance since as n increases the first maximum of $J_n(2\pi Rr)$ occurs at progressively larger R and has gradually diminishing magnitude.

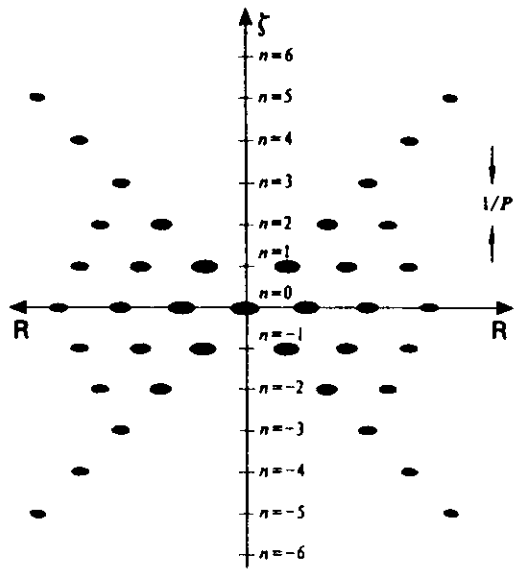


Figure XI.2 — The diffraction pattern expected from an infinite continuous helix[4]

### XI.1.2. The Fourier Transform of an Infinite Discontinuous Helix

It is relatively simple to extend this analysis to an infinite *discontinuous* helix (D) in which there are regularly spaced points along the structure, as illustrated in figure XI.3.

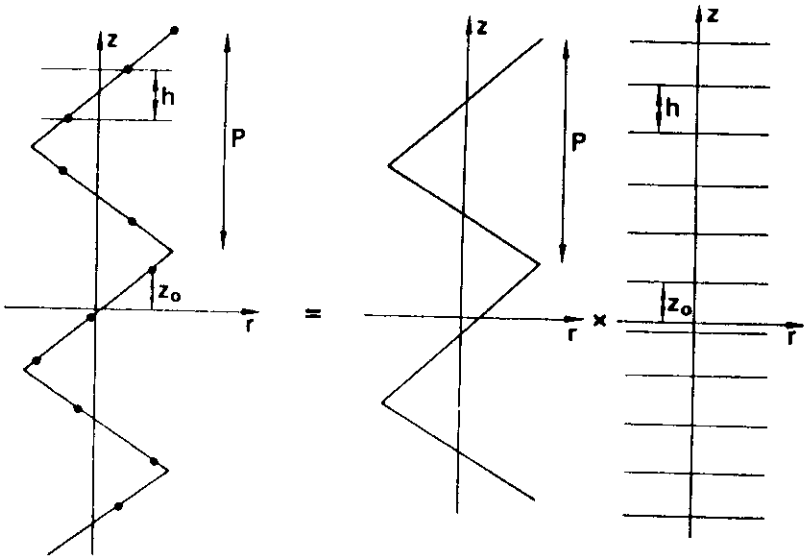


Figure XI.3 — a discontinuous helix made up of regularly separated points along the path of a smooth helix (from reference 4)

The discontinuous helix is visualised as the product of the function which describes an infinite continuous helix (i.e. H) with one which is zero everywhere except on horizontal planes having a spacing h. Hence the Fourier transform of the discontinuous helix ($F_D$) is the convolution of the Fourier transform of the infinite continuous helix with that of the set of planes spaced by h. The latter transform has peaks with spacing 1/h along ζ so that the form of $F_D$ is essentially the same as that for a simple helix but for the fact that the helix cross pattern of figure XI.2 is repeated for all points given by ζ=m/h, where m is an integer (see figure XI.4).

Therefore we would expect in a diffraction experiment to observe diffraction only on planes defined by:

$$\zeta = \frac{n}{P} + \frac{m}{h}.$$

In the general case where the helix is non-integral having N "points" per K turns then the true repeat along the axis of the helix is Nh=KP=c. Hence it can be shown that:

$$n = \frac{l - mN}{K}.$$

This is the *helical selection rule* for selecting Bessel function orders that will contribute to a given layer line l. The Fourier transform of the discontinuous helix ($F_D$) is thus summed over all values of the Bessel function orders allowed by the selection rule so that



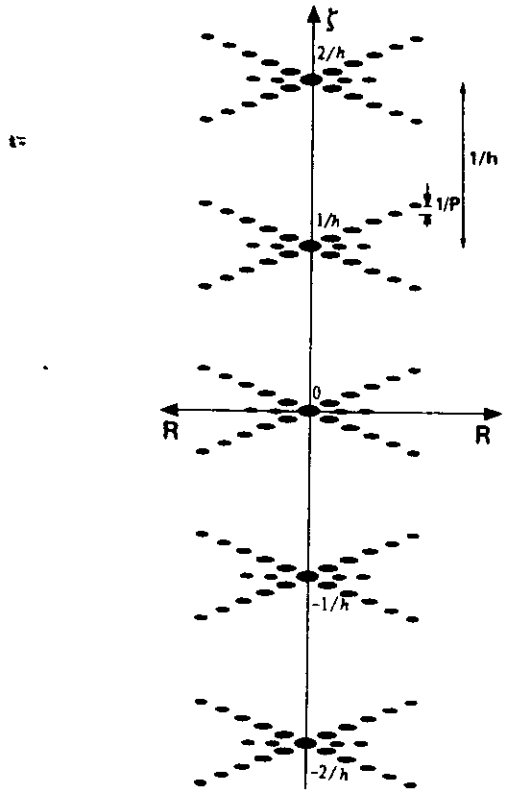


Figure XI.4 —The Fourier transform of a discontinuous helix (from reference 4)

$$F_D\left(R, \psi, \frac{\ell}{c}\right) = \sum_n J_n(2\pi Rr) \exp\left[in\left(\psi + \frac{\pi}{2}\right)\right]$$

### XI.1.3. The Fourier Transform of a Helix containing Polyatomic Monomers

If we now substitute a monomer unit for each of these points on our discontinuous helix then we can predict the features that we would expect to see in a diffraction experiment with a real helical polymer. The Fourier transform of such a system is obtained by the vector addition of the scattering contributions from each of the j constituent atoms making up the monomer. Each of these atoms can be described by cylindrical polar coordinates $(r_j, \phi_j, z_j)$ so that the Fourier transform for layer line *l* is given by:

$$F(h,k,l) = \sum_j \sum_n f_j J_n\left(2\pi R r_j\right) \exp i\left[n\left(\psi - \phi_j + \frac{\pi}{2}\right) + \frac{2\pi l z_j}{c}\right].$$

where $f_j$ is the atomic scattering factor of the jth atom. The principal features of the transforms described in the previous sections are well illustrated by the semicrystalline diffraction pattern recorded from the B form of the DNA double helix (figure XI.5(a)). The spacing of the layer lines in this pattern reflects the ~34Å pitch of the helix and the cross shaped intensity distribution is evident. The strong meridional reflection on the 10th layer line corresponds to a rise/base-pair residue of 3.4Å in the ten-fold helix.

### XI.1.4. Structure Factors Calculated From a Crystalline Array of Helices

Now consider a regular 3-dimensional array of helices so that each unit cell has p molecules with the fractional coordinates $(x_k,y_k,z_k)$ and molecular orientation $\phi_k$. The structure factor F(h,k,l) is given by

$$F(h,k,l)=\sum_k\sum_n\sum_j f_j J_n\left(2\pi R r_j\right)\exp i\left[n\left(\psi-\phi_j+\frac{\pi}{2}\right)+\frac{2\pi l z_j}{c}\right]\exp 2\pi i\left(hx_k+ky_k+lz_k\right)\exp(-$$

For a fully crystalline array of helices it is clear then that the sampling of the underlying molecular transform at reciprocal lattice points will result in a rather different diffraction pattern from the screw-disordered pattern shown in Figure XI.5(a). Figure XI.5(b) shows a crystalline diffraction pattern recorded from B-DNA with sharp Bragg reflections extending to high resolution. As mentioned earlier the random orientation of the crystallites about the fibre axis results in some overlap of systematically related reflections so that the appearance of the diffraction pattern is rather like that of a single crystal rotation photograph in which the reflections have been broadened into arcs.

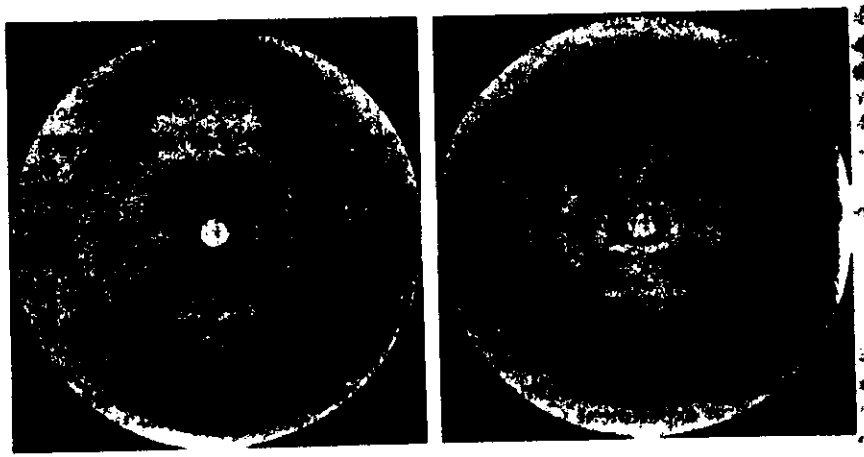

(a) (b)

Figure XI.5 — (a) Semicrystalline X-ray fibre diffraction pattern collected from semi-crystalline B-DNA. (b) Crystalline fibre diffaction pattern collected from the lithium salt of B-DNA.



## XI.2. X-ray Fibre Diffraction Studies using Synchrotron Radiation

The availability of synchrotron X-ray sources has dramatically extended the range of diffraction studies which can be undertaken for biological and synthetic systems. The high X-ray fluxes available on synchrotron radiation sources can be exploited in a number of ways so that in addition to the ability to undertake time-resolved diffraction studies of conformational changes in a wide variety of systems, it is also possible to collect diffraction data from very small samples or samples that are particularly susceptible to radiation damage. The wavelength tunability of synchrotron radiation sources has also been exploited in the study of single crystal and fibrous systems. In fibre diffraction studies it is possible to record diffraction patterns with exposures that are between two and three orders of magnitude shorter than those obtainable on conventional equipment. The implications of this in the field of DNA studies is evident in that it is possible to study conformational transitions in the double helix as its structure varies in response to changes in the water or ionic content of the sample. A typical fibre is ~200μm thick and ~5mm long. On conventional X-ray equipment this frequently necessitates exposure times of up to 12 hours. The use of the SERC Daresbury Laboratory synchrotron radiation source (SRS) in comparable experiments on line 7.2 results in exposure times of ~5 minutes. Similar experiments on the Wiggler line 9.6 with the Enraf-Nonius FAST TV detector allow exposure times of ~5 seconds. Although the use of an electronic area detector inevitably results in some loss of spatial resolution in the diffraction image it can be seen from figure XI.6 that it is still possible to collect high resolution data of a quality that is adequate for time-resolved studies.

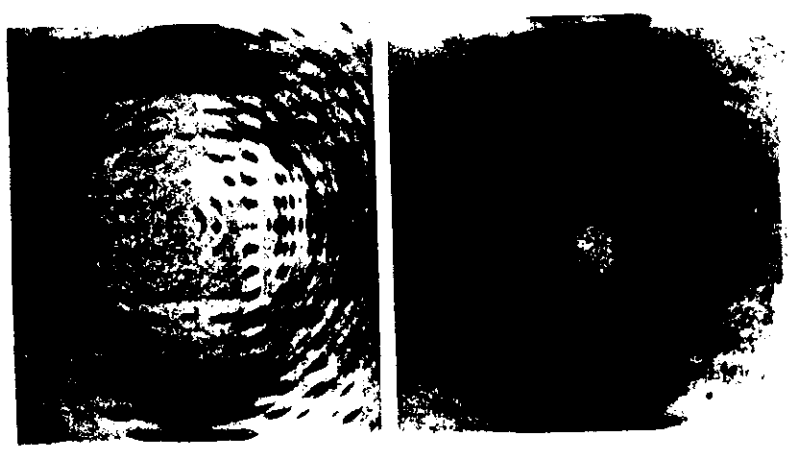

(a) (b)

Figure XI.6 — Comparison of X-ray fibre diffraction patterns recorded from the potassium salt of the D form of poly[d(A-T)].poly[d(A-T)] using (a) photographic film and (b) the Enraf-Nonius FAST TV detector.

One example of the way in which this sort of time resolution can be used in investigating conformational changes is provided by X-ray fibre diffraction studies of the B⇔D structural transition in DNA[5]. This is a transition which was first characterised using film on line 7.2 and later improved in studies using the FAST on line 9.6. Some of these results are shown in figure XI.7 which shows 6 selected diffraction patterns recorded during a time-resolved sequence. From these diffraction patterns it is can be seen that the reflection labelled II at the beginning of the sequence splits to form an extra reflection IV which moves continuously towards the centre of the pattern during the transition to the B form. These datasets show that the D⇔B structural change is a highly cooperative one which occurs via a series of intermediate conformations such that the pitch of the DNA double helix changes smoothly between the 24.2 Å characteristic of D-DNA to the 33.6Å characteristic of B-DNA in this polymer (see figure XI.8). Other experiments of this type have been undertaken for the A⇔B, A⇔S and S⇔B conformational transitions. Of particular interest are transitions involving the S(or Z) form because these involve a change of handedness of the helix[6].

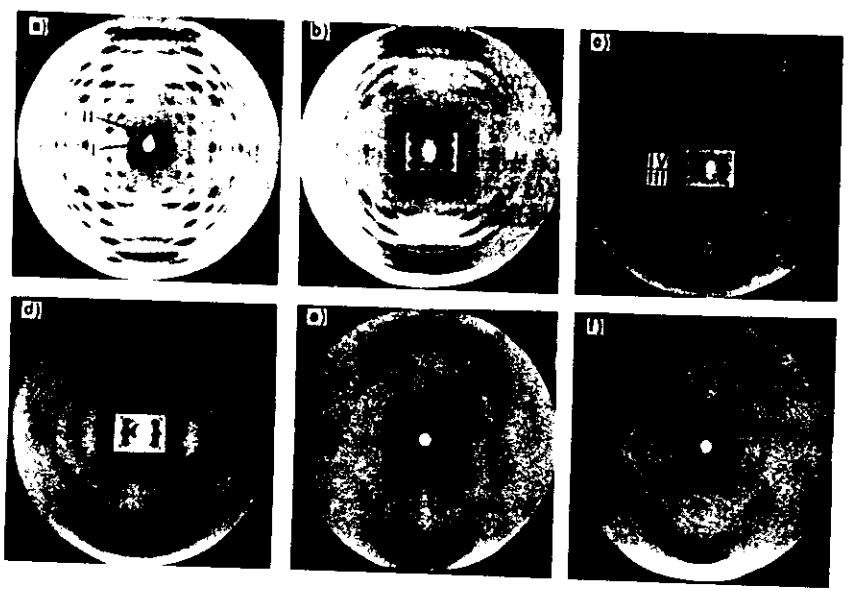


Figure XI.7. — Selected diffraction frames recorded during the D⇔B transition in the DNA polymer poly[d(A-T)].poly[d(A-T).

Results from time-resolved fibre diffraction studies of industrial polymers have also produced extremely interesting results that have provided new information on the drawing and annealing stages in the production of polymer sheets. In time resolved studies of PEEK undertaken on line 9.6 with the FAST detector both these processes have been studied in detail.

Figure XI.9 shows a sequence of selected diffraction patterns illustrating one such experiment where a "cold-draw" process of the polymer is followed by an annealing stage. The sequence of diffraction patterns proceeds from top left→top right→middle left→middle right etc. and starts with a pattern collected from the polymer which has been oriented during a cold draw. One of the most striking observations in this experiment was that the onset of crystallisation (seen in the last two pictures) in a drawn sheet of polymer was preceeded by a sudden and temporary loss of orientation in the pattern[7]. This was a result which had not previously been observed using film at the SRS and was first observed when experiments using the FAST were initiated.

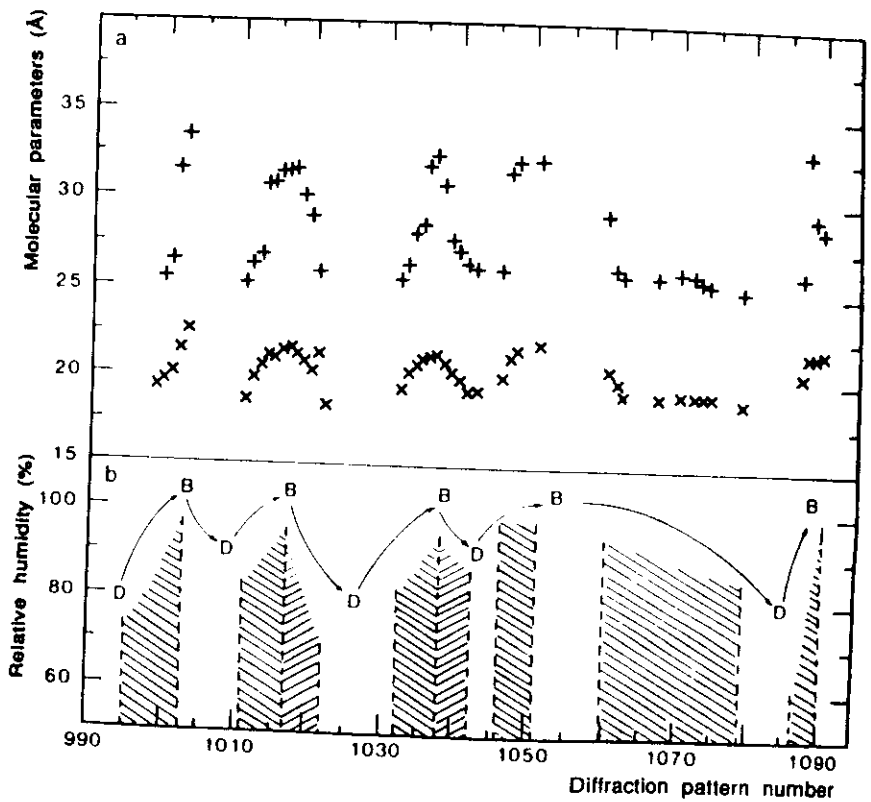


Figure XI.8 . — Variation of the helix pitch (x) and lateral intermolecular spacing (+) determined from the diffraction patterns recorded during the D⇔B conformational transition in the poly[d(A-T)].poly[d(A-T)] double helix (from reference 5).

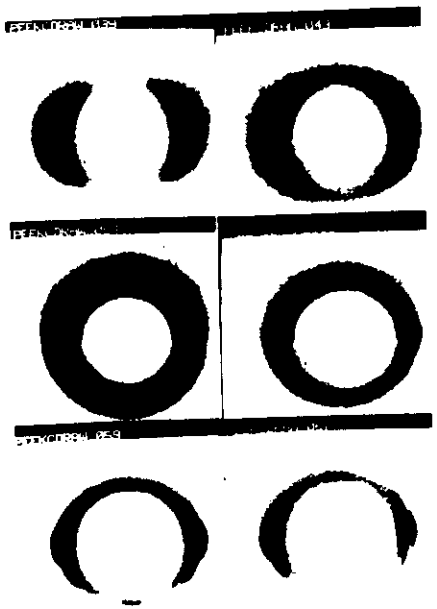

Figure XI.9. — Fibre diffraction patterns collected from PEEK during the drawing and annealing processes.

## XI.3. Neutron High-Angle Fibre Diffraction

Although X-ray fibre diffraction experiments with synchrotron radiation provide very extensive information on molecular conformation and on structural transitions there are instances in which neutron fibre diffraction measurements offer important advantages. This stems largely from the fact that the neutron scattering factors of the various elements vary across the periodic table in a way that is completely different than that for X-rays. In particular the large difference in the scattering powers of hydrogen and its isotope deuterium enables a variety of isotopic replacement experiments to be used in studies of the location of hydrogen (a very weak scatterer of X-rays) atoms in molecular structures. The ability to undertake isotopic substitution of $D_2O$ for $H_2O$ is widely exploited in a variety of neutron scattering techniques but has only recently been applied in high-angle neutron fibre diffraction studies where it has provided important information on the location of ordered water around the DNA double helix. This is an area of central interest in molecular biology where it is clear that water plays a vital role in stabilising the various conformations that DNA can adopt and in mediating structural transitions between these conformations. Despite the fact that fibre diffraction offers the most direct method of investigating the structure of DNA polymers, results from X-ray studies have provided only limited information in this area. The first application of neutron high-angle fibre diffraction to the study of DNA hydration was undertaken on the D form of the poly[d(A-T)].poly[d(A-T)] double helix[8].

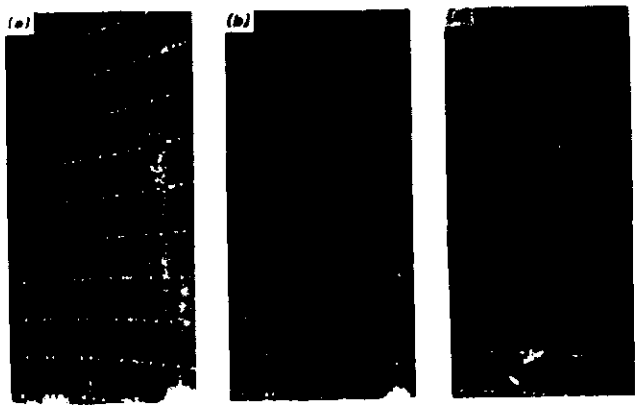


Figure XI.10. — Neutron high-angle diffraction data recorded from D-DNA (a) hydrated with $D_2O$; (b) hydrated with $H_2O$; (c) point for point difference between images (a) and (b). The white dots on these pictures indicate the positions of reciprocal lattice points.

Figure XI.10 shows part of the neutron high-angle fibre diffraction data collected from (a) D-DNA hydrated with $D_2O$; (b) D-DNA hydrated by $H_2O$ and (c) the point for point difference between the two patterns in (a) and (b). There are clear, reversible and reproducible differences between the diffraction patterns collected for DNA/$D_2O$ and the DNA/$H_2O$. Difference amplitudes measured from these datasets have been used in the construction of Fourier difference maps in which peaks were identified with ordered water around the DNA. Figure XI.11 shows one view of a $D_2O$-$H_2O$ difference map calculated for D-DNA.

Figure XI.11. — $D_2O$-$H_2O$ Fourier difference map showing the distribution of water around the D form of DNA

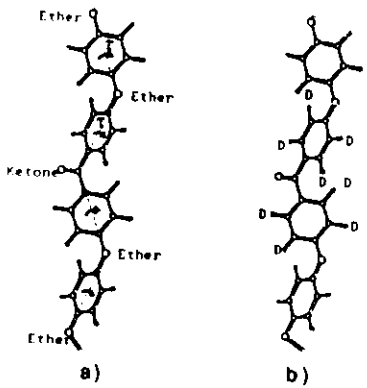


Figure XI.12. — The structure of PEEK: (a) the normal hydrogenated polymer and (b) the deuterated polymer in which 2 out of every 3 phenyl rings have been deuterated.

The results illustrate the existence of an extensive water network in the minor and major grooves of the D-DNA double helix. The peaks are consistent spatially with both the DNA and with the location of cations as determined by X-ray isomorphous replacement experiments[9].

Isotopic replacement experiments have also been undertaken with the synthetic PEEK polymer[10]. Here the structural interest is in the position of the phenyl ring in the unit cell. Figure XI.12 shows a diagram illustrating the structure of PEEK. The conformation of the polymer is described by one torsion angle (marked as $\tau$ in figure XI.12) about a dummy bond constructed across the phenyl ring. Differing values for this torsion angle have been obtained from powder and fibre X-ray diffraction studies.

The availability of the deuterated polymer form of PEEK has allowed high-angle neutron fibre diffraction experiments to be used in deciding between the two possible X-ray structures. Neutron fibre diffraction patterns collected from hydrogenated and deuterated forms of PEEK are shown in figure XI.13. These results have been used in difference Fourier studies in which the location of the hydrogen atoms about the benzene ring was determined and thereby the orientation of the phenyl ring in the unit cell. A Fourier difference map of this type is shown in figure XI.14. This study used reflections to 2Å resolution and gives a clear picture of the hydrogens around the phenyl ring in this polymer.


Figure XI.13. — High Angle Fibre Diffraction data recorded from hydrogenated ( a ) and deuterated ( b ) analogues of the PEEK polymer.



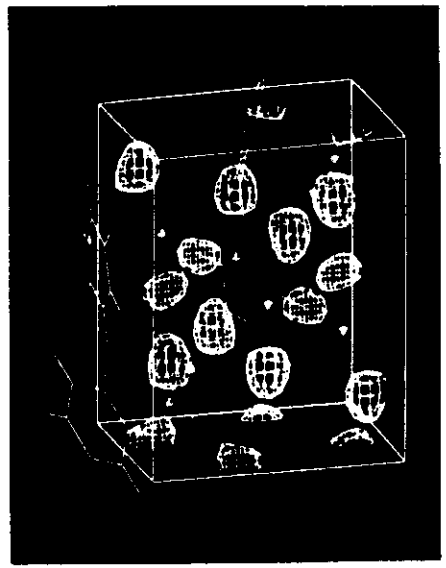

Figure XI.14 . — Fourier Difference ma calculated from the data shown in figur XI.13 using phases calculated from th model structure.

## XI.4. Conclusion

The power of fibre diffraction has been greatly enhanced by the availabilit of high intensity synchrotron radiation sources. The applications which hav been described here were chosen to demonstrate this and to illustrate the fact tha such studies have provided new information which in many cases could no have been obtained using conventional X-ray sources. However, despite th massive gain in flux which has been obtained in moving from conventional t synchrotron radiation sources, the results of time-resolved experiments on DNA PEEK and other fibrous systems have shown that many of the changes note during the study of these conformational pathways occur on a subsecon timescale. It is clear therefore that future developments in this area of polyme science for the study of both biological and non-biological systems will depen critically on steps taken to improve the available time resolution. In this conte it is also important to make the general point that many of the development which have occurred as a result of the application of synchrotron radiation to th study of condensed matter owe their success in no small measure t simultaneous developments in beamline instrumentation, camera design and i particular the development of suitable X-ray detectors. These considerations ar especially important for the development of fibre diffraction facilities capable o fully exploiting the high fluxes which will become available at sources such a the ESRF. These experiments also present formidable new problems for dat reduction and analysis and it can be expected that in the future new theoretic and computational approaches will be required for the processing of larg amounts of time-resolved data. Neutron fibre diffraction studies have als provided information on molecular conformation and solvent structure that ha traditionally been extremely difficult to obtain using X-ray fibre diffraction alon These studies have required major developments in procedures for samp preparation and also for the collection, assembly and analysis of diffractio

patterns. In particular, the use of isotopic replacement provides a very powerful method of complementing information from X-ray studies and it is expected that in the future neutron fibre diffraction will be used increasingly in parallel with X-ray studies of biological and synthetic polymers.

## REFERENCES


1. Vainshtein, B.K., in "Diffraction of X-rays by Chain Molecules" (Elsevier) (1966).
2. Fraser, R.D.B., and MacRae, T.P. in "Conformation in Fibrous Proteins" (Academic Press) (1973).
3. Cochran,W., Crick,F.H.C., and Vand,V., Acta Cryst. 5, 581-586 (1952).
4. Sherwood, D., in "Crystals, X-rays and Proteins" (Longman),(1983).
5. Mahendrasingam, A., Forsyth, V.T., Hussain, R., Greenall, R.J., Pigram, W.J., and Fuller, W., Science 233, 195-197 (1986).
6. Mahendrasingam, A., Denny, R.C., Forsyth, V.T., Greenall, R.J., Pigram, W.J., Papiz, M.Z., and Fuller, W., Inst. Phys. Conf. Ser. 101, 225-236 (1989).
7. Mahendrasingam, A., Fuller, W., Forsyth, V.T., Oldman, R.J., MacKerron, and Blundell, D.J., Rev. Sci. Instr. 63, 1087-1090 (1992).
8. Forsyth, V.T., Mahendrasingam, A., Pigram, W.J., Greenall, R.J., Bellamy, K., Fuller, W., and Mason, S.A., Int. J. Biol. Macr. 11, 236-240 (1989).
9. Forsyth, V.T., Mahendrasingam, A., Langan, P., Pigram, W.J., Stevens, E.D., Al-Hayalee, Y., Bellamy, K.A., Greenall, R.J., Mason, S.A., and Fuller, W., Inst. Phys Conf. Ser. 101, 237-248 (1989).
10. Mahendrasingam, A., Al-Hayalee, Y., Forsyth, V.T., Langan, P., Fuller, W., Oldman, R.J., Blundell, D.J., Mason, S.A., Physica B 180/181, 528-530 (1992).


# CHAPTER XII

## POLARIZED X-RAYS

M. ALTARELLI

Until recently, X-rays were hardly considered a valuable tool for the investigation of magnetic order. The experiments pioneered by de Bergevin and Brunel (1972) have shown that photons couple to electron spins, as indeed predicted from quantum electrodynamics, and that, as a consequence, X-ray diffraction can reveal the periodicity of magnetic structure, e.g. in an antiferromagnet. However, these relativistic effects are small, such that their observation with laboratory sources was a real "tour de force". The advent of synchrotron radiation sources allows an easier observation of such effects (Gibbs et al., 1985), but magnetic diffraction of X-rays remains a technique unfrequently used, if compared with neutron diffraction. Very recently, from 1986 on, a remarkable development in the application of synchrotron radiation to magnetic systems has taken place. This is to be ascribed to two facts:

a) The exploitation of the polarization properties (linear in the orbital plane, circular above or below such plane) of synchrotron radiation. A source of polarized X-rays makes magneto-optical techniques such as magnetic dichroism (linear or circular), available, which were up to now restricted to the visible or the near ultraviolet. These effects are not due to small relativistic terms, but to electric multipolar terms, of much greater intensity. The high penetration power of X-rays is a definite advantage with respect to visible light in the study of metallic samples. Furthermore in the region of hard X-rays ($\hbar\omega > 20$ keV) circular polarization allows the measurement of spin-resolved Compton spectra. These techniques are discussed elsewhere in these lectures.

b) The discovery in 1988 of Resonant Exchange Scattering of X-rays (Gibbs et al., 1988; Hannon et al., 1988), a process which yields magnetic information, with a cross-section at least 3 orders of magnitude bigger than conventional magnetic diffraction. In this case, one takes advantage not only of the polarization features, but also of the "white" spectrum of synchrotron radiation, which allows selection of photons in resonance with an absorption threshold of a magnetic ion. In the present paper we shall discuss the salient features of non-resonant and resonant magnetic scattering of X-rays in the elastic regime. The topic is developed in the following way: first we recall, in this introductory subsection, some elementary concepts about the polarization of photons. Then we briefly describe the polarization properties of synchrotron sources. The two following subsections are devoted to the discussion of magnetic diffraction and of resonant exchange scattering experiments.

Consider a beam of photons propagating in the z direction. The electric field vector is confined in the x y plane and the polarization vector for a given photon in the beam can be represented in any two basis vectors in this plane, e.g.

# 6.1 What X-rays tell us about muscle contraction—then and now

*Hugh E. Huxley*

Striated muscle is a system that has been extensively studied by X-ray diffraction over a remarkably long period of time, some 70 years, beginning in the 1920s and 1930s, with Herzog and Jancke (1926) and Boehm and Weber (1932) who observed an oriented X-ray diagram, with Astbury's recognition of the characteristic and unchanging α-protein pattern in muscle in the late 1930s (Astbury and Dickinson 1940), and continuing right up to the present day with new and interesting findings, and, I am sure, extending on into the future for some time yet. How has it come about that this one type of tissue and one technique has been able to provide new information, decade after decade, for so long?

The underlying reason is, of course, that the basic nature of the structure is such that a great deal of the information that we need is potentially available in a very convenient form. To generate the forces that are needed to move animals around at a competitive speed, very large numbers of energy-transducing elements are needed, acting in series and parallel, and all have to be oriented in the same direction so that all their elementary contributions are additive. The molecules concerned are therefore built into repeating assemblies, or filaments, and the assembly mechanisms that nature uses result in a regular spatial repeat of the molecules in the filaments. Thus the nature of the tissue inherently provides one with a large amount of regularly diffracting material. To collect a fairly detailed two-dimensional X-ray diffraction diagram of a muscle requires that something like $10^{12}$–$10^{13}$ X-ray photons be incident upon it, giving about $10^{7}$–$10^{8}$ or so photons in the recorded pattern. The volume of muscle involved might contain approximately $10^{14}$ myosin molecules, so that there are plenty of them to provide the information even if they get destroyed in the process.

The reason that the X-ray study of muscle has been such a long drawn out endeavour is that our means of producing X-rays have been extraordinarily inefficient, so that available beam intensities have been weak and increasing them has been a lengthy process. At the same time, however, one must point out that the time-scale over which we have been in a position to ask sensible questions about muscle has become progressively shorter and shorter, and X-ray technology has really done quite a good job in keeping up with other types of information.

The two periods that I would like to compare in the 'then' and 'now' of my title are the mid-1960s, when much of the elementary information about muscle contraction was obtained by using normal laboratory-based X-ray tubes and X-ray film to record the images, and the present era, when we have gone quite a long way in exploiting the possibilities of synchrotron radiation (though with still some significant distance to go) and when the much more extensive information we now have provides answers to many questions but also reveals further intriguing problems, still to be understood.

## Experimental results up to and including the 1960s

The important features of the muscle system that had been established using X-ray diffraction by the mid-1960s were the following, approximately in the order of their discovery.

1. The fibrous proteins present in muscle give an α-type wide-angle X-ray diagram, and much of the structure remains in this configuration during contraction (Astbury and Dickinson 1940). These parts of the pattern are generated by the α-helical coiled-coil structures of the rod portions of the myosin molecules in the thick filaments and the tropomyosin molecules in the thin filaments. The result, as we would now interpret it, indicates that large overall changes in myosin backbone configuration are not involved in contraction, but much more detailed measurements would be needed to rule out much more restricted changes.
2. Actin and myosin molecules are present in separate filaments forming a double hexagonal lattice array (Huxley 1951, 1952, 1953).
3. The axial periodicities within these filaments remain practically constant during both passive and active length changes of muscle (Huxley 1952, 1953; Elliott *et al.* 1967; Huxley and Brown 1967).
4. Myosin heads form a regular helical array around the thick filaments in a resting muscle, but move nearer the actin filaments during contraction and in rigor (Huxley 1968; Haselgrove and Huxley 1973).
5. The myosin heads have considerable flexibility in their attachment to the myosin backbone. In rigor, they attach to actin and adopt the helical parameters of the actin filament. In contraction, they also lose their myosin-based helical characteristics but retain a strong 14.5-nm axial periodicity. Labelling of the actin pattern is much weaker than in rigor (Elliott *et al.* 1967; Huxley and Brown 1967).
6. Much of the underlying actin structure seems to remain unchanged during both rigor and contraction (Huxley and Brown 1967). However, large changes in intensity at wider angles on the second actin layer line could be interpreted in terms of a lateral tropomyosin shift in the thin filaments associated with activation (Haselgrove 1972; Huxley 1972; Vibert *et al.* 1972; Parry and Squire 1973).



These findings provided a good deal of the experimental basis for the sliding-filament, moving-crossbridge mechanism of muscle contraction, which I think one can say was well-established if not universally believed by 1970—although its essential features had been described much earlier. (Hanson and Huxley 1955; Huxley, A. F. 1957) After about 25 years of further experience with the system, I think it is fair to say that all these findings and the basic conclusions drawn from them have turned out to be correct.

## Current research

Since then, the basic question has been, 'How do the moving crossbridges (myosin heads) produce the sliding force between the actin and myosin filaments?'. This has proved to be a remarkably difficult question to answer, so much so that a few people (e.g. Pollack 1983) have been tempted to believe that some totally different mechanism might be involved, perhaps involving changes in myosin filament length. However, light microscope pictures showing fluorescently labelled single actin filaments, *in vitro*, sliding unidirectionally in the presence of adenosine triphosphate (ATP) over surfaces covered with isolated purified myosin $S_1$-head subunits (Toyashima *et al.* 1987), and force measurements on such preparations of myosin $S_1$ and actin (Kishino and Yanagida 1988) now make it very difficult to argue for any alternative mechanism.

During this time, the power of the methods available for carrying out X-ray studies on muscle has been increased enormously, by the use of synchrotron radiation, by the use of electronic X-ray detectors of various kinds and of imaging plates, and by carrying out much more sophisticated physiological manipulation of muscle, and even of single muscle fibres, during the diffraction experiments.

The results of these experiments can be divided into three categories. There are those that provide straightforward experimental verification of various features postulated in the basic model but not previously demonstrated. There are other results that fit into the basic model, but reveal some more novel aspect of it, not quite as originally imagined. And then there are the really surprising results, which confront us with the fact that there are layers of subtlety and complication about this basic mechanism that are still able to exercise our ingenuity and imagination.

In the first category I would put all the time-resolved measurements on equatorial and myosin layer line reflections that show that the overall time course of the movement of the myosin heads toward the actin filaments, and away from the myosin helical lattice, at the start of contraction, and that their return, again during relaxation, is closely correlated with the development of tension in a stimulated muscle and its decline when stimulation stops (Huxley 1975; Huxley and Haselgrove 1976; Sugi *et al.* 1977; Matsubara and Yagi 1978; Huxley *et al.* 1982). In the second category I would place some of

the finer details of these measurements which indicate that attachment of crossbridges to actin precedes full tension development by those attached crossbridges. This has been very amply confirmed recently by studies on length-clamped single muscle fibres, in which internal shortening is prevented and therefore cannot be delaying the tension rise (Cecchi *et al.* 1991). Also included would be measurements of the increase in actin second layer line intensity that show that it manifests itself even sooner after stimulation, some 10–15 ms earlier than crossbridge attachment in frog muscle at 8°C, and still occurs in the absence of actin–myosin filament overlap in very stretched muscles (Kress *et al.* 1986). These observations indicate that changes in thin filament structure (possibly tropomyosin movement) take place autonomously in the thin filaments in response to calcium binding, that subsequent initial attachment of crossbridges occurs with a significant delay, and that a further rate process has to occur before the attached crossbridges can exert full tension. These are all rather important features, not originally self-evident, but fitting in comfortably with the original scheme though not with certain biochemical kinetic models (Williams *et al.* 1988).

Perhaps the most critical question to be approached concerns the so-called 'working stroke' of the crossbridges. During contraction, as the actin filaments slide past myosin heads under load and mechanical work is performed, hydrolysis of ATP is effected by the actin–myosin head complex and some kind of structural cycle or cycles must take place in the myosin–actin interaction. The part of the cycle when force and movement are actually being generated is known as the 'working stroke' of the crossbridge, though, in principle, the myosin head could remain stationary relative to the thick filaments and the actin alone could move. To repeat a question I asked at a much earlier meeting, 'What evidence is there that the crossbridge can be attached to actin in more than one configurational state, and that transitions between the states develop the force for contraction?' (Huxley 1980). Observations of the disordering of the helical arrangement of myosin heads at the onset and throughout contraction do not necessarily show that directed movement of a myosin head takes place during every or any working stroke. However, the question can be approached using the very important observations made by Huxley and Simmons (1971) of very rapid tension recovery taking place in a muscle following small but rapid length decreases. These observations showed an instantaneous elastic response to the immediate length change, followed by tension recovery with a time constant of the order of a millisecond in frog muscle at 2°C; releases corresponding to 4-nm relative filament sliding in each half sarcomere could give almost complete loss of tension and almost complete recovery. Thus a very considerable synchronization of crossbridge action must be taking place.

In experiments using whole muscle in the early 1980s (Huxley *et al.* 1981, 1983) it was found that a large decrease in intensity of the 14.5-nm meridional reflection took place when such a small but rapid quick release was applied to



an otherwise isometrically contracting muscle. The intensity change took place in about a millisecond, but was delayed by 1/2–1 ms on the length change. However, it could not be established absolutely definitely whether the intensity change was associated with the slightly delayed tension recovery process itself, i.e. the synchronized working strokes, or with the passive elastic change that immediately preceded it, although the former was thought more probable. The uncertainty arose because of uncertain synchronization of mechanical events along a large intact muscle on a ms time-scale. Surprisingly, much of the intensity decrease was reversed within the 5–10 ms following the quick release; this was interpreted as due to rapid crossbridge reattachment in a configuration close to the original one. The experiments clearly showed that a major change takes place in the axial configuration of the crossbridges that generate the 14.3 meridional reflection, either during the initial drop in tension or during the subsequent tension recovery. Either way, crossbridges attached to the moving actin filaments must undergo a change in their longitudinal density distribution.

This question has now been decisively settled by some very beautiful and important experiments performed recently by Irving and his colleagues (1992) on single fibres using the Daresbury Storage Ring. By using a striation follower to measure sarcomere length in the region of the fibre illuminated by the X-ray beam and a repetitive release technique to augment total exposure, they were able to achieve a 0.2 ms time resolution and to show that the intensity decrease is indeed associated with the rapid tension recovery phase, i.e. with the working stroke and not with the initial drop in tension. Thus changes in the axial configuration of the crossbridges definitely do occur during the working stroke. I think this is a major triumph for X-ray diffraction, since a large number of very sophisticated optical and spin resonance techniques have failed to produce useful evidence about such a change, perhaps because of interfering signals generated by random movements of some or all of the myosin heads. The X-ray reflection monitors one particular feature of the structure. It is this signal that seems to track most satisfactorily with the detailed physiological state of the muscle.

Most intriguing of all is the third category of results, the really unexpected ones. In fact, we came across one of these quite early on, in the early 1970s, although we couldn't be sure at the time that it wasn't some sort of artefact, since we were still using laboratory X-ray tubes, and rapid time-resolved experiments were difficult. The experiment was a fairly obvious one, to apply a quick release of about 2–3 per cent to a whole muscle, enough to drop tension to near zero and for tension then to recover only at the slower rate characteristic of normal muscle shortening taking up the slack in series elastic elements. With a shortening of 20–30 nm per half sarcomere, one would have expected all the crossbridges to go through a detached phase before reattaching and generating tension again, with a delay similar to that seen at the outset of contraction. Instead, we saw very little change in the equatorial

intensities, as if neither the working stroke nor the subsequent detachment had any effect on the lateral density distribution of the crossbridges. Under these conditions, there was no sign of a partial return to a relaxed or detached configuration. This puzzling finding was in fact one of my motivations for continuing to work on muscle at a time when a number of people thought the problem was already solved.

When Simmons and I and our colleagues (Huxley *et al.* 1981, 1983) carried out the rapid release experiments using synchrotron radiation, and saw the large changes in the 14.3-nm meridional reflection, we again found no change in the intensity of the equatorial reflections either during the release itself (and the presumed synchronized working stroke of many crossbridges) nor during the subsequent tension recovery, even though we looked extremely hard for them. We published this result, pointing out the restriction it imposed on the exact geometry of the working stroke, and the implication that release at the end of a rapid stroke was followed by extremely rapid reattachment, an implication that did not attract much attention at the time.

We looked into this further by studying the onset of rapid shortening in a muscle (starting from an isometric contraction) looking first at the equatorial intensities, which we knew from previous work (Huxley 1979) did, in fact, change toward the relaxed (detached) values during more prolonged rapid shortening. We also made careful measurements of the exact value of the 14.3-nm axial spacing, which we knew increased by about 1.3 per cent between the relaxed (unattached) and contracting (attached) states. In each case, we found that, after shortening started, there was a significant delay, of 15–25 ms at the shortening velocities in the experiment (about 2.5 $l_o$ per second) before the expected changes manifested themselves (Huxley *et al.* 1989). This corresponded to a distance of sliding of about 500 Å before X-ray evidence for normal detachment was seen, even though tension reached its steady low value much earlier. The phenomenon is probably related to the rapid recovery of 14.3 intensity, already described, which occurs after a rapid release and may also be indicating rapid reattachment; it may be that these effects are another manifestation of the multiple structural cycle effect described by Lombardi *et al.* (1992) and of the long working stroke behaviour described by Yanagida (Yanagida *et al.* 1985; Ishijima *et al.* 1991). Whether these are multiple cycles of a conventional kind, or whether some new property of the system has to be invoked to explain them, remains to be seen. This question is now in the forefront of ideas about the mechanism of muscle contraction.

## Future perspectives

Even with the synchrotron radiation sources available in the 1980s, available X-ray intensity has been a limiting factor and X-ray studies have progressed fairly slowly since the basic behaviour of the stronger equatorial and meridional reflections was worked out. The off-meridional actin and myosin layer line reflections are much weaker and need to be studied with inconveniently long total exposure times built up from runs on many muscles if their radial intensity distribution is to be reliably measured during changes even with a 5 or 10 ms time resolution. This is very unsatisfactory, especially when using multiple two-dimensional electronic counters whose spatial sensitivity and positional scaling can vary with time.



It is now particularly important to be able to visualize the behaviour of all the weaker parts of the two-dimensional X-ray pattern from muscle on a millisecond or submillisecond time-scale, as we have seen from the quick-release experiments. Our approach to the several problems involved is the following. First of all, one has to have a much larger total flux than has been hitherto available; this can be achieved on the 25-pole wiggler beamline at CHESS (Cornell) with a new small-angle scattering camera that we (Stewart, Sosa, and Huxley from Brandeis; Irving from Cornell) have designed and built. This provides us with a total incident flux in excess of $10^{13}$ photons/s, and a total flux in the diffraction diagram of the order of $10^8$ photons/s. This is what is needed for the time resolution required, but it would clearly overwhelm any two-dimensional multiwire counter likely to be available in the very near future. Moreover, the total incident flux that a muscle can sustain before radiation damage becomes significant is sufficient only for one or two short time frames repeated during the required number of contractions. We therefore make a virtue of necessity and record the patterns on imaging plates, avoiding the flux rate problem, and look at only two time slots in each experimental run, avoiding the radiation damage problem. Since we can obtain excellent patterns extending beyond the 2.7-nm actin meridional reflection in a total exposure time of the order of 100 ms on imaging plates with this camera and beam line, and since we can obtain shutter open times in the ms range and have muscles perform the requisite total number of contractions (e.g. 50 or 100), the approach seems highly feasible and the pattern recorded so far extremely promising (see also Chapter 6.14, this volume.)

## Conclusion

In summary, therefore, it seems that X-ray diffraction has made major contributions toward defining and answering major current problems in muscle contraction over a long time period, and X-ray technology has kept pace with the increasing sophistication of our understanding of the molecular mechanism. If the crucial information about the nature of the working stroke is indeed present in the two-dimensional X-ray diagrams during and after quick-release transients, it should now be accessible by the methods I have described.

## References

Astbury, W. T. and Dickinson, S. (1940). X-ray studies of the molecular structure of myosin. *Proceedings of the Royal Society*, **B129**, 307–22.

Boehm, G. and Weber, H. H. (1932). Das Röntegendiagramm von gedehuten Myosin fäden. *Kolloid-Zeitschrift*, **61**, 269–70.

Cecchi, G., Griffiths, P. J., Bagni, M. A., Ashley, C. C., and Maeda, Y. (1991). Time-resolved changes in equational X-ray diffraction and stiffness during use of tetanic tension in intact length-clamped single muscle fibers. *Biophysical Journal*, **59**, 1273–83.

Elliott, G. F., Lowy, J., and Millman, B. M. (1967). Low angle X-ray diffraction studies of living striated muscle during contraction. *Journal of Molecular Biology*, **25**, 31–45.

Hanson, J. and Huxley, H. E. (1955). The structural basis of contraction in striated muscle. *Symposia of the Society for Experimental Biology*, **9**, 228–64.

Haselgrove, J. C. (1972). X-ray evidence for a conformational change in the actin-containing filaments in vertebrate skeletal muscle. *Cold Spring Harbor Symposium of Quantitative Biology*, **37**, 341–52.

Haselgrove, J. C. and Huxley, H. E. (1973). X-ray evidence for radial crossbridge movement and for the sliding filament model in actively contracting skeletal muscle. *Journal of Molecular Biology*, **77**, 549–68.

Herzog, R. O. and Jancke, W. (1926). Röntgenographische Untersuchungen am Muskel. *Naturwissenschaften*, **14**, 1223-A.

Huxley, A. F. (1957). Muscle structure and theories of contraction. *Progress in Biophysics*, **7**, 255–318.

Huxley, A. F. and Simmons, R. M. (1971). Proposed mechanism of force generation in striated muscle. *Nature*, **233**, 533–8.

Huxley, H. E. (1951). Low-angle X-ray reflections from living muscle. *Discussions of the Faraday Society*, **11**, 148–9.

Huxley, H. E. (1952). The structure of muscle. Ph.D. thesis, University of Cambridge.

Huxley, H. E. (1953). X-ray diffraction and the problem of muscle. *Proceedings of the Royal Society*, **B141**, 59.

Huxley, H. E. (1968). Structural differences between resting and rigor muscle. *Journal of Molecular Biology*, **38**, 507–20.

Huxley, H. E. (1972). Structural changes in the actin- and myosin-containing filaments during contraction. *Cold Spring Harbor Symposium of Quantitative Biology*, **37**, 361–76.

Huxley, H. E. (1975). The structural basis of contraction and regulation in skeletal muscle. *Acta Anatomica Nipponica*, **50**, 301–25.

Huxley, H. E. (1979). Time-resolved X-ray diffraction studies on muscle. In *Cross-bridge mechanism in muscle contraction* (ed. H. Sugi and G. H. Pollack), pp. 391–402. University of Tokyo Press, Tokyo.

Huxley, H. E. (1980). The movement of myosin crossbridges during contraction. In *Muscle contraction: Its regulatory mechanism* (ed. S. Ebashi, K. Maruyama, and M. Endo), pp. 33–43. Japan Sci. Society Press, Tokyo/Springer-Verlag, Berlin.

Huxley, H. E. and Brown, W. (1967). The low angle X-ray diffraction diagram of vertebrate striated muscle and its behaviour during contraction and rigor. *Journal of Molecular Biology*, **30**, 382–434.

Huxley, H. E. and Faruqi, A. R. (1983). Time-resolved X-ray diffraction studies on vertebrate striated muscle. *Annual Reviews of Biophysics and Bioengineering*, **12**, 381–417.

Huxley, H. E. and Haselgrove, J. C. (1976). The structural basis of contraction in muscle and its study by rapid X-ray diffraction methods. In *Myocardial failure* (ed.



Huxley, H. E., Simmons, R. M., Faruqi, A. R., Kress, M., Bordas, J., and Koch, M. H. J. (1981). Millisecond time-resolved X-ray changes in X-ray reflections from contracting muscles during rapid mechanical transients, recorded using synchrotron radiation. *Proceedings of the National Academy of Science, USA*, **78**, 2297–301.

Huxley, H. E., Faruqi, A. R., Kress, A. R., Bordas, J., and Koch, M. H. J. (1982). Time resolved X-ray diffraction studies of the myosin layer line reflections during muscle contraction. *Journal of Molecular Biology*, **158**, 637–84.

Huxley, H. E., Simmons, R. M., Faruqi, A. R., Kress, M., Bordas, J., and Koch, M. H. J. (1983). Changes in the X-ray reflections from contracting muscle during rapid mechanical transients and their structural implications. *Journal of Molecular Biology*, **169**, 469–506.

Huxley, H. E., Simmons, R. M., and Faruqi, A. R. (1989). Time course of spacing change of 143 Å meridional crossbridge reflection during rapid shortening. *Biophysical Journal*, **55**, 12a.

Irving, M., Lombardi, V., Piazzesi, G., and Ferenczi, M. (1992). Myosin head movements are synchronous with the elementary force generating process in muscle. *Nature*, **357**, 156–8.

Ishijima, A., Doi, T., Sakurada, K., and Yanagida, T. (1991). Sub-piconewton force fluctuation of actomyosin *in-vitro*. *Nature*, **352**, 301–6.

Kishino, A. and Yanagida, T. (1988). Time course of spacing change of 143 Å meridional crossbridge reflection during rapid shortening. *Nature*, **334**, 74–6.

Kress, M., Huxley, H. E., Faruqi, A. R., and Hendrix, J. (1986). Structural changes during activation of frog muscle studied by time-resolved X-ray diffraction. *Journal of Molecular Biology*, **188**, 325–42.

Lombardi, V., Piazzesi, G., and Linari, M. (1992). Rapid regeneration of the actin–myosin power stroke in contracting muscle. *Nature*, **355**, 638–41.

Matsubara, I. and Yagi, N. (1978). A time-resolved X-ray diffraction study of muscle during twitch. *Journal of Physiology*, **278**, 297–307.

Parry, D. A. D. and Squire, J. M. (1973). Structural role of tropomyosin in muscle regulation; analysis of the X-ray diffraction patterns from relaxed and contracting muscles. *Journal of Molecular Biology*, **75**, 33–55.

Pollack, G. H. (1983). The cross-bridge theory. *Physiological Review*, **63**, 1049–113.

Sugi, H., Amemiya, Y., and Hashizume, H. (1977). X-ray diffraction of active frog skeletal muscle before and after a slow stretch. *Proceedings of the Japanese Academy*, **53**, 178–82.

Toyashima, Y., Kron, S. J., McNally, E. M., Niebling, K. R., Toyashima, C., and Spudich, J. A. (1987). Myosin subfragment-1 is sufficient to move actin filaments *in-vitro*. *Nature*, **328**, 536–9.

Vibert, P. J., Haselgrove, J. C., Lowy, J., and Poulsen, F. R. (1972). Structural changes in actin-containing filaments of muscle. *Journal of Molecular Biology*, **71**, 757–67.

Williams, D. L., Greene, L. E., and Eisenberg, E. (1988). Cooperative turning on of myosin subfragment/adenosinetrephosphatase activity by the troponin–tropomyosin–actin complex. *Biochemistry*, **27**, 6987–93.

Yanagida, T., Arata, T., and Oosawa, F. (1985). Sliding distance of actin filament induced by a myosin crossbridge during one ATP hydrolysis cycle. *Nature*, **316**, 366–9.

Time-resolved X-ray diffraction studies of the myosin layer-line reflections during muscle contraction. *Journal of Molecular Biology*, **158**, 637–84.

Rome, E., Hirabayashi, T., and Perry, S. V. (1973). X-ray diffraction of muscle labelled with antibody to troponin C. *Nature*, **244**, 154–5.

Towns-Andrews, E., Berry, A., Bordas, J., Mant, G. R., Murray, P. K., Roberts, K., Sumner, I. L., Worgan, J. S., Lewis, R. A., and Gabriel, A. (1989). Time-resolved X-ray diffraction station: X-ray optics, detectors and data acquisition. *Review of Scientific Instruments*, **60**, 2346–9.

Worgan, J., Lewis, R. L., Fore, N. S., Sumner, I. L., Berry, A., Parker, B., D'Annunzio, F., Martin-Fernandez, M. L., Towns-Andrews, E., Harries, J. E., Mant, G. R., Diakun, G. P., and Bordas, J. (1990). The application of multiwire X-ray detectors to experiments using synchrotron radiation. *Nuclear Instruments and Methods in Physics Research*, **A291**, 447–54.

# 6.4 X-ray diffraction evidence for a specific actomyosin complex in live isometrically contracting frog sartorius muscle

*M. L. Martin-Fernandez, G. P. Diakun, F. G. Diaz, J. E. Harries, R. A. Lewis, J. Lowy, G. R. Mant, E. Towns-Andrews, and J. Bordas*

Given the sensitivity and speed of synchrotron radiation (SR) X-ray diffraction techniques, one would expect to be able to tackle directly one of the crucial questions concerning force generation in living muscles, namely, whether there exists an *in vivo* equivalent to the actomyosin complex which has been studied in solution or deduced from electron microscopy and X-ray diffraction experiments on rigor muscles.

Early experiments in which the X-ray diffraction patterns of relaxed and rigor frog muscles were compared showed that the layer lines due to the three-dimensional arrangement of myosin heads in the rest state disappear and are replaced by a new set that look weaker, are more diffuse, and occur at axial spacings corresponding to submultiples of the pitch of the actin helix (Huxley and Brown 1967; Haselgrove 1975). The interpretation was that, following nucleotide depletion, the myosin heads attach to actin at specific sites and with a specific configuration, thus generating 'decorated' actin layer lines. Subsequently, it was suggested that the rigor head configuration may correspond to the end of the working stroke in the crossbridge cycle (Huxley 1969). To test this, an intensive search was made for the presence of actin-based layer lines in isometrically contracting living frog muscles, but this endeavour was not successful (Huxley *et al.* 1982). To help clarify this situation some results are presented from two different types of experiments carried out at station 2.1 of the Daresbury SR source.

In the first set of experiments, X-ray diffraction patterns from frog sartorius muscles of *Rana esculenta* undergoing 800 ms long tetani were collected using a multiwire gas proportional area detector in conjunction with a 6.5 m long camera. This camera length was used to ensure good resolution between the layer lines. Patterns were recorded at rest, at 30 per cent remnant tension (collected during the recovery phase following the end of stimulation and with a time resolution of 50 ms) and at the plateau of tension (time resolution of 600 ms) following a second stimulus applied at 30 per cent remnant tension. A total of 780 contractions using 13 muscles (i.e. an average of *ca.* 60

contractions per muscle) were recorded. It should be pointed out that the tension developed by each muscle never fell by >15 per cent of its original value and the patterns recorded at the plateau of tension following the first and the second stimuli were essentially identical.

In a second set of experiments, data were recorded using image plates (Molecular Dynamics Ltd) and a camera length of 2.5 m. Data at rest and at the plateau of tension (1 s resolution) were averaged from seven muscles, each of which was stimulated by 40 tetani of 1.2 s duration applied every 3 min. Thus we obtained an accumulated total of 280 contractions.

Further details about the experimental set-up, data collection, processing procedures, and of other results obtained from these experiments are reported elsewhere (Towns-Andrews *et. al.* 1989; Bordas *et al.* 1991, 1992).

## Patterns at rest, 30 per cent remnant tension, and plateau of tension

The rest pattern (Fig. 1(a)) is essentially identical to that previously reported (Huxley and Brown 1967). The data show: (1) the strong myosin layer lines (Figs 1(a) and 2(a)) arising from the quasi-helical disposition of the heads with a pitch of *ca.* 42.9 nm and an axial rise of *ca.* 14.34 nm; these layer lines are sampled due to the packing of the filaments in a hexagonal superlattice (Luther and Squire 1980); (2) the (1,0,0), (1,1,0), (2,0,0), (2,1,0), and (3,0,0) equatorial reflections; and (3) four meridional bands at spacings of *ca.* 44.0, 38.2, 19.1, and 12.75 nm. The 44.0 nm band originates from the C protein in the thick filaments (Rome *et al.* 1973*a*), whilst the 38.2, 19.1, and 12.75 nm bands arise from the disposition of the troponin molecules in the thin filaments (Rome *et al.* 1973*b*). From accurate measurements (using image plates) of the spacings of the actin layer lines at *ca.* 5.9, 5.1, and 2.73 nm, we deduce that the actin filament can be closely approximated by a non-integral helix with a long pitch of *ca.* 72.9 nm.

Comparison of the pattern at rest (Fig. 1(a)) with that at the plateau of tension (Fig. 1(c)) shows that: (1) the (1,0,0) and (1,1,0) equatorial reflections undergo the well-known intensity loss and gain, respectively; (2) the myosin layer lines and the 21.5 nm meridional cluster of reflections decrease considerably in intensity and the lattice sampling vanishes; (3) the meridional intensities of the 44.0 and 38.2 nm reflections decrease substantially; (4) the spacings of the third and fourth myosin layer lines increase by *ca.* 1.6 per cent from 14.34 to 14.58 nm and 10.75 to 10.93 nm, respectively (Fig. 2) and their meridional maxima more than double in radial width (Fig. 1(a) and (c)); the same spacing increase of *ca.* 1.6 per cent occurs in all the other myosin layer lines (results not shown); (5) a new set of layer lines appears at spacings of *ca.* 37.0, 24.0, 19.0, 18.0, 14.58, 10.9, and 10.4 nm (Fig. 2); these spacings correspond closely to those seen in rigor patterns by Huxley and Brown (1967).



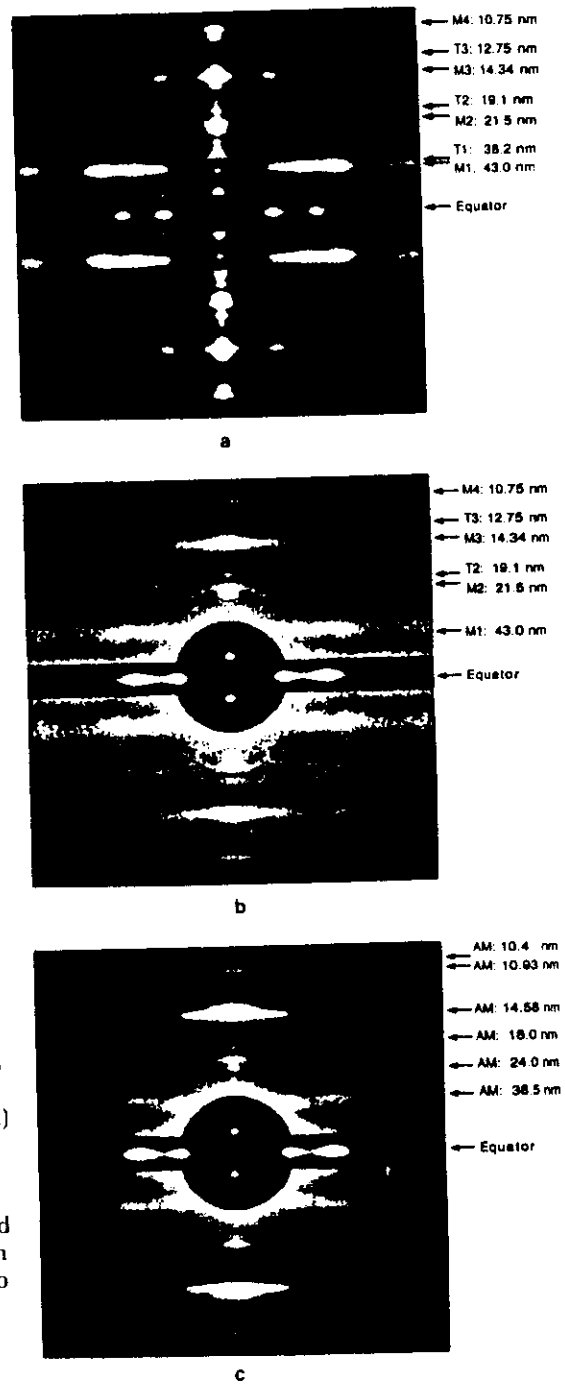


**Fig. 1** Background-subtracted X-ray diffraction patterns recorded with a camera length of 6.25 m. (a) Rest; (b) 30 per cent remnant tension; and (c) plateau of tension. The intensity in the equator and in the central ring has been reduced by a factor of 40 to allow simultaneous visualization of all the features in the patterns.

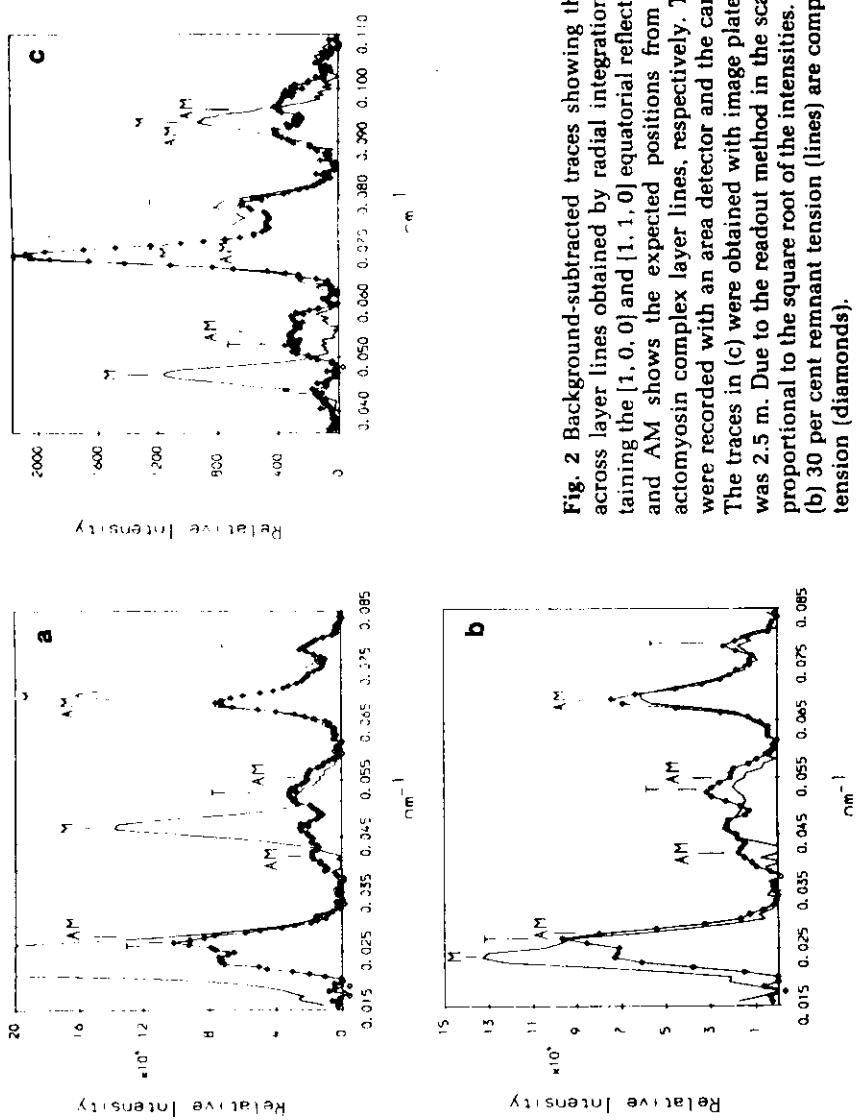


**Fig. 2** Background-subtracted traces showing the intensity distribution across layer lines obtained by radial integration within the region containing the [1, 0, 0] and [1, 1, 0] equatorial reflections. The labelling M, T, and AM shows the expected positions from myosin, troponin, and actomyosin complex layer lines, respectively. The traces in (a) and (b) were recorded with an area detector and the camera length was 6.25 m. The traces in (c) were obtained with image plates and the camera length was 2.5 m. Due to the readout method in the scanner the vertical axis is proportional to the square root of the intensities. In (a) and (c) rest, and in (b) 30 per cent remnant tension (lines) are compared with the plateau of tension (diamonds).



It is clear from the above that a major difference between rest and plateau of tension patterns is the loss of crystallographic order in the latter. We have shown elsewhere (Bordas *et al.* 1992) that intensity changes due to loss of such order occur very soon after activation, and that the recovery of order lags well behind tension relaxation. Furthermore, the loss of order is only indirectly related to the formation of an actomyosin (AM) complex. Thus, to compare intensities between an active and a largely inactive state in equivalent conditions of disorder, we chose the 30 per cent remnant tension state. This procedure was based on the observation that at that stage the muscle gave patterns in which the crystallographic order characteristic of the rest state was still practically absent, whilst the relative intensities of the myosin-based layer lines, especially on the meridian, were similar to those observed at rest. Moreover, the diffraction patterns showed very few of the features associated with active tension production. Therefore we argue that the transient state recorded at 30 per cent remnant tension best approximates a crystallographically unsampled inactive state which it is more appropriate to use to make intensity comparisons with the active state at the plateau of tension.

## New layer lines at the plateau of tension

The above considerations indicate that one cannot make quantitative intensity comparisons between the rest and plateau of tension states. Nevertheless, the traces in Fig. 2(a) reveal that, at the plateau of tension, the layer lines at *ca.* 24.0 nm and in the region of 19.0–18.0 nm are stronger than at rest. Due to the dominance of the neighbouring 43.0 nm layer line, it is not clear whether any intensity change occurs in the layer line at 37.0 nm (Fig. 2(a)). From the image plate data in Fig. 2(c) one can see that the intensity increase in the 19.0–18.0 nm region arises from two superimposed maxima at spacings of 19.0 and 18.0 nm. The former indexes as the second order of the troponin periodicity whilst the latter is located at the position of the fourth actin layer line. Figure 2(c) also shows two distinct bands in the region of the fourth myosin layer line. One of these at *ca.* 10.9 nm (arising as a result of the *ca.* 1.6 per cent spacing change in the fourth myosin layer line) decreases in intensity, whilst the other at *ca.* 10.4 nm (located at the position of the seventh actin layer line), clearly shows an increase in intensity.

As explained above, by performing experiments in which the crystallographic order is largely absent, a more quantitative comparison can be made. Intensity comparisons between the 30 per cent remnant tension and the active state at the plateau of tension show that the 19.0 and 18.0 nm reflections have increased by *ca.* 180 per cent, whilst there may be a slight increase in the 37.0 nm layer line (Fig. 2(b)). Note that the 24.0 and 10.4 nm reflections are absent at 30 per cent remnant tension (Bordas *et al.* 1992). In summary, this intensity comparison shows that, when the loss of order is not contributing to the intensity changes, then all the layer lines indexing as a

submultiple of the *ca.* 72.9 nm actin repeat increase in intensity to a lesser or greater degree. In addition, the intensity of the third myosin layer line increases by *ca.* 20 per cent and its spacing changes from *ca.* 14.4 to 14.58 nm, that is, it shows, although less pronounced, a trend similar to that seen when the muscle is stimulated from rest. Moreover, we have noted (Chapter 6.3, this volume) that, following stimulation from 30 per cent remnant tension, the intensity of the third myosin layer line increases by *ca.* 370 per cent.

The intensity increase of these several layer lines during contraction provides evidence for the formation of an AM complex because: (1) the ones at spacings of *ca.* 24.0, 18.0, and 10.4 nm show an increase well outside the radial positions expected for contributions arising from tropomyosin motion and/or actin conformational changes, and, given their spacings, this change must be free of any troponin contributions; (2) layer lines with similar axial spacings are also seen in rigor muscles, where they are thought to indicate the labelling of the thin filaments by myosin heads (Haselgrove 1975). Additional support that this also applies to the contracting muscle comes from studies of structural kinetics (Bordas *et al.* 1992).

We therefore propose that, in a situation where an AM complex is formed during isometric contraction, the diffraction features cannot be described as being either thick or thin filament-based. Thus we define a minimum axial repeat for the AM complex. This can be derived from the inverse of the positions of the two most closely spaced layer lines which appear at the plateau of tension, namely, those at *ca.* 10.9 and 10.4 nm. From these it can be calculated that a minimum repeat of the actomyosin complex is *ca.* 218.7 nm ($(10.41\ \text{nm})^{-1} - (10.93\ \text{nm})^{-1} = (218.7\ \text{nm})^{-1}$). Hence, all the layer lines observed at the plateau of tension at axial spacings of *ca.* 37.0, 24.0, 21.8, 18.0, 14.58, 10.9, and 10.4 nm index as the 6th, 9th, 10th, 12th, 15th, 20th, and 21st orders of this long 218.7-nm repeat, respectively. Consequently, though by convention some of these layer lines would be referred to as actin- or myosin-based, we would argue that all of them are attributable to the presence of an AM complex at the plateau of tension state. It may be noted that the axial lattice defined for this AM complex is identical, or at least has all the basic features, to that proposed for the AM complex in rigor (Squire and Harford 1988), suggesting that in both cases the interacting sites follow the actin lattice.

The question that naturally arises is whether the AM complex described at the plateau of tension is identical to that observed in rigor? A comparison of the intensity distribution across the layer lines shows that they are all weaker at the plateau of tension: the one at 37.0 nm by *ca.* 80 per cent, those at 24.0 and 18.0 nm by 20–30 per cent, and the one at 14.58 nm by about 50 per cent. In contrast, measurements of the 14.58 nm meridional intensity reveal that at the plateau of tension it is stronger by about 800 per cent. Thus, not only the absolute intensities but also the relative intensities differ between these two states. Therefore, the AM complex at the plateau of tension cannot be the same as in rigor. This can be explained if one assumes that the myosin heads that attach to actin at the plateau of tension do not follow the helical order of the thin filament as is the case when they attach in rigor (Haselgrove 1975), and/or that the myosin heads have a different axial orientation (as they must in order to account for the large intensity difference in the meridional region of the 14.58 nm layer line; Bordas *et al.* 1992). It is relevant to point out here that activation events associated with tropomyosin motions may also contribute to the relative weakness of the 37.0 nm reflection (Yagi and Matsubara 1988).



Given that the evidence we have presented shows that the AM complexes in rigor and contraction are different, is it possible to estimate the number of myosin heads that interact with the thin filament at the plateau of tension? This cannot be done by comparing the intensities of individual layer lines in the two states because, as the relative intensities of the two sets of layer lines are different, each layer line would provide a different measure of attachment. Thus, we conclude that a comparison between the intensities of the AM layer lines in rigor and plateau of tension states does not constitute a valid approach for the determination of the fraction of interacting myosin heads in contracting muscle.

The formation of the active AM complex requires that the myosin layer lines undergo the *ca.* 1.6 per cent spacing change (Bordas *et al.* 1992). We suggest that a high resolution determination of the relative integrated intensities at 14.34 nm and 14.58 nm may be used to provide a measure for the number of myosin heads interacting with actin providing due account is taken of any change in form factor of the myosin head. From our present observations one cannot determine unequivocally the absolute number of attached heads. However, taking the change in spacing as a sole criterion we deduce that a substantial fraction of the heads have adopted the axial periodicity of the AM complex. This, together with the intensity changes in the equatorial reflections during contraction (Haselgrove and huxley 1973; Matsubara *et al.* 1975; Squire 1981) and an explanation of the spacing change based on model calculations (Bordas *et al.* 1992) leads to the conclusion that at least 70 per cent of the myosin heads may be attached to actin during isometric contraction.

## Conclusions

The structural transitions associated with isometric tension generation were recorded under conditions in which the three-dimensional order characteristic of the rest state was either present or absent. In both cases, new layer lines appear during tension generation, subsequent to changes due to activation events in the thin filaments (for results on activation see Chapter 6.3, this volume). Compared with the 'decorated' actin layer lines of the rigor state, the spacings of the new layer lines are similar whereas their intensities differ significantly. We conclude that in contracting muscle an actomyosin complex

is formed whose structure is not like that in rigor, although it is possible that the interacting sites are the same.

## References


Bordas, J., Diakun, G. P., Harries, J. E., Lewis, R. A., Mant, G. R., Martin-Fernandez, M. L., and Towns-Andrews, E. (1991). Two-dimensional X-ray diffraction of muscle: recent results. *Advances in Biophysics*, **29**, 15–33.

Bordas, J., Diakun, G. P., Diaz, F. G., Harries, J. E., Lewis, R. A., Lowy, J., Mant, G. R., Martin-Fernandez, M. L., and Towns-Andrews, E. (1993). Two-dimensional time-resolved X-ray diffraction studies of isometrically contracting frog sartorius muscle. *Journal of Muscle Research and Cell Motility*, **14**, 311–24.

Haselgrove, J. C. (1975). X-ray evidence for conformational changes in the myosin filaments of vertebrate striated muscle. *Journal of Molecular Biology*, **92**, 113–43.

Haselgrove, J. C. and Huxley H. E. (1973). X-ray evidence for radial cross-bridge movement and for the sliding filament model in actively contracting skeletal muscle. *Journal of Molecular Biology*, **77**, 549–68.

Huxley, H. E. (1969). The mechanism of muscle contraction. *Science*, **164**, 1356–66.

Huxley, H. E. and Brown, W. (1967). The low angle X-ray diffraction diagram of vertebrate striated muscle and its behaviour during contraction and rigor. *Journal of Molecular Biology*, **30**, 383–434.

Huxley, H. E., Faruqi, A. R., Kress, M., Bordas, J., and Koch, M. H. J. (1982). Time-resolved X-ray diffraction studies of the myosin layer-line reflections during muscle contraction. *Journal of Molecular Biology*, **158**, 637–84.

Luther, P. K. and Squire, J. M. (1980). Three-dimensional structure of the vertebrate muscle A-band. II The myosin filament superlattice. *Journal of Molecular Biology*, **141**, 409–39.

Matsubara, I., Yagi, N., and Hashizume, H. (1975). Use of an X-ray television for diffraction of the frog striated muscle. *Nature*, **255**, 728–9.

Rome, E., Offer, G., and Pepe, F. A. (1973*a*). X-ray diffraction of muscle labelled with antibody to C protein. *Nature*, **244**, 152–4.

Rome, E., Hirabayashi, T., and Perry, S. V. (1973*b*). X-ray diffraction of muscle labelled with antibody to troponin C. *Nature*, **244**, 154–5.

Squire, J. M. (1981). In *The structural basis of muscular contraction*. Plenum Press, New York.

Squire, J. and Harford, J. J. (1988). Actin filament organisation and myosin head labelling patterns in vertebrate skeletal muscles in the rigor and weak binding states. *Journal of Muscle Research and Cell Motility*, **9**, 344–58.

Towns-Andrews, E., Berry, A., Bordas, J., Mant, G. R., Murray, P. K., Roberts, K., Sumner, I. L., Worgan, J. S., Lewis, R. A., and Gabriel, A. (1989). Time-resolved X-ray diffraction station: X-ray optics, detectors and data acquisition. *Review of Scientific Instruments*, **60**, 2346–9.

Yagi, N. and Matsubara, I. (1988). Changes in the 5.9 nm actin layer-line on activation of frog skeletal muscles. *Advances in Experimental and Medical Biology*, **226**, 369–80.


# 6.5 Modelling structural changes of the muscle thin filaments during an isometric contraction

*Yutaka Ueno, Noriyoshi Moriwaki, and Katsuzo Wakabayashi*

An intense synchrotron radiation source combined with the use of a high-resolution area detector has provided very nice X-ray diffraction patterns from a contracting skeletal muscle (Amemiya *et al.* 1987), showing the structural changes of muscle proteins responsible for force generation.

X-ray diffraction patterns from a contracting skeletal muscle have shown characteristic intensity changes in the thin filament-based reflections. Our current examination has suggested strongly that these changes are due to the structural changes within the thin filaments that are caused by interaction with the myosin heads (Wakabayashi and Amemiya 1991). Recently, the structure of the G-actin monomer complexed with DNase I has been solved by X-ray crystallography to a resolution of 0.2–0.3 nm (Kabsch *et al.* 1990; Sasaki *et al.* 1992). The modelling studies using the crystallographic data are expected to be useful in deriving the structure from the X-ray fibre pattern when the phase problem has not been solved. A study along these lines has been started for the F-actin structure by Holmes *et al.* (1990). To examine the thin filament changes during contraction of frog skeletal muscle we also begun to analyse the thin filament-based diffraction pattern using the crystallographic data of G-actin. In this chapter we describe our preliminary modelling studies and discuss the structural changes of the thin filament in muscle contraction in terms of possible models.

## Intensity changes of the thin filament-layer lines

Figure 1 shows X-ray diffraction profiles of the thin filament-based layer lines from an isometrically contracting frog skeletal muscle compared with those from the resting state, where troponin reflections are removed. The intensities from the second layer line (1/18.5 $nm^{-1}$) to the first meridional reflection (1/2.7 $nm^{-1}$) increase without any meridional shift of their centroids at all (Wakabayashi *et al.* 1991). The amount of the intensity change varies in different layer lines. Our recent studies showed that the first thin filament layer line (~1/37 $nm^{-1}$; not shown) does decrease in intensity during contraction, and this decrease occurs in a reciprocal manner with the intensity increase of the second layer line (Wakabayashi *et al.* 1991, 1993). Such

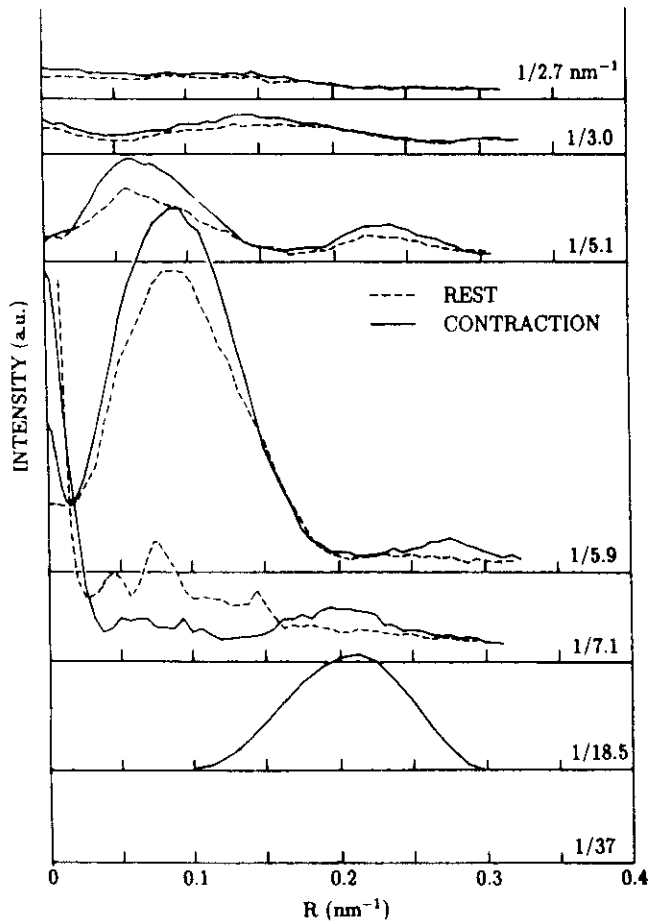


**Fig. 1** Observed intensity distributions of the thin (actin) filament layer lines from frog skeletal (sartorius) muscles. Troponin reflections are removed. The profile of the first layer line (1/37 $nm^{-1}$) has not yet been accurately measured and was omitted. Dashed curve, resting state; solid curve, isometric contraction. Data were derived from the same muscles. The X-ray diffraction patterns were taken using an integrating area detector (an imaging plate) and synchrotron X-rays at the Photon Factory.

intensity changes are quite dissimilar to those taking place when the muscle is put into the rigor state. The distinct intensification of the outer layer lines (≥7.1 nm) occurs in the muscle with an overlap of the thin and thick filaments but not in the overstretched muscle (Wakabayashi *et al.* 1991). The intensity changes of the first and second layer lines occur in the overstretched muscle and are attributed to the change of regulatory proteins, but their



changes (decrease and increase) are smaller than those taking place in the overlap muscle (Wakabayashi *et al.* 1993). Thus the main part of the intensity change of the thin filaments during contraction is caused by interaction with the myosin heads. If significant head binding occurs during force production, its labelling must have an effect on the intensity distribution of the thin filament layer lines. However, careful inspection has revealed that no distinct effect such as mass transfer from the bound heads was observed on any of the layer lines. (Note the existence of the intensity near the meridian on the 7.1-nm layer line.) Although the myosin projections geometrically mark the actin filaments during contraction, the X-ray pattern shows that the actomyosin interaction is taking place in incommensurate periodicities of the thin and thick filaments. Recent quick-freeze electron microscopic studies have revealed that the myosin heads during contraction are interacting with actin along the two-stranded 2/1 helix with a wide range of orientations and shapes in this framework and the marking is not stereospecific (Lenart *et al.* 1993). During contraction, association and dissociation of actin and myosin heads are always repeated on a random basis (Ishijima *et al.* 1991). Probably, the interference between X-rays scattered from the myosin heads and the thin filaments is not strong, so that the intensity changes of the thin filament layer lines during contraction indicate that the thin filament structure is altered over the entire length by random-base interaction with the myosin heads. As mentioned above, the reciprocal intensity change of the first and second layer lines shows that fourfold rotational symmetry becomes more pronounced in the thin filament during contraction. On this basis, we have conducted modelling studies using the atomic coordinates of the G-actin crystal structure to examine the structural change of the thin filaments during force generation.

## Modelling structural changes of the actin–tropomyosin complex

We will consider a model of a thin filament that is composed of actin and tropomyosin, since we are concerned with layer-line intensities which seem to have their main contributions from these molecules (Fig. 1). In modelling, we first assume that the intensities of the outer layer lines (≥7.1 nm) are dominated by the F-actin structure. Using the crystal structure of the G-actin monomer by Kabsch *et al.* (1990), we constructed a model of F-actin to obtain the best fit to these observed intensities. At low resolution analysis (~2.7 nm), only the α-carbon coordinates were used. According to the crystal structure, the actin monomer consists of four subdomains of unequal size and shape, and has a fairly flat structure. We constructed the F-actin structure by arranging this monomer into a filament and the layer-line intensities were calculated by changing parameters, such as orientation, helical coordinate of the monomer, relative position of each subdomain in the monomer, and a scaling weight for the observed data. These parameters have been optimized to fit the observed layer-line intensities by a least-squares procedure. We did

calculations without bias of the model proposed by Holmes *et al.* (1990). It has been possible to derive two F-actin models to fit our observed intensities in the resting state. One (Fig. 2 (a)) is a model very similar to that of Holmes *et al.* apart from slight differences in parameters. (Hereafter it is denoted as an H-model.) The other (Fig. 2 (b)) is a model in which the monomers are arranged with their flat side oriented along a one-start helix of the 5.9-nm pitch. This model may have some resemblance to a model derived by Schutt *et al.* (1989). Although these two possible models gave a similar intensity *R*-factor of 0.22, the main difference between them is in the intensities of the two low-angle layer lines.

We next investigated whether the intensity increase of the outer layer lines observed during contraction could be generated by changing the resting structure. We found that it could be done by altering the domain structure of the monomer. A least-squares fitting procedure has generated a possible active model with a low *R*-factor for the respective resting models. For the moment, we adopt the H-model. In a top view of the H-model (Fig. 3(b)) the movements of subdomains relative to the resting structure are: outward shifts by 0.2 nm and 0.3 nm for subdomains 1 and 3, respectively, and a 0.3 nm inward-up shift for subdomain 2. We did not need extra mass, which might be expected from the attached heads, to achieve such a fit with the observed intensities (see Fig. 4).

We then incorporated tropomyosin molecules into the F-actin models. Tropomyosin was represented as successive spheres of a radius of 0.8 nm, and its weight was determined from the molecular weight ratio relative to the actin monomer. The criterion used for positioning of tropomyosin in the F-actin model is to attain the very weak intensity of the second layer line in the resting state and its significant intensity together with the intensity decrease of the first layer line in the active state. Figure 3 shows a presently possible positioning of tropomyosin for the H-model. We have not yet refined these structures against the X-ray data shown in Fig. 1. In the resting model (Fig. 3 (a)), tropomyosin sits at a radius of 2.8 nm near a cleft between subdomains 1,2 and 3,4 and at an azimuthal position of about 12 degrees from the fibre axis, making contact with the subdomains 1, 3, and 4. In the active model (Fig. 3(b)), it shifts outward slightly (~0.3 nm) and azimuthally further by about 17 degrees, making contact with the subdomains 3 and 4. This

**Fig. 2** Two possible models of the F-actin filaments derived from the rigid body transformation of the α carbon coordinates of the G-actin structure by Kabsch *et al.* (1990). (a) A model similar to that of Holmes *et al.* (1990). (b) A model in which actin monomers are placed with their flat side oriented along a one-start helix of the 5.9-nm pitch. Upper, a side view; lower, a top view. Boundary of the monomer in the filament is contoured by white lines. In one monomer: subdomain 1, white; subdomain 2, light grey; subdomain 3, medium grey; subdomain 4, dark grey. (The numbering of subdomains follows Kabsch *et al.* (1990).)



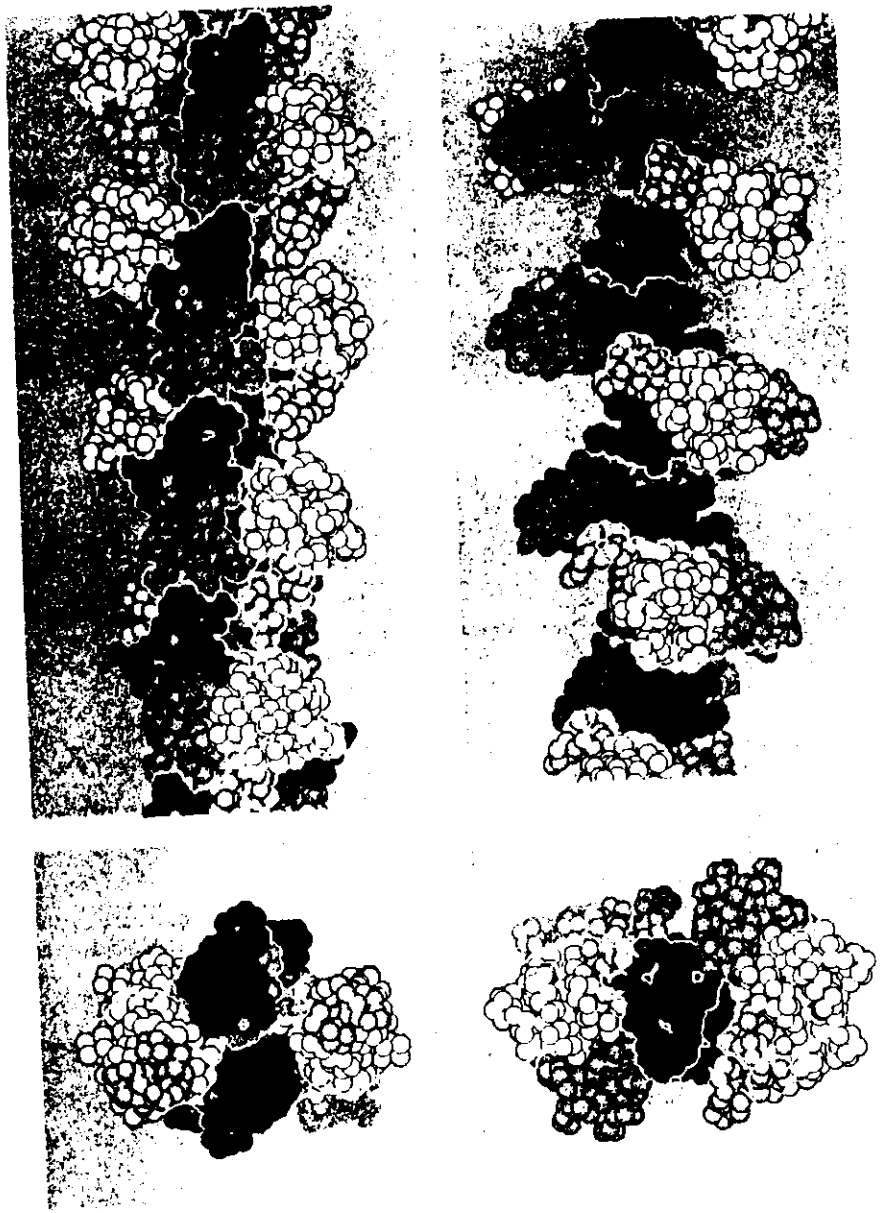

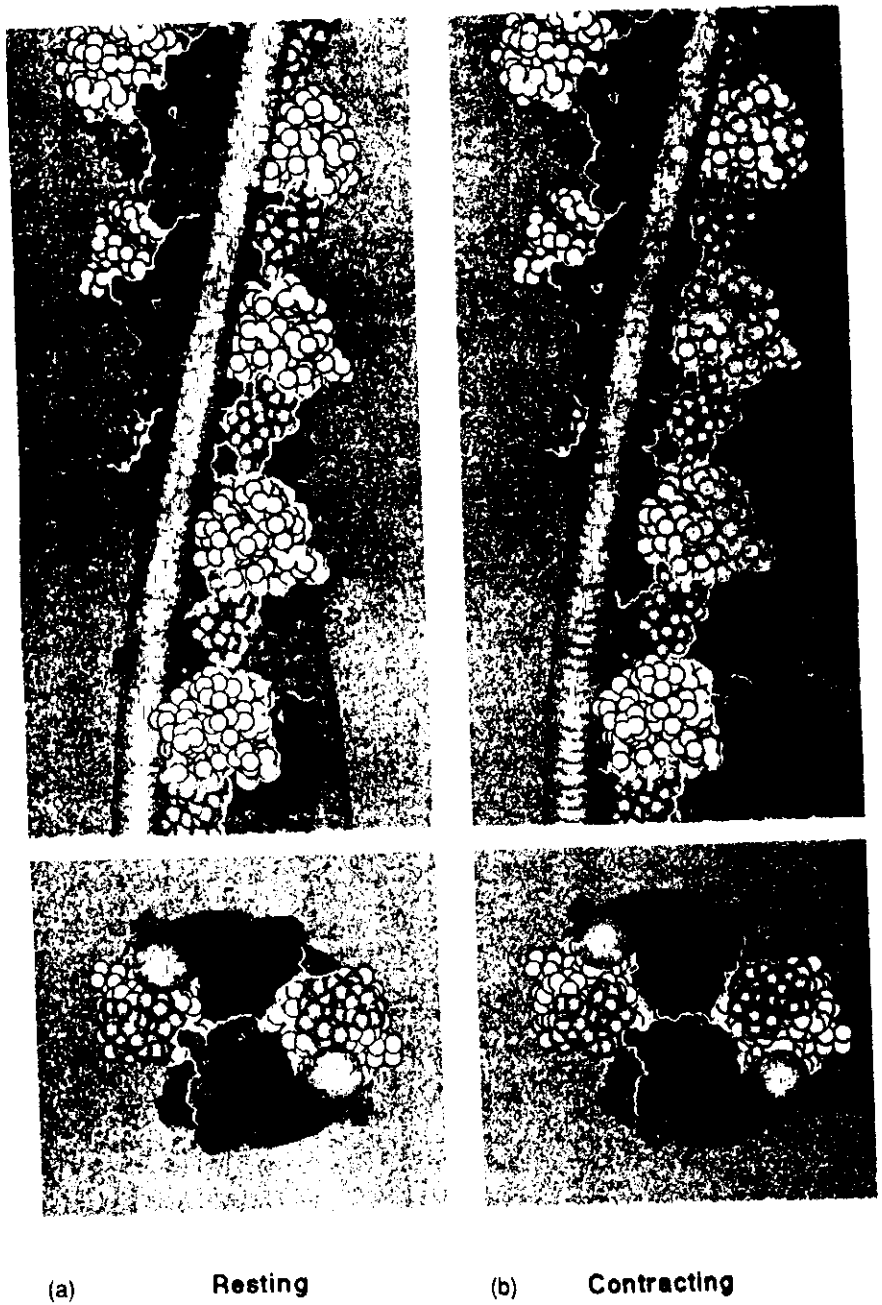


**Fig. 3** Preliminary models of the actin–tropomyosin complex. The F-actin model is the same as in Fig. 2(a). Two ropes represent tropomyosin molecules. (a) A



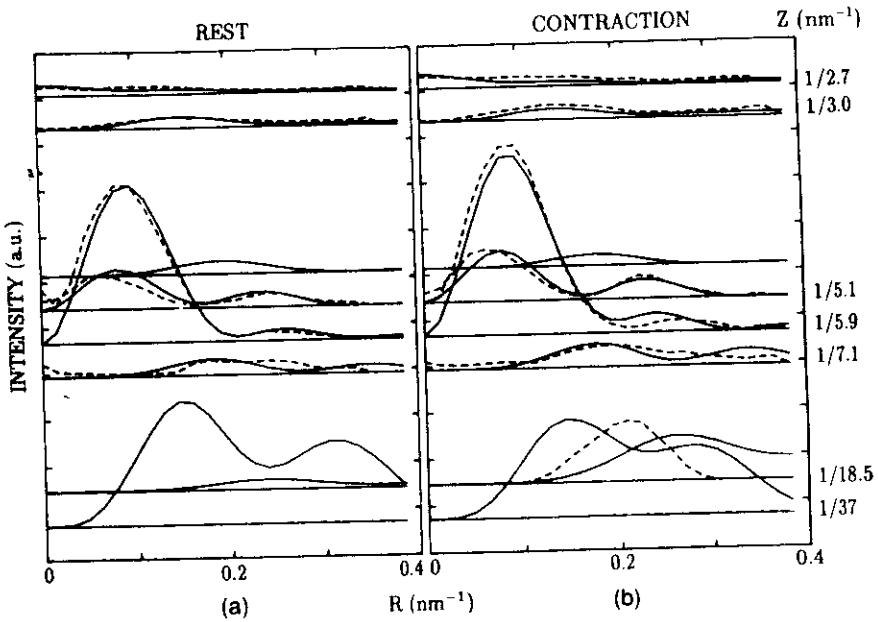


**Fig. 4** Comparisons between the calculated and observed layer-line intensities. (a) Resting state; (b) active state. Solid curves represent calculated intensities from the model of Fig. 3. The dashed curve represents observed intensities from Fig. 1.

position for tropomyosin has been found in a reconstruction of the decorated thin filaments (Milligan *et al.* 1990). Figure 4 shows the comparison between the calculated (from models in Fig. 3) and observed intensities in the resting and active states. Fitting for the second layer line is not good but it could be overcome by further refinement for the tropomyosin positioning. Unfortunately, we have not been able to accurately derive the profile of the first layer line for various reasons described elsewhere (Wakabayashi *et al.* 1993). Thus, in the present analysis, the fitting of the first layer line was not made. Figure 3(b) shows that in the active state the structural deviation of the filament from its axial average increases due to a change in the domain structure of the actin monomer. Our modelling studies suggest that, on activation, the large tropomyosin movement could be caused by an alteration of the actin structure if tropomyosin makes contact to the subdomain 3. The thin filament structure enhances the fourfold rotational symmetry contribution to the structure due to a change in the internal structure of the monomer and the associated movement of tropomyosin in the active state.

## Concluding remarks

The feature of changes in intensities of the thin filament-based layer lines in the X-ray diffraction pattern from an isometrically contracting frog skeletal

muscle was described. We have attempted to explain these characteristic intensity changes in terms of the structural changes of the actin–tropomyosin complex caused by interaction with the myosin heads. Possible structural changes of the complex were shown by modelling using the atomic coordinates of the G-actin crystal structure by Kabsch *et al.* (1990). Modelling studies imply that the actin structure is altered, being responsible for tropomyosin movement.

## Aknowledgements

We are indebted to Drs H. Tanaka, T. Kobayashi, and H. Iwamoto for X-ray diffraction work and to Mr H. Saito for data treatment. We acknowledge Dr W. Kabsch and Professor K. C. Holmes for use of the atomic coordinates of the G-actin crystal structure.

## References

Amemiya, Y., Wakabayashi, K., Tanaka, H., Ueno, Y., and Miyahara, J. (1987). Laser-stimulated luminescence used to measure x-ray diffraction of a contracting striated muscle. *Science*, **237**, 164–8.

Holmes, K. C., Popp, D., Gebhard, W., and Kabsch, W. (1990). Atomic model of the actin filament. *Nature*, **347**, 44–9.

Ishijima, A., Doi, T., Sakurada, K., and Yanagida, T. (1991). Sub-piconewton force fluctuations of actomyosin in vitro. *Nature*, **352**, 301–16.

Kabsch, W., Mannherz, H. G., Suck, D., Pai, E. F., and Holmes, K. C. (1990). Atomic structure of the actin:DNase I complex. *Nature*, **347**, 37–44.

Lenart, T. D., Allen, T. St., Barsotti, R. J., Ellis-Davies, G. C. R., Kaplan, J. H., Franzini-Armstrong, C., and Goldman, Y. E. (1993). Mechanical and structural characteristics of cross-bridges following activation of frog muscle fibres by photolysis of caged $Ca^{2+}$. *Advances in Experimental Medicine and Biology*, (In press).

Milligan, R. A., Whitakker, M., and Safer, D. (1990). Molecular structure of F-actin and location of surface binding sites. *Nature*, **348**, 217–21.

Sasaki, K., Sakabe, K., Sakabe, N., Kondoh, H., and Shimomura, M. (1992). Crystal structure of smooth muscle actin DNase I complex at 2Å resolution. Abstracts of the 4th International Conference on Biophysics and Synchrotron Radiation, Tsukuba, p. 29.

Schutt, C. E., Uno, L., Myslik, J., and Strauss, N. (1989). Molecular packing in profilin:actin crystals and its implications. *Journal of Molecular Biology*, **209**, 735–46.

Wakabayashi, K. and Amemiya, Y. (1991). Progress in x-ray synchrotron diffraction studies of muscle contraction. In *Handbook on synchrotron radiation*, Vol. 4 (ed. S. Ebashi, M. Koch, and E. Rubenstein), pp. 597–678. Elsevier, Amsterdam.

Wakabayashi, K., Tanaka, H., Saito, H., Moriwaki, N., Ueno, Y., and Amemiya, Y. (1991). Dynamic x-ray diffraction of skeletal muscle contraction: Structural change of actin filaments. *Advances in Biophysics*, **27**, 3–13.

Wakabayashi, K., Saito, H., Moriwaki, N., Kobayashi, T., and Tanaka, H. (1993). The first thin filament layer line decreases in intensity during an isometric contraction of frog skeletal muscle. *Advances in Experimental Medicine and Biology*, (In press).

# 6.6 Synchrotron radiation in time-resolved X-ray diffraction studies of molecular movements in muscle

*John M. Squire, Jeffrey J. Harford, and Hind Alkhayat*

Because of the enormous X-ray fluxes in low-angle diffraction beamlines on synchrotron sources, fast time-resolved X-ray diffraction studies of dynamic events in biological systems such as muscle (Fig. 1) are uniquely informative (Huxley *et al.* 1980; Wakabayashi *et al.* 1988; Irving *et al.* 1992; Harford and Squire 1990, 1992). Two-dimensional diffraction patterns from activated whole muscles can be recorded satisfactorily at 5-ms time resolution to a spatial resolution of about 27 Å axially and 70 Å radially. In addition, the effects of microsecond mechanical interventions on single fibres have been monitored with about 200-μs time resolution (Irving *et al.* 1992). The main problem with all such diffraction studies is that only intensity information is recorded, but phase information is also needed in order to interpret the changes in the diffraction patterns that are observed. Interpretation of muscle diffraction patterns has proved to be the main hurdle to overcome in order to make full use of time-resolved X-ray diffraction information. This chapter therefore addresses the problem of how the muscle phase problem is being overcome. It is a summary of work in progress—the final structure determination is not yet complete.

## Bony fish muscle

In this research group, after early studies of frog muscle (Squire 1975; Luther and Squire 1980), we are now exploiting the high degree of order in bony fish muscle which gives this preparation unique advantages in 'solving' the molecular arrangements in the muscle (Harford *et al.* 1988). One of the historic problems with X-ray diffraction patterns from most vertebrate muscle types, despite the enormous technical progress that has been made, is that the patterns are only partially sampled. For example, within the A-bands (Fig. 1) of frog muscles and muscles of most other vertebrates apart from bony fish, the myosin filaments are arranged on a hexagonal lattice but with a statistical distribution of filament orientations on the lattice points. There is no regular unit cell; the nearest thing to it is a statistical superlattice (Luther and Squire 1980). This means that the observed diffraction patterns, especially the parts arising from the quasi-helical arrangement on the myosin filament surfaces of

# 4. Synchrotron radiation and chain molecules

- flux, but radiation damage is possible
- SAXS, because sometimes large periodicities
- micro-analysis, because sometimes not homogeneous
- time-resolved

# IV LIPIDS

## 1- Overview

- Small molecules
- hydrophilic head
  hydrophobic chains

- bilayer systems

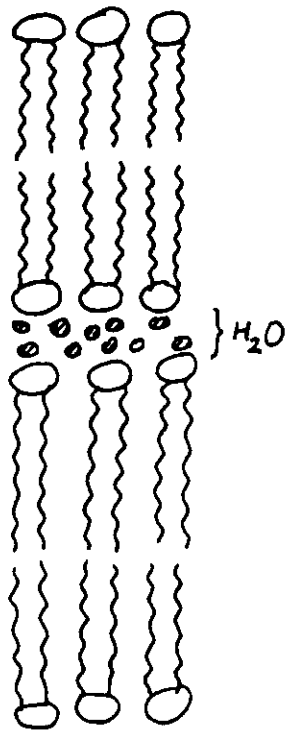


- chemical barrier
  (membranes)

# Scattering by lipids

It is usual to distinguish between the reflections due to the lamellar order from the reflections due to the order within a lamellae.

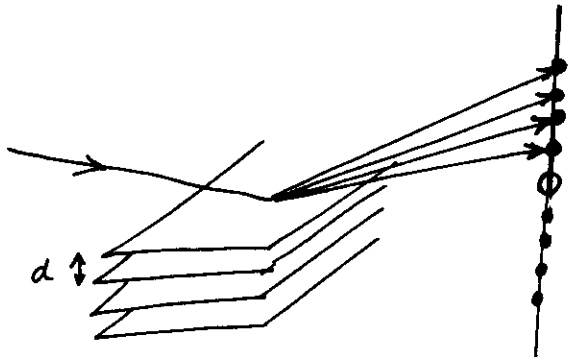


various harmonics n/d along the meridian

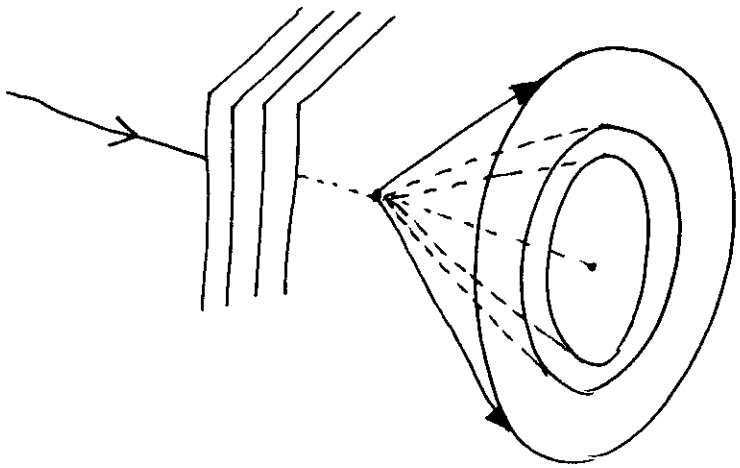

various rings if crystallized within the layers. Gives the order within the layers

Order within the layers
- crystalline (hexagonal or pseudo-hexagonal)
- liquid
- liquid crystalline

TARDIEU A, DELAYE M., 1988 - Eye lens proteins and transparency: from light transmission theory to solution X-ray structural analysis - Ann Rev Biophys Biophys Chem 17, 47-70

TARDIEU A., VACHETTE P., GULIK A., le MAIRE M., 1981 - Biological macromolecules in solvents of variable density : characterization by sedimentation equilibrium, densimetry and X-ray forward scattering - Biochemistry 20, 4399-4406

## REFERENCES

BENEDEK, G. B., 1971 - Theory of transparency of the eye - Appl. Opt. 10:459-473.

CARNAHAN N.F. & STARLING K.E., 1969 - Equation of state for non attracting rigid spheres - J. Chem. Phys. 51, 635-636

DELAYE M, TARDIEU A, 1983 - Short range order of crystallin protein accounts for eye lens transparency - Nature (London) 302, 415-417

HANSEN J.P. & HAYTER J.B., 1982 - A rescaled MSA structure factor for dilute charged colloidal dispersions - Mol. Phys. 42, 651-656

HAYTER, J. B. & PENFOLD, J., 1981 - An analytic structure factor for macroion solutions - Molec. Phys., 42, 109-118

KINSEY V.E. & REDDY D.V.N., 1965 - Studies of the crystallin lens. XI The relative role of the epithelium and the capsule in transport - Invest. Ophthalm. 4, 104-121

KORETZ J.F., 1988 - How the human lens focuses - Scientific American, 259: 64-71

PARSEGIAN V.A., RAND R.P. FULLER N.L. & RAU D.C., 1986 - Osmotic stress for the direct measurement of intramolecular forces- Methods Enzymol. 127, 400-416

PIATIGORSKY J., 1984 - Lens crystallin and their gene families - Cell 38, 620-621

PROUTY M. S., SCHECHTER, A. N., and PARSEGIAN, V. A., 1985 - Chemical potential measurements of deoxyhemoglobin S polymerization: Determination of the phase diagram of an assembling protein- J. Mol. Biol. 184, 517-528.

TROKEL, S., L., 1962 - The physical basis for transparency of the crystalline lens - Invest. Ophthalmol., 1, 493-501.

VERETOUT F., DELAYE M. & TARDIEU A., 1989 - The molecular basis of eye lens transparency: osmotic pressure and x-ray analysis ( f alpha-crystallin solutions - J Mol Biol 205: 713-728

VERETOUT F. & TARDIEU A., 1989 - The protein concentration gradient within eye lens might originate from constant osmotic pressure coupled to differential interactive properties of crystallins - Eur. Biophys. J. 17, 61-68



# CHAPTER X

# DIFFRACTION EXPERIMENTS ON LIPID BILAYERS AND BIOLOGICAL MEMBRANES

G. BÜLDT

Biological membranes are the barriers in cells and organelles against the outside medium. The two major components of membranes are lipids and proteins. Lipids are amphiphilic molecules, which in aqueous media spontaneously form double layered structures. The amphiphilic character of the lipids with polar headgroups and apolar hydrocarbon chains is responsible for the two-dimensional geometry of biological membranes. Integral membrane proteins, which span the lipid bilayer, mediate the transport of matter and signals. Soluble proteins can be associated with one side of a membrane through a lipid anchor covalently bound to the protein. A membrane can also contain protein anchors for filamentous structures, which mechanically stabilize the cell.

The first part of this lecture describes X-ray and neutron diffraction experiments on pure lipid bilayer systems, whereas the second part presents experiments concerning the structure and dynamics of membrane proteins. Scattering experiments on biological membranes or on pure lipid bilayer systems are normally carried out on aggregates like single shell vesicles or multibilayer systems. Diffraction experiments on membranes have two levels in the degree of difficulty. Recording diffraction patterns and simply measuring positions of diffraction peaks provide geometrical information on bilayer systems like the thickness of membranes, packing of lipid chains, secondary structure of membrane proteins, and membrane protein packing. Any nonspecialist can collect this information without spending too much effort. Measuring integrated intensities of diffraction peaks, solving the phase problem, and calculating density maps in order to solve structures is much more complicated.

## X.1. Pure lipid bilayers

Although, in a biological membrane, proteins modify the interactions between membranes as well as between membrane components, it is the amphiphilic architecture of a lipid molecule, which is responsible for its geometric arrangement in the form of bilayers. In addition, the inherent ability of most lipids to take up a large number of conformations and their segmental mobility leads them to form an excellent two-dimensional solvent for membrane proteins. Therefore, to have a clear understanding of the forces which are responsible for the various lipid and bilayer properties, an investigation of pure lipid bilayer systems is necessary. X-ray and neutron diffraction are the most powerful tools in characterizing lipid and bilayer morphology and to follow up their changes due to alterations in the number of components and their concentrations. It should be noted that ions and other molecules in the water phase adjacent to the bilayer

surface influence the physical state of membranes and should therefore be considered as components of the bilayer.

As a nicely written introductory article for the diffraction methods applied to bilayer systems, a paper of Franks and Lieb (1981) is recommended.

### X.1.1. Diffraction experiments on oriented films of multilamellar stacks of bilayers

With respect to the basic principles of a diffraction experiment, there is no large difference between neutrons and X-rays. As the flux of neutron sources is several orders of magnitude smaller than for X-rays, the sample volume in a neutron diffraction experiment is typically of the order of 10 x 20 x 1 $mm^3$ and therefore much larger than in the X-ray case. In the paragraphs (X.1.1 and 1.2), which are introductory, the experiments described are carried out with X-rays. The same type of experiments can be done with neutrons, after modifying the instrumentation with respect to beam size, scattering volume and detectors.

In a first experiment, a sonicated dispersion of 4 mg of the lipid 1,3-DPPC (1,3-dipalmitoyl-glycero-2-phosphocholine) in 0.2 ml $H_2O$ is spread on a glass slide and allowed to evaporate slowly. After evaporation of the bulk water a multibilayer film is formed with predominent orientation parallel to the bilayer surface. The slide with the lipid film is aligned in an X-ray beam which hits the film tangentially (Figure X.1.A.). In quantitative experiments the sample should be controlled with respect to temperature and relative humidity which is achieved by a sample chamber with windows transparent for the X-ray beam.

In Figure X.1.B. three diffraction patterns of the same 1,3-DPPC lipid film are shown. The equidistant intensity spots on the meridian of the X-ray film prove that we have a one-dimensional periodicity along the direction perpendicular to the lipid film.

From Bragg's law $|G|=|s|$, with $|G|=\frac{h}{d}$ and $|s|=\frac{2}{\lambda}\sin(\theta)$

we obtain $$\frac{h}{d}=\frac{2}{\lambda}\sin(\theta) \qquad \text{with } h = 1, 2, 3, \ldots .$$

where d is the repeat distance of the one-dimensional lattice, which is the thickness of the lipid bilayer plus the water layer. Bragg angle $\theta$ is calculated (see Figure X.1.A.) by $\mathrm{tg}\,2\theta = \ell/L$.

The diffraction spots in Figure X.1.B.a. are extended arcs. The intensity distribution over an arc is directly proportional to the number of domains in the lipid film with different orientations relative to the glass slide. The angular distribution of all domains in the sample is called the **mosaic spread**, which in (a) is of the order of 25° FWHM (full width at half maximum). The mosaic spread for this lipid film can be reduced by an annealing procedure, in heating up the sample to 110°C for 4h and then cooling it down slowly (Büldt et al., 1979). The procedure results in an enhanced intensity of diffraction orders in this case by a factor of 20 as seen in (b). The diffraction patterns (a) and (b) were collected at 22°C, where DPPC is in the so called gel phase, which is characterized by hydrocarbon chains in all-*trans* conformation. When the temperature is raised to



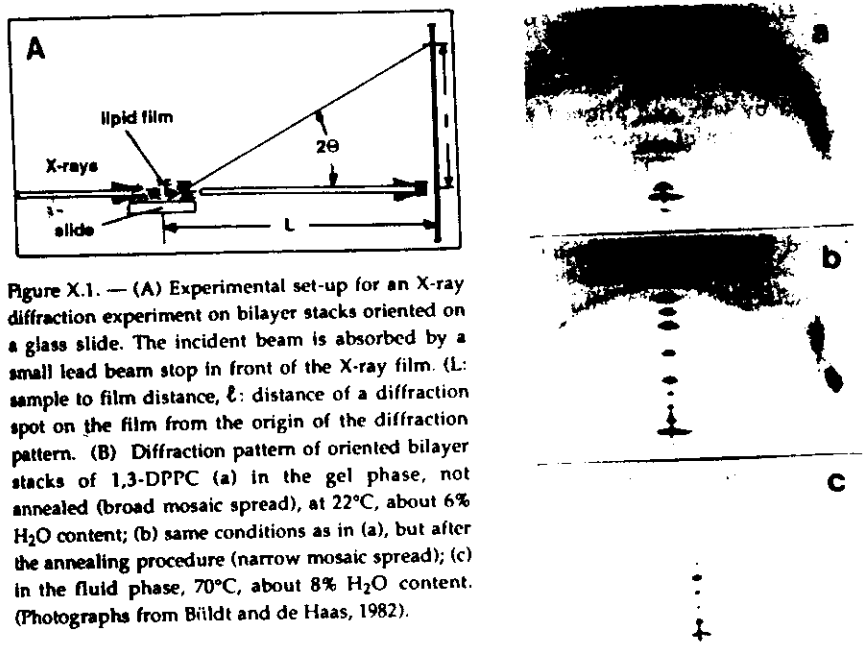


Figure X.1. — (A) Experimental set-up for an X-ray diffraction experiment on bilayer stacks oriented on a glass slide. The incident beam is absorbed by a small lead beam stop in front of the X-ray film. (L: sample to film distance, $\ell$: distance of a diffraction spot on the film from the origin of the diffraction pattern. (B) Diffraction pattern of oriented bilayer stacks of 1,3-DPPC (a) in the gel phase, not annealed (broad mosaic spread), at 22°C, about 6% $H_2O$ content; (b) same conditions as in (a), but after the annealing procedure (narrow mosaic spread); (c) in the fluid phase, 70°C, about 8% $H_2O$ content. (Photographs from Büldt and de Haas, 1982).

70°C, i.e., above the first order phase transition temperature of DPPC, the sample is in the fluid phase with hydrocarbon chains forming *gauche+* and *gauche-* conformations which result from rotations around C-C bonds by + or - 120° degrees. The diffraction pattern of the fluid phase is shown in (c). The Bragg peaks are further apart, which means that the bilayer plus water layer becomes smaller. This is the result of a reduction in the thickness of the hydrocarbon chains due to segmental disorder. We also observe a decrease in intensity which is quite dramatic for diffraction spots greater than h = 6. This is caused by the Debye-Waller factor, which is a Gaussian function centered on s = 0 $Å^{-1}$ with a width depending on the disorder and motion of lipid segments in the bilayer.

Off-axis to the equator at 1/s = 4.2 Å one single reflection spot is visible in (a, b). This reflection originates from the packing of hydrocarbon chains. If we assume an hexagonal arrangement, the observed reflections can be indexed by h,k=1,0. Using Bragg's law

$$\frac{2}{\sqrt{3}a}\sqrt{h^2+hk+k^2}=\frac{2}{\lambda}\sin(\theta)$$

the lattice constant a, which is the distance between two neighboring chains, is determined to be a = 4.85 Å. The off-axis position of the chain-packing reflection is caused by a tilt of hydrocarbon chains with respect to the bilayer normal (Tardieu et al., 1973). This reflection becomes more pronounced at smaller mosaic spread (b) and is very weak in the fluid phase. The increase of disorder in this phase causes a broadening and a shift of the chain reflection from 4.2 Å to 4.5 Å.

### X.1.2. Diffraction experiments on powders of multilamellar stacks of bilayers

For sample preparation 7.5 mg of DPPC is mixed with 2.5 mg $H_2O$ and filled in a glass capillary of 1 mm diameter with 0.01 mm wall thickness. The capillary is closed by wax and aligned perpendicular to an X-ray beam. The X-ray film shows a pattern of concentric equidistant rings centered around the origin of the diffraction pattern. The ring system originates from the diffraction of multilamellar bilayer stacks in the powder. The chain packing gives a ring at 4.2 Å. The lamellar reflections in the diffraction pattern of the fluid phase, which can be obtained by heating the capillary with hot air, are shifted away from the center which means that the thickness of the bilayer plus water became smaller. The chain reflection is broadend and shifted to 4.5 Å, as observed for the oriented sample.

### X.1.3. The conformation of a phospholipid molecule in a bilayer as studied by neutron diffraction

In the previous sections, we have derived geometrical information on bilayer systems. In this paragraph it will be shown how coordinates of certain segments in a lipid molecule in the bilayer are obtained, applying methods of one-dimensional crystallography to the one-dimensional periodicity of multilamellar stacks of bilayers. Structure factors, derived from lamellar diffraction spots, give only profile information of the bilayer which is the projection of density on the bilayer normal. With X-ray diffraction it is not possible to see positions of certain segments in the bilayer profile in the gel or fluid phase. The fluctuations of individual segments along the bilayer normal are quite large and overlapping with neighbouring segments occurs, so that the determination of the average position of a segment is impossible. This problem was solved by neutron diffraction in combination with selective deuteration of a molecular group, thus enhancing the local contrast. In this way the average position and the extent of fluctuations of a segment were determined from a difference of two density maps with and without the deuterated group. In general, one great advantage for the application of neutrons over X-rays to biological structures is the possibility of contrast enhancement by isotope exchange which normally is a very small disturbance to the structure. For biological material in most cases the difference in coherent scattering length between hydrogen ($b = -0.374 \cdot 10^{-12}$ cm) and deuterium ($b = +6.67 \cdot 10^{-12}$ cm) is used. A neutron diffraction experiment on an oriented lipid film is performed in a similar way to an X-ray experiment. However, the area of the lipid film in a neutron diffraction experiment has to be quite large (about 25x50 $mm^2$). The diffraction pattern of such a film is shown in Figure X.2..

Experimental details are given in the figure legend. The differences in relative height of the diffraction orders demonstrate the sensitivity of the method with respect to label positions, e.g., the change in label position to a neighbouring segment leads already to a remarkable change in relative intensities (Figure X.2.). From integrated intensities of diffraction spots the absolute values of structure factors are derived. Since pure lipid bilayers are centrosymmetric, the phase problem reduces to a distinction between phase angle 0 or π. This problem can be solved for the lower order reflections by $H_2O/D_2O$ exchange experiments using the water layer between membranes as an isomorphous replacement site.



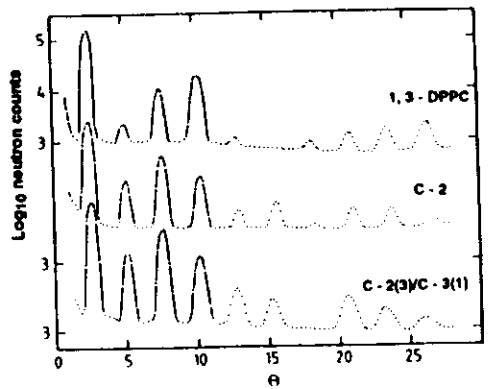


Figure X.2. — Log plots of neutron counts versus Bragg angle (θ) for 1,3-DPPC in $H_2O$ measured on the diffractometer D16 at the ILL Grenoble ($\lambda = 4.5$ Å): The upper plot: non-deuterated 1,3-DPPC; the pattern in the middle: 1,3-DPPC$_3$-deuterated at the first methylene segment or at the second carbon atom (C-2) in both chains; the third plot: the same lipid, deuterated at the second carbon atom in chain 3 (C-2(3)) and at the third carbon atom in chain 1 (C-3(1)). All three patterns are taken in the gel phase at 20°C and 6% $H_2O$ content, lamellar spacing 52.2 Å. (From Büldt and deHaas, 1982).

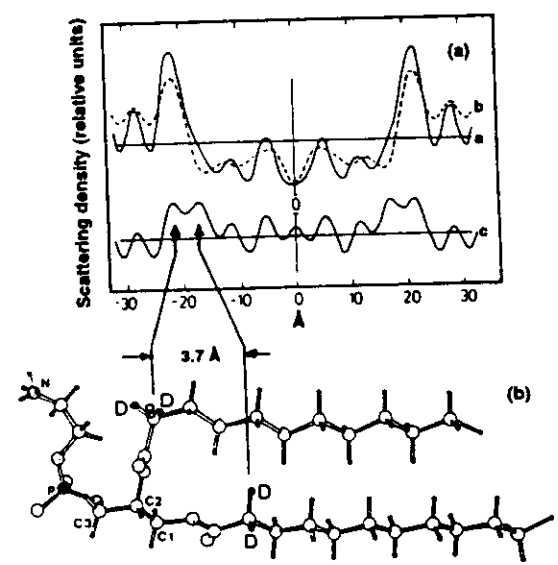


Figure X.3. — (A) Neutron scattering length density profiles calculated from 10 structure factors of (a) DPPE deuterated at the C-2 position, (b) of the non-deuterated sample, and (c) the difference of these profiles. (Plot from Büldt and Seelig, 1980, with permission).

(B) Molecular model of a phospholipid in a bilayer according to the distance of the first methylene segments in both hydrocarbon chains.

Figure X.3.A. shows the profile of DPPE (1,2-dipalmitoyl-*sn*-glycero-3-phosphoethanolamine) selectively deuterated in the first methylene segments of both chains together with the profile of the non-deuterated DPPE. The resulting difference profile (lower trace) shows two peaks at position 17.4 Å and 21.1 Å.

Although the profile is quite noisy, the numbers can be determined very accurately from a refinement procedure on the structure factors. The main result of this profile is that the first methylene segments in both hydrocarbon chains are shifted with respect to each other by 3.7 Å along the bilayer normal (Büldt and Seelig, 1980).

The consequence of this experimental finding on the molecular model of a phospholipid is illustrated in Figure X.3.B.. The glycerol backbone is oriented perpendicular to the membrane plane with the sn-1 chain following this direction whereas the sn-2 chain becomes parallel to sn-1 after a sharp bent. Using Deuterium Magnetic Resonance this conformation was shown to be general for all phospholipids in all phases and membranes (Seelig and Seelig, 1980), and even in its crystal structure where it was first discovered (Hitchcock et al., 1974).

## X.2. Membrane proteins

There exists a wide range of methodical approaches for the investigation of membrane proteins with neutrons or X-ray synchrotron radiation. A number of membrane proteins have now been crystallised but only two fundamentally different structures have been solved to high resolution by X-ray crystallography (Deisenhofer et al., 1985; Weiss et al., 1991). In this paragraph we restrict ourselves to a few examples of diffraction studies on stacks of so called "Purple Membranes" (PM) which are part of the cell membrane of *Halobacterium halobium*.

The integral membrane protein bacteriorhodopsin (BR) is the sole protein in the purple membrane and acts as a light-driven proton pump. Although many attempts have been made (Michel, 1982), up to now the formation of well-diffracting 3-dimensional crystals of BR has been unsuccessful. Numerous structural and spectroscopic methods have been applied to this protein, in order to obtain various pieces of information, which together form a now nearly complete mosaic of the structure-function relationship. Diffraction methods as well as electron microscopy studies on this protein benefitted from its aggregation into two-dimensional hexagonal crystals (purple membranes) in the cell membrane of these bacteria. The unit cell contains a trimer of BR (26500 Da) and 21 to 27 lipids. The purple colour reflects the interaction of the chromophore retinal in the protein pocket of BR. It is the absorption of a photon by the chromophore followed by a sequence of isomerisation steps which are coupled to the translocation of one proton across one BR molecule, per functional cycle (Grzesiek and Dencher, 1986).

The characterization of the aggregation state of BR in the membrane, as well as the amount and orientation of its secondary structure was given by X-ray diffraction methods (Blaurock, 1975; Henderson, 1975). The basic picture of the tertiary structure, describing the three-dimensional arrangement of α-helices spanning the membrane, was given in several papers on low dose electron microscopy (e.g., Unwin and Henderson, 1975; Henderson and Unwin, 1975).

The knowledge of the amino-acid sequence (Ovchinnikov et al., 1979) allowed the prediction of a folding model by determining seven α-helical stretches in the polypeptide chain which were assigned to the seven α-helices seen in the electron microscopical structure (Engelman et al., 1980). In the following years neutron diffraction was the method of choice to prove this model using BR molecules containing certain perdeuterated amino acids (Engelman and Zaccai, 1980; Trewhella et al., 1983) and partially deuterated α-helices (Trewhella et al.,1986; Popot et al., 1989). This technique was also successful in the localization of perdeuterated or partially deuterated retinal within the protein (Jubb et al., 1984; Heyn et al.,1988). Heavy-atom labelled retinal analogues incorporated into the protein confirmed these results by X-ray diffraction (Büldt et al., 1991). In early neutron diffraction experiments the hydration of purple membranes was studied (Zaccai and Gilmore, 1979) and more recently the location of the proton channel in BR was determined by neutron diffraction in combination with $H_2O/D_2O$ exchange experiments (Papadopoulos et al., 1990).

In 1990, cryo-electron microscopy provided an additional breakthrough providing a structure of BR at 3.5 Å resolution in the X-Y plane and 7 Å in the Z-direction. These pictures allowed for the first time, including all the information from other methods mentioned above, to construct a molecular model of BR (Henderson et al., 1990).

The examples given in paragraph X.2.2. and X.2.3. will demonstrate that diffraction by neutrons and X-rays give complementary information which is not obtained from cryo-electron microscopy.

### X.2.1. Diffraction experiments on oriented films of two-dimensional protein crystals

This section gives an introduction to diffraction experiments on the two-dimensional hexagonal lattices of BR. Figure X.4. illustrates in (A) a two-dimensional protein latice in real space and its counterpart in reciprocal space. The h,k-plane, which corresponds to the plane of two-dimensional periodicity in real space, has a distinct intensity distribution at reciprocal lattice points. Perpendicular to these points in the l-direction continuous intensity distributions, the so called Bragg rods, are obtained which correspond to the direction with no periodicity in real space. This is the situation for electron diffraction in the electron microscope where a diffraction pattern from a single protein lattice can be recorded (Henderson and Unwin, 1975), since the interaction of an electron with matter is much larger than for X-rays or neutrons. The latter case is illustrated in (B), where several millions of lattices form a film of purple membranes. In this film, lattices have small but different angles to the supporting surface which determines the mosaic spread as in the case of oriented pure lipid bilayers. Within each stack, lattices are randomly oriented to each other with respect to an axis perpendicular to the membrane plane. The corresponding reciprocal lattices are also randomly oriented with respect to the l-axis and form a system of concentric cylinders, which have a continuous intensity distribution in the l-direction. Only the Bragg rod at h,k = 0,0, which is on the l-axis, is the Fourier transform of the projected density of the membranes (the profile) and is therefore periodic showing distinct intensity spots. In scattering geometry (i), where the incident beam runs parallel to the purple membranes, "Ewald's sphere" or "the sphere of reflection" intersects reciprocal space tangentially to the l-axis at the origin. The intersection picture is shown on the X-ray film with the lamellar spots on the meridian and the intersection lines of Ewald's sphere with the concentric cylinders on the equator. In configuration

(ii), with the incident beam perpendicular to purple membranes, Ewald's sphere intersects the reciprocal space tangentially to the h,k-plane at the origin, resulting in concentric rings on the X-ray film.

### X.2.2. The location of the chromophore retinal in bacteriorhodopsin by neutron diffraction

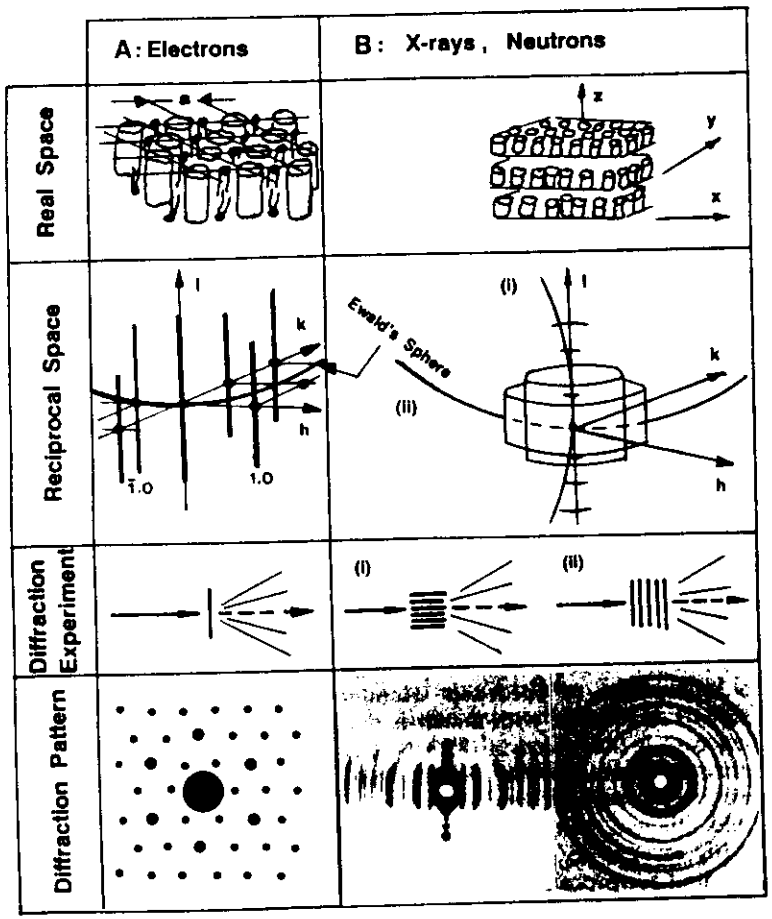


Figure X.4. — (A) Density in real space and intensity distribution in reciprocal space of a single protein lattice and an electron diffraction experiment.

(B) Intensity distribution of a stack of lattices randomly oriented with respect to Z-axis. X-ray films show diffraction pattern for stacks of purple membranes in two different scattering geometries (i) and (ii).



A nice example of the enhancement of local contrast by selective deuteration is the localization of the chromophore retinal in bacteriorhodopsin by neutron diffraction. The first successful solution of this problem was done by *in vivo* incorporation of perdeuterated retinal into BR by Jubb et al. (1984). Figure X.5.A. shows diffraction peaks in the radial direction of rings as illustrated in Figure X.4. (B, ii). The neutron wavelength used was 4.5 Å and therefore much higher than the copper $K_\alpha$-line of 1.5 Å in X-ray experiments. Therefore, to insure that the scattering vector **s** is always parallel to the membrane plane a so called $\theta$-$2\theta$ scan was performed, where the sample aligned on the $\omega$-axis of the diffractometer is rotated by $\theta$ and the detector by $2\theta$. At detector angle $2\theta = 0$ purple membranes were oriented perpendicular to the incident neutron beam.

Figure X.5.A. shows two diffraction patterns for purple membrane films with deuterated and non-deuterated retinal. The integrated intensity was obtained for each reflection after substraction of background and multiplication of a Lorentz factor. As seen in the previous section rotation of Bragg rods around the l-axis leads to a superposition of reflections with the same value in $h^2+hk+k^2$, e.g. $I(h^2+hk+k^2)$ = const. was split between the (h,k) and (k,h). Therefore the intensity I(h,k), I(k,h) etc., according to their ratio in electron diffraction (Henderson and Unwin, 1975). Phase angles determined by electron microscopy were used. Figure X.5.B. shows the resulting difference Fourier map. The highest contour line depicts the location of the center of mass of deuterons in the retinal.

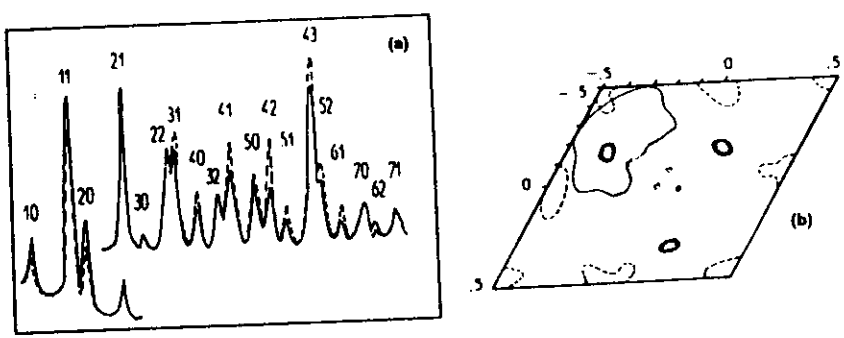


Figure X.5. — (a). Neutron diffraction pattern of an oriented purple membrane film. Dashed line: sample with non-deuterated retinal, full line: sample with perdeuterated retinal.
(b). Difference Fourier map: highest positive bold contour lines show the center of mass of the deuterated retinal, the thin line marks the protein area. (Photographs from Jubb et al., 1984, with permission).

In the following years, these experiments were extended and refined using retinals which were partially deuterated at three different positions within the chromophore (Heyn et al., 1988). With these retinals the orientation of the chromophore within the unit cell was determined in projection on to the plane of the membrane as well as in the profile from lamellar diffraction (Hauß et al., 1990).

Heavy atom labelled retinals in PM used in X-ray diffraction experiments confirmed these results (Büldt et al., 1991). The heavy atom labelled retinals are now used in EXAFS-experiments to explore the fine structure of the retinal binding pocket in BR for different intermediate states of the photocycle.

### X.2.3. Conformational changes in bacteriorhodopsin during the photocycle as seen by neutron and time-resolved X-ray diffraction

Bacteriorhodopsin translocates protons over the membrane in a cyclic way using the energy of light. The ground state $BR_{568}$ of this cycle is characterized by an optical absorption band centered at 568 nm. In this state the retinal is in an all-*trans* conformation. Absorption of a photon by the retinal starts the photocycle, which after several short living intermediates comes to the long living $M_{412}$-state which under normal conditions decays within several milliseconds. In this state, the chromophore is in a 13-*cis* conformation with an absorption maximum at 412 nm. The photocycle, which is easily followed by changes in the color of the chromophore, is linked to the proton translocation process. In the $BR_{568}$, the Schiff's base linkage of the retinal to lysine 216 is protonated and becomes deprotonated during M-formation. In this way, the movement of the Schiff's base proton starts the pumping cycle resulting in the ejection of a proton through the external channel of BR to the outside, which is followed by the uptake of another proton from the cytoplasmic side of BR, which leads to a reprotonation of the Schiff's base.

The mechanistic details of this cycle are not yet understood. Central for the unterstanding of this mechanism is the question, whether conformational changes of the protein occur and are essential for the cycle, or whether the protein stays in its ground state conformation with a rigid channel, where the chromophore, by switching from all-*trans* to 13-*cis*, controls the passage of protons. Time resolved X-ray experiments using an intense X-ray plasma source gave indications for very large conformational changes during the photocycle in BR (Frankel and Forsyth, 1985), whereas electron diffraction experiments by Glaeser et al. (1986) detected no changes in diffraction orders in the resolution regime from 60-7 Å. Neutron diffraction experiments on oriented films of purple membranes trapped at liquid nitrogen temperatures in the $M_{412}$ and in the ground state showed moderate intensity changes between both states of the order of 9% in $\Sigma|\Delta I|/\Sigma I$. (Dencher et al., 1989). Model calculation revealed that small changes of 1 or 2 degrees in the tilt angle of several α-helices could account for these differences.

This indicated for the first time that small conformational changes in the tertiary structure are involved in proton translocation. In order to show that these structural changes correlate with relaxation processes in the photo- and pumping cycle of BR, the transition from the M-state to the ground state was followed by a time-resolved X-ray diffraction analysis using intense synchrotron radiation (Koch et al., 1991). The $M_{412}$ decay rate was slowed down by employing mutated BR Asp96Asn in purple membranes.

The time course of flash-induced changes for three reflections at neutral pH is illustrated in Figure X.6.(A). The diffraction pattern was recorded with a linear detector on the X33 double focusing mirror-monochromator camera of the EMBL



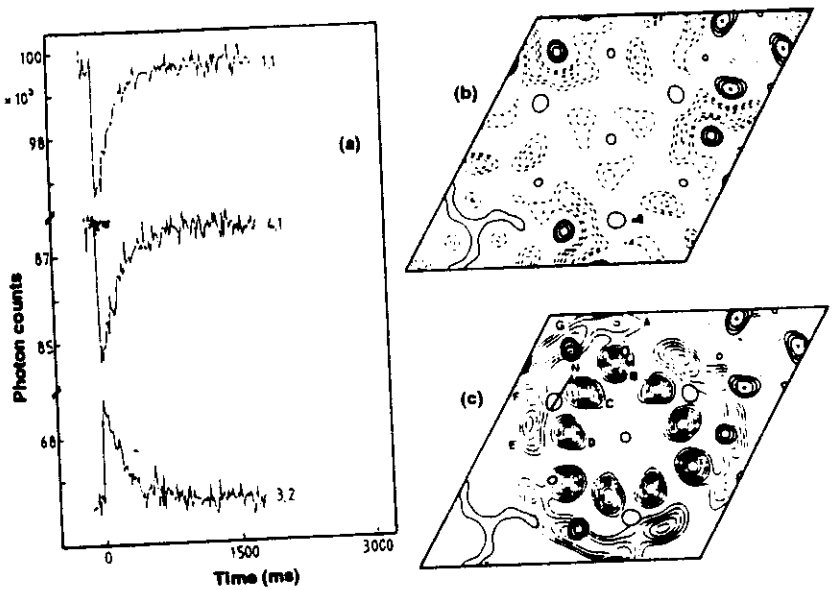


Figure X.6. — (a) Time course, after a short light flash (0.75 ms FWHM) at t = 0 s, of the integrated intensity including back ground under the (1,1), (4,1) and (3,2) reflections for mutated BR Asp96Asn at neutral pH.

(b) Two-dimensional difference Fourier map between the electron densities of the M- and the ground state calculated from amplitudes derived from intensity changes in (A). Continuous contour lines represent positive densities, dashed lines negative densities.

(c) The highest positive difference density levels (bold contours) are plotted on the projected structure of BR in the M-state (thin lines). N marks the position of the Schiff's base nitrogen at the end of the retinal (bold bar). (Photographs from Koch et al., 1991, with permission).

illustrated in Figure X.4.(B.ii). The changes in individual reflections before and immediately after the light flash are consistent both in amplitude and in direction with the earlier neutron results.

Figure X.6.B. shows the difference electron density map obtained from these intensity alterations. The most pronounced changes occur in the vicinity of helix G and between helices E and F (Figure X.6.C.), as also found by neutron diffraction (Dencher et al., 1989). At present it cannot be decided, if the additional large density peak emerging close to helix F, which was not observed by neutron diffraction, reflects a difference in the structural changes of mutated BR. The relaxation times of individual reflections in Figure X.6.A. are very similar having half-times $\tau_{1/2}$ = 150 ms, which are in aggreement with a large relaxation component of absorbance changes in the transition from the M- to the ground state with half-time $\tau_{1/2}$ = 208 ms. This indicates that structural changes correlate in their time behaviour to processes seen by the chromophore in the binding pocket of BR.

Recent cryo-electron diffraction experiments (Subramaniam et al., 1993) fully agree with the above neutron and X-ray results. In these experiments, the M-state was obtained by illumination of a wet purple membrane on a microscopy grid just before injecting it into liquid ethane cooled by a bath of liquid nitrogen. In this way, in difference to earlier electron diffraction experiments, BR is trapped in the M-state embedded in amorphous ice which prevents the drying of the sample.

## REFERENCES: Pure lipid bilayers


BLAUROCK, A.E., 1982 - Biochim. Biophys. Acta 650, 167

BÜLDT, G., GALLY, H.U., SEELIG, J., ZACCAI, G., 1979 - Nature 271, 182

BÜLDT, G., SEELIG, J., 1980 - Biochemistry. 19, 6170

BÜLDT, G., WOHLGEMUTH, R.J., 1981 - J. Membrane Biol. 58, 81

BÜLDT, G., DE HAAS, G.H.J., 1982 - J. Mol. Biol. 158, 55

FRANKS, N.P., LIEB, W.R., 1981.- in Liposomes, page 243-270, ed. by C.G. Knight, Cambridge, Elsevier

HITCHCOCK, P.B., MASON, R., SHIPLEY, G.G., 1975 - J. Mol. Biol. 94, 297

SEELIG, J., SEELIG, A., 1980 - Quarterly Rewiews of Biophysics 13, 19

TARDIEU, A., LUZZATI, V., REMAN, F.C., 1973 - J. Mol. Biol. 75, 711


## REFERENCES: Membrane proteins


BLAUROCK, A.E., 1975 - J. Mol. Biol. 93, 139

BÜLDT, G., KONNO, K., NAKANISHI, K., PLÖHN, H.-J., RAO, B.N., DENCHER, N.A., 1991 - Photochem. Photobiol. 54, 873

DEISENHOFER, J., EPP, O., MIKI, K., HUBER, R. and MICHEL, H., 1985 - Nature 318, 618

DENCHER, N.A., DRESSELHAUS, D., ZACCAI, G., BÜLDT, G., 1989 - Proc. Natl. Acad. Sci. 86, 7876

ENGELMAN, D.M., ZACCAI, G., 1980 - Proc. Natl. Acad. Sci. 77, 5894

ENGELMAN, D.M., HENDERSON, R., MCLACHLAN, A.D., WALLACE, B.A., Proc. Natl. Acad. Sci. 77, 2023-2027 (1980).

FRANKEL,R.D., FORSYTH; J.M., 1985 - Biophys. J. 47, 387

GLAESER, R.M., BALDWIN, J., CESKA, T.A., HENDERSON, R., 1986 - Biophys. J. 50, 913

GRZESIEK, S., DENCHER, N.A., 1986 - FEBS Lett. 208, 337

HENDERSON, R., 1975 - J. Mol. Biol. 93, 123

HENDERSON, R.,UNWIN, P.N.T., 1975 - Nature 257, 28

HENDERSON, R., BALDWIN, J.M., CESKA, T.A., ZEMLIN, F., BECKMANN, E., DOWNING, K.H., 1990 - J. Mol. Biol. 213, 899





HEYN, M.P., WESTERHAUSEN, J., WALLAT, I., SEIFF, F., 1988 - Proc. Natl. Acd. Sci. 85, 2146

JUBB, J.S., WORCESTER, D.L., CRESPI, H.L., ZACCAI, G., 1984 - EMBO J. 3, 1455

KOCH, M.H.J., DENCHER, N.A., OESTERHELT, D., PLÖHN, H.-J., RAPP, G. BÜLDT, G., 1990 - EMBO J. 10, 521

Michel, H., EMBO J. 1, 1276-1271 (1982)

OVCHINNIKOV, YU., ABDULAEV, N., FERGIRA, M., KISELEV, A., LOBANOV, N., 1979 - FEBS Lett. 100, 219

PAPADOPOULOS, G., DENCHER, N.A., ZACCAI, G., BÜLDT, G., 1990 - J. Mol. Biol. 214, 15

POPOT, J.-L., ENGELMAN, D.M., GUREL, O., ZACCAI, G., 1989 - J. Mol. Biol. 210, 829

SUBRAMANIAM, S., GERSTEIN, M., OESTERHELT, D., HENDERSON, R., 1993 - EMBO J. 12, 1

TREWHELLA, J., ANDERSON, S., FOX, R., GOGOL, E., KHAN, S., ENGELMAN, D., ZACCAI, G., 1983 - Biophys. J. 42, 233

TREWHELLA, J., POPOT, J.-L., ZACCAI, G., ENGELMAN, D.M., 1986 - EMBO J. 5, 3045

UNWIN, P.N.T., HENDERSON, R.J., 1975 - Mol. Biol. 94, 425

ZACCAI, G., GILMORE, D.J., 1979 - J. Mol. Biol. 132, 181

WEISS, M.S., KREUSCH, A., SCHILTZ, E., NESTEL, U., WELTE, W., WECKESSER, J. & SCHULTZ, G.E., 1991 - FEBS Lett. 280, 379.